Analysis of total energy probes for sailplane application

N Aucamp

orcid.org/0000-0002-2394-5651

Dissertation submitted in fulfilment of the requirements for the degree *Master of Engineering* in Mechanical Engineering at the North-West University

Supervisor: Dr JJ Bosman

Graduation May 2018

Student number: 22122486

ABSTRACT

Sailplane manufacturers who strive to design and build the best competition sailplanes in the world try to outwit their competitors through improved gliding performance. Although significant effort is made to make the design as sleek as theoretically possible, the external sensors needed to operate the flight instruments diminish these efforts.

The sensors cause the predominantly laminar boundary layer that forms on the aerodynamic surfaces of the sailplane where they are installed to prematurely transition to the turbulent boundary layer, creating parasitic drag. The dissertation aims to identify the possibility of reducing this drag using the total energy probe on the JS-1C Revelation sailplane manufactured by Jonker Sailplanes (JS-1C) as a baseline. Possible total energy probe designs, as well as other external sensors compatible with the JS-1C, were applied to different parts of the sailplane to determine the most optimum sensor selection and arrangement that would promote parasitic drag reduction.

The combination of a total energy probe design applied to the sides of the fuselage as protrusions on the skin, along with the pitot-static probe installed on the tip of the horizontal tail plane, would induce nearly 80 % less drag than that of the current total energy probe. The design required further refinement to ensure uniform pressure drop changes during pitch manoeuvres and insensitivity to pitch and sideslip manoeuvres. This configuration, however, would rather benefit sailplanes in the design phase where the total energy probe design is built into the tooling without having to make modifications later.

The popularity of electric variometers provides an alternative probe configuration, where the installation of two pitot-static probes on each tip of the horizontal tail plane would induce 90 % less drag than that of the current total energy probe. The pitot-static probe provides the best performance during pitch manoeuvres, while the installation of pitot-static probes on each tip should improve the sideslip capabilities thereof by measuring an average pressure. This configuration is also the least invasive method to accurately incorporate the probes into the building process of the sailplane, without having to make significant changes to existing tooling that would reduce tool life and risk diminishing an out-of-mould surface finish.

Key terms: sailplane, glider, parasitic drag, total energy, variometer, boundary layer, transition, dynamic pressure, turbulent kinetic energy, CFD

OPSOMMING

Sweeftuig vervaardigers streef daarna om die beste kompetisie sweeftuie in die wêreld te ontwerp deur hul mededingers onkant te vang met verbeterde sweef prestasie. Hoewel beduidende pogings aangewend word om die ontwerp so vaartbelyn moontlik te maak, benadeel die eksterne sensors benodig om die vlug instrumente aan te dryf, hierdie poging.

Die sensors veroorsaak dat die laminêre grenslaag wat voorkom op die aerodinamiese oppervlaktes van die sweeftuig voortydig oorskakel na die turbulente grenslaag wat onnodige parasitiese sleurkragte veroorsaak. Die verhandeling se doel is om die moontlikheid te ondersoek om hierdie kragte te verminder deur die totale energie sensor op die JS-1C te gebruik as ‘n basislyn. Totale energie sensors, asook ander eksterne sensors wat op die JS-1C geïnstalleer kan word, is ondersoek en toegepas op verskillende gedeeltes van die sweeftuig om die mees optimale sensor kombinasie en plasing te bepaal wat parasitiese sleurkrag vermindering tot gevolg het.

Die kombinasie van ‘n totale energie sensor ontwerp, geplaas op die kante van die romp as knopvormige uitsteeksels, tesame met die installasie van die pitot-statiese sensor op die punt van die horisontale sterkvlerk, behoort byna 80 % minder sleurkragte te veroorsaak as die van die huidige totale energie sensor. Die totale energie sensor ontwerp benodig verdere verfyning om uniforme druk veranderinge in beweging in die laterale as en verminderde sensitiwiteit in beweging in die laterale en vertikale asse te handhaaf. Hierdie konfigurasie sal hoofsaaklik ‘n sweeftuig in die ontwerp fase bevoordeel, waar die totale energie sensor in die produksielyn toerusting ingebou word sonder om later veranderinge aan die eindproduk aan te bring.

Die gewildheid van elektroniese variometers verskaf ‘n alternatiewe sensor konfigurasie, waar twee pitot-statiese sensors geïnstalleer word, op elke punt van die horisontale stertvlerk, en behoort 90 % minder sleurkragte te veroosaak as die van die huidige totale energie sensor. Die pitot-statiese sensor verskaf die beste prestasie tydens beweging in die laterale as, terwyl die installasie van pitot-statiese sensors op elke punt die prestasie tydens beweging in die vertikale as behoort te verbeter deur die gemiddelde druk te meet. Hierdie konfigurasie is ook die maklikste manier om die sensors akkuraat in die bou proses van die sweeftuig te inkorporeer sonder om beduidende veranderinge aan bestaande produksielyn toerusting aan te bring en sodoende die leeftyd van die toerusting en die oppervlak afwerking van die parte te belemmer.

Sleutel terme: sweeftuig, parasitiese sleurkragte, totale energie, variometer, grenslaag, oorgang, dinamiese druk, turbulente kinetiese energie, CFD

ACKNOWLEDGEMENTS

I would like to thank the following people:

- Johan Bosman as my supervisor for his guidance and support throughout the time span of the dissertation.
- My family for their continuous support and encouragement when I needed it most.
- Uys Jonker and A.P. Kotze for the flight tests conducted.
- My colleagues at Jonker Sailplanes for their support and optimism.

DISSERTATION LAYOUT

The dissertation is chronologically written based on the order of the work completed.

Chapter 1: An introduction to the dissertation is provided with a brief summary of the use of total energy probes. The problem statement, objective and deliverables are discussed.

Chapter 2: All literature and principles applicable to the dissertation are briefly summarised in the literature study. The sub-paragraphs are arranged according to the thinking process used during the progress of the dissertation, starting with the main components of a sailplane and ending with how total energy probes are tested for conformance to theory and practice.

Chapter 3: Theoretical models were created to formulate an ideal total energy probe based on the information from the literature study.

Chapter 4: A baseline Computational Fluid Dynamics (CFD) program was created to enable more accurate comparison of different total energy probe configurations and designs, all with the same base programming.

Chapter 5: Flight tests were conducted to determine the compensation characteristics of the current total energy probe. The data was compared to the theoretical models to determine the conformance of the current probe to theory. The data was also compared to the CFD program created (Chapter 4) in Chapter 6 to verify the ability thereof to recreate flight test data.

Chapter 6: The CFD program created in Chapter 4 was used to recreate the flight test data and compared to the actual flight test data for verification.

Chapter 7: The theoretical drag force of a simple aerofoil was calculated and compared to the CFD program to verify the ability thereof to recreate the drag force. The current total energy probe was recreated in CFD and the results compared to an oil test conducted on the JS-1C tail fin to also verify external airflow replication. The estimated drag caused by the current probe was then calculated using CFD.

Chapter 8: Alternative total energy probe designs are presented for the tail fin based on the flight test and CFD data obtained for the current probe.

Chapter 9 and 10: The current total energy probe was moved to other parts of the JS-1C, namely the horizontal tail plane (Chapter 9) and the fuselage (Chapter 10). The effect of the current probe positioned at different locations of the sailplane on the surfaces thereof was analysed and alternative or improved total energy probe designs are presented for each location.

Chapter 11: The installation of other external sensors, besides the total energy probe, required for flight was discussed. The drag induced by the pitot-static probe at different locations on the sailplane was analysed, as well as the possibility of replacing all external sensors with a single, multi probe.

Chapter 12: The manufacturability of the total energy probe configurations and designs was discussed regarding different methods to incorporate the probes into the building process of the sailplane and the risks relating to each method.

Chapter 13, 14 and 15: The main discussion compares the total energy probe configurations and designs based on their overall performance and installation (Chapter 13). The main conclusions to the dissertation were summarised (Chapter 14) and recommendations were made based on the conclusions reached (Chapter 15).

TABLE OF CONTENTS

LIST OF TABLES

LIST OF FIGURES

LIST OF EQUATIONS

NOMENCLATURE

ABBREVIATIONS

AOA	Angle of attack
CAS	Calibrated airspeed
CFD	Computational fluid dynamics
IAS	Indicated airspeed
JS-1C	JS-1 Revelation sailplane manufactured by Jonker Sailplanes
RFC	Request for Change document

SYMBOLS

Greek letters:

θ	Angle	° (degrees)
ρ	Density	kg/m^3
μ	Dynamic viscosity	Pa*s

Roman characters:

a	Radius	m
A	Area	m^2
A_1	Area upstream	m^2
A_2	Area downstream	m^2
$C_{D\ laminar\ total}$	Total laminar drag force coefficient	-
$C_{D\ turbulant\ total}$	Total turbulent drag force coefficient	-
C_{P1}	Pressure coefficient before manoeuvre	-
C_{P2}	Pressure coefficient after manoeuvre	-
C_{Plocal}	Local pressure coefficient	-
D	Chord length	m
$D_{laminar\ total}$	Total laminar drag force	N
$D_{turbulant\ total}$	Total turbulent drag force	N
ΔE_K	Change in kinetic energy	J
ΔE_P	Change in potential energy	J
ΔE_T	Change in total energy	J
g	Gravitational acceleration	m/s^2
h_1	Height before manoeuvre	m
h_2	Height after manoeuvre	m
Δh	Change in height	m
m	Mass	kg
P	Pressure	Pa
P_1	Pressure upstream	Pa

Roman characters:

P_2	Pressure downstream	Pa
$P_{dynamic}$	Dynamic pressure	Pa
$P_{dynamic1}$	Dynamic pressure upstream / before manoeuvre	Pa
$P_{dynamic2}$	Dynamic pressure downstream / after manoeuvre	Pa
P_{local}	Local pressure	Pa
P_{local1}	Local pressure before manoeuvre	Pa
P_{local2}	Local pressure after manoeuvre	Pa
P_s	Pressure along a cylinder	Pa
P_{static}	Static pressure	Pa
$P_{static1}$	Static pressure upstream / before manoeuvre	Pa
$P_{static2}$	Static pressure downstream / after manoeuvre	Pa
r	Radial coordinate measured from the centreline	m
Re_{total}	Total Reynolds number	-
S	Frontal area of an aerofoil	m^2
V	Velocity	m/s
V_1	Velocity upstream / before manoeuvre	m/s
V_2	Velocity downstream / after manoeuvre	m/s
V_{MIN}	Minimum speed	km/h
V_{NE}	Never exceed speed	km/h
V_r	Radial velocity	m/s
V_θ	Tangential velocity	m/s
$V_{\theta s}$	Tangential velocity along a cylinder	m/s
ΔV	Change in velocity	m/s

CHAPTER 1: INTRODUCTION

The background, problem statement, objectives and expected deliverables of the dissertation are discussed.

1.1 Background

A sailplane is a light-weight aircraft used for gliding (Figure 1-1). The design includes high aspect ratio wings and a high lift-to-drag ratio for improved climbing performance, reduced sink rate and long distance gliding at high speeds.

Figure 1-1: The JS3 Rapture sailplane

Soaring includes the ability to detect and determine climb and sink rates in the air to maintain gliding at higher altitudes for longer periods (Nicks, 1976). A pilot uses a variometer to determine whether the sailplane is in an area of rising air or sink, which measures the rate of change in total energy (the change in altitude and speed due to rising and sinking air) (FAA, 2013; Nicks, 1976; Reid, 2009a).

The pilot has two choices in still air, to exchange altitude for increased speed by pushing the control stick forward, or to exchange speed to gain altitude by pulling the control stick back. Both choices have no effect on the change in the total energy, since potential energy (altitude) and kinetic energy (velocity) was exchanged, not gained or lost. A sailplane that enters an area of rising air (also known as a thermal) at a constant velocity will experience an increase in total energy as the sailplane gains altitude without having to decrease speed. A sailplane that enters an area of sink at a constant velocity will experience a decrease in total energy, where altitude decreases without having to increase speed (Nicks, 1976; Reid, 2009a).

A variometer is connected directly to the atmosphere using a total energy probe. The design of the total energy probe enables it to compensate for changes that do not involve the detection of rising and sinking air. The probe is mostly positioned in free stream air away from the body and surrounding surfaces to measure the surrounding air unaffected by the presence of the

sailplane. The pilot can determine the strength and stability of a thermal by observing the movement of the variometer indicator (Brandes, 1975; FAA, 2013; Nicks, 1976; Reid, 2009a).

1.2 Problem statement

The current position of the total energy probe on the JS-1C vertical tail fin causes parasitic or unnecessary drag (Figure 1-2). A large wake is created behind the probe, where turbulent flow induces drag over the surface of the fin. The drag reduces the gliding performance of the sailplane, which reduces the gliding duration and altitude gained in a thermal. The probe can be moved to a different area on the sailplane, but could induce the same amount of drag (or more) at the targeted area. Also, the probe could induce drag on various surfaces of the sailplane at the same time that further undermines the performance of the sailplane.

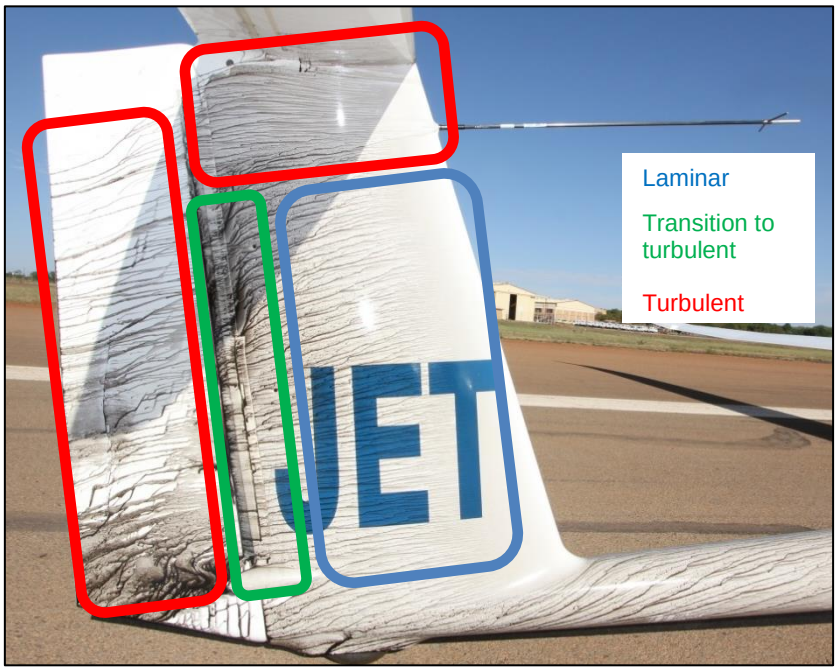

Figure 1-2: Drag induced by the current total energy probe visualised through an oil test (JS, 2014)

Furthermore, the capabilities of the probe may be reduced if moved to a different location, causing inaccurate readings on the variometer. The design of a new total energy probe concept is also a challenge, where it could easily under- or over-compensate. A sailplane is not only subjected to various manoeuvres (ascending, descending and turns), but also environmental conditions such as wind, temperature and humidity. The probe must be able to compensate for and barely indicate any changes that do not involve the detection of rising and sinking air.

1.3 Objective

The objectives of the dissertation include (1) investigating the effect of the total energy probe on the boundary layer of the JS-1C tail fin and (2) the possibility of reducing the drag caused by the probe without reducing the compensation capabilities thereof.

1.4 Deliverables

The deliverables of the dissertation include (1) a complete literature study that summarises all principles and information relevant to the dissertation, (2) theoretical models that recreate an ideal total energy probe, (3) a baseline CFD program that replicates flight test data and calculates the theoretical drag, (4) test data on the compensation capabilities of the current total energy probe and (5) the optimum probe configuration and placement to promote drag reduction.

A literature study was compiled to analyse various factors that influence the position, drag performance, compensation capabilities and design of the total energy probe.

CHAPTER 2: LITERATURE STUDY

There are various factors to consider when moving or designing a total energy probe. These factors include (1) the main components of a sailplane, (2) what a sailplane uses to stay aloft, (3) how to find or detect these sources, (4) how a total energy probe measures these sources and compensates for false readings, (5) how airflow over an aerofoil works, (6) where a total energy probe can be positioned to induce minimum drag and measure the change in total energy effectively and (7) how the characteristics of a total energy probe can be tested during various flight manoeuvres.

2.1 Components of a sailplane

A sailplane consists of four main components, namely the fuselage, wings, vertical tail fin and horizontal tail plane. Each component is designed to improve the stability of the aircraft in the latitudinal, longitudinal and vertical axis and to maximize lift generation.

2.1.1 Fuselage

The fuselage is the baseline part to which all the other parts of the sailplane are attached to. It houses the cockpit that contains all the controls necessary for the pilot to control the sailplane during flight in the latitudinal, longitudinal and vertical axis.

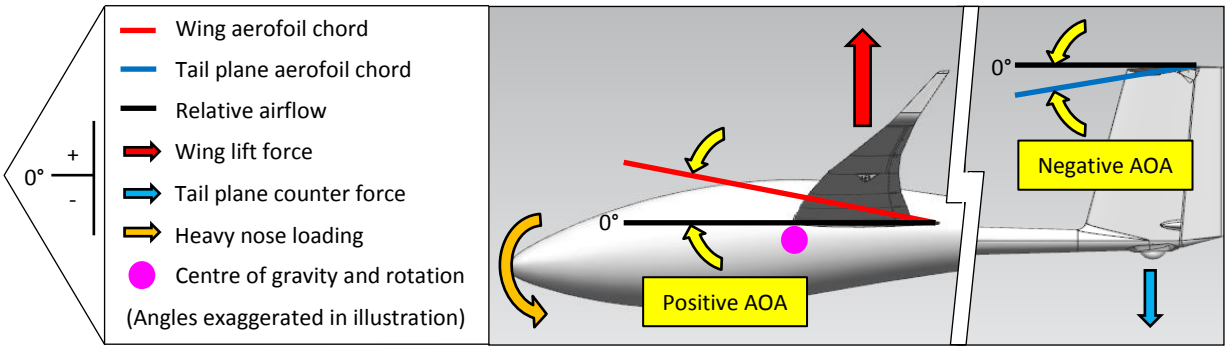

Figure 2-1: Wing aerofoil with a positive angle of attack and tail plane aerofoil with a negative angle of attack (FAA, 2013)

A sailplane is designed nose heavy to promote longitudinal stability, minimising the effect of forces acting along the longitudinal axis from causing the sailplane to pitch uncontrollably (Figure 2-1) (FAA, 2013). This also prevents the sailplane from stalling easily during flight, where a nose down attitude is maintained and promotes airflow over the wings for lift generation. A stall occurs when the airflow over the wings becomes distorted or separates prematurely from the wing surface to a point where the airflow does not produce enough lift to counter the weight of the sailplane. A sailplane that is designed tail heavy has a centre of

gravity positioned closer to the tail that causes the sailplane to assume a nose up attitude, increasing the probability of a stall occurring.

2.1.2 Wings

The aerofoil of a sailplane wing causes air to accelerate over the top surface to create low pressure and decelerate over the bottom surface to create high pressure (FAA, 2013). The high pressure on the bottom surface is the lift generating force that enables the sailplane to gain altitude for flight.

The design includes a positive angle of attack (AOA), which twists the wing to form a positive angle between the chord of the wing aerofoil (a straight line that connects the leading and trailing edges of an aerofoil together) and the relative airflow for improved lift generation (Figure 2-1). The nose up attitude of a sailplane designed tail heavy, or pulling back on the control stick excessively to raise the nose, can increase the angle of attack (AOA) to a negative extent. After around 15° AOA it becomes harder for the air to flow along the aerofoil, which causes premature air separation and reduces lift generation. If the AOA keeps increasing the weight of the sailplane eventually exceeds the lift force generated, causing the sailplane to lose altitude.

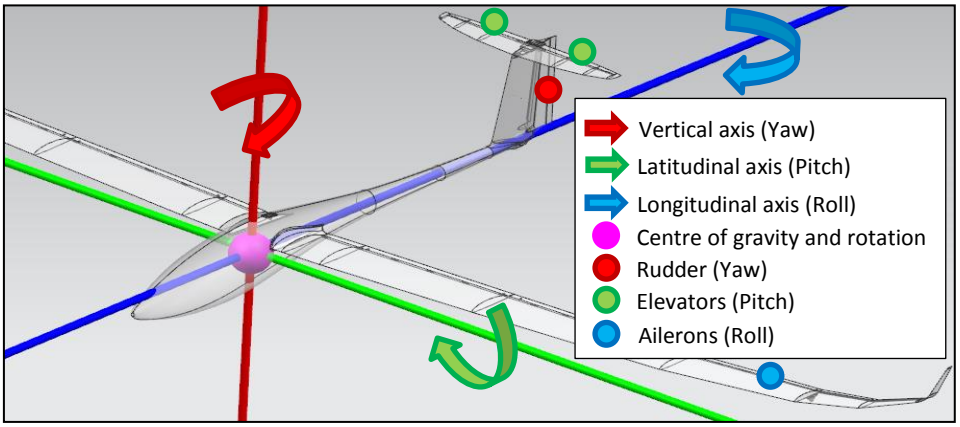

Figure 2-2: Axis of rotation on a sailplane through the centre of gravity (FAA, 2013)

The ailerons connected to the wings control the movement of the sailplane in the longitudinal axis (Figure 2-2).

2.1.3 Vertical tail fin

The fin forms part of the fuselage and acts as a vertical stabiliser to prevent the sailplane from yawing uncontrollably in the vertical axis (Figure 2-2) (FAA, 2013). It is symmetric to the airflow, causing the air to flow the same speed along the sides thereof that creates an equal pressure distribution on either side.

The rudder connected to the fin controls the movement of the sailplane in the vertical axis.

2.1.4 Horizontal tail plane

The tail plane is used as a horizontal stabiliser to counter the natural pitch forward motion of a sailplane during normal flight due to the heavy nose loading (Figure 2-1) (FAA, 2013). The design is almost the same as a wing aerofoil, but with its own design. It is positioned at a negative angle of attack that causes air to decelerate over the top surface to create high pressure and accelerate over the bottom surface to create low pressure (Figure 2-3). The high pressure on the top surface pushes the tail section of the sailplane down to counter the natural forward pitch motion of the sailplane during normal flight.

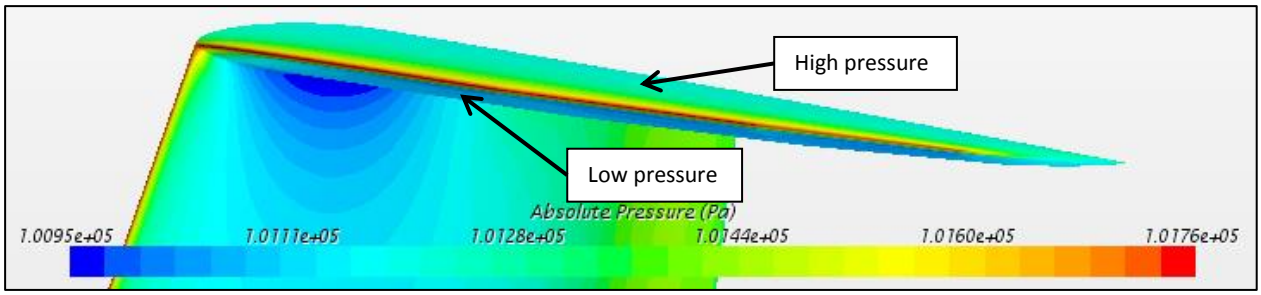

Figure 2-3: Horizontal tail plane aerofoil design

The elevators connected to the tail plane control the movement of the sailplane in the latitudinal axis (Figure 2-2).

A pilot uses lift sources, such as thermals, to keep the sailplane aloft for extended periods without the use of an additional power source.

2.2 Thermals and sink

The sun heats the ground to a higher temperature than the surrounding environment, causing the air near the ground to heat up and rise (FAA, 2013; Gordon, 2006). The heavier cold air above the heated air prevents it from rising, forcing the heated air to break through in the form of a concentrated column or bubble (FAA, 2013). The movement of the rising air causes an updraft (lift) and the sides of the column cooling causes a downdraft (sink) as the cooled air returns to the ground (Figure 2-4) (FAA, 2013; Gordon, 2006).

Sailplanes depend on these columns or bubbles of rising air to stay aloft for longer periods without having to change speed (FAA, 2013; Gordon, 2006; Nicks, 1976). A pilot has two goals, to gain altitude for extended flight and to increase speed to reach a destination quicker. In still air both goals cannot be satisfied and the pilot is left with two choices (Figure 2-5); (1) exchange altitude for increased speed by pushing the control stick forward to descend or (2) exchange speed to gain altitude by pulling the control stick back to ascend.

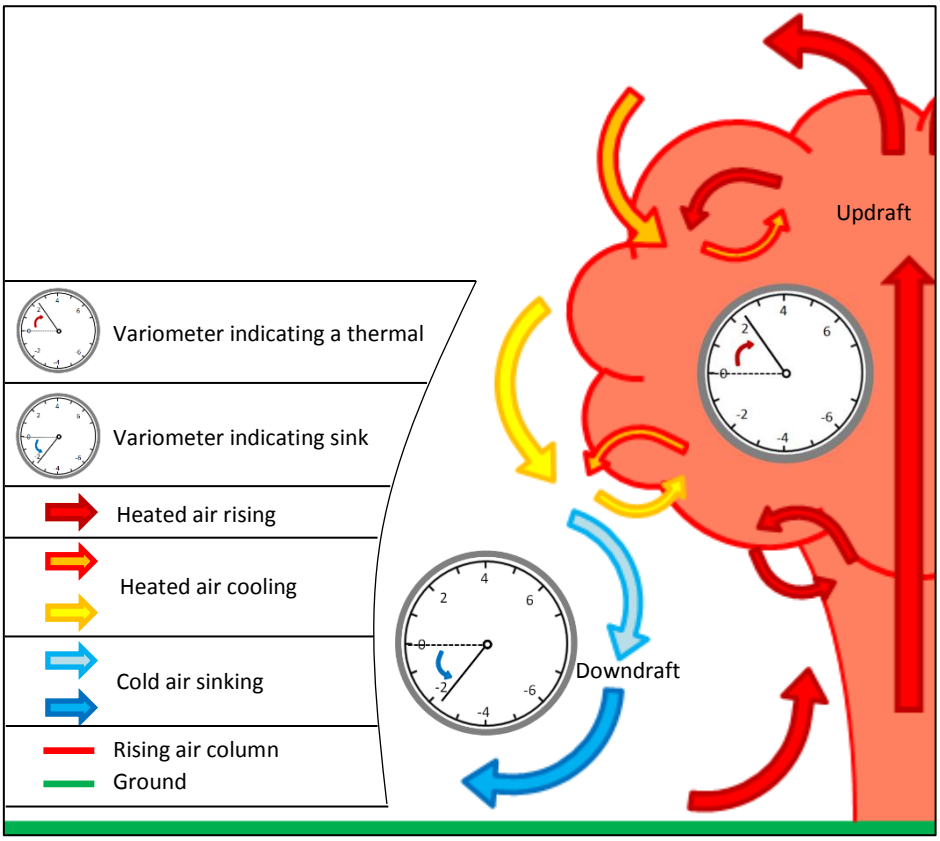

Figure 2-4: **Updraft and downdraft caused by rising and sinking air respectively (FAA, 2013)**

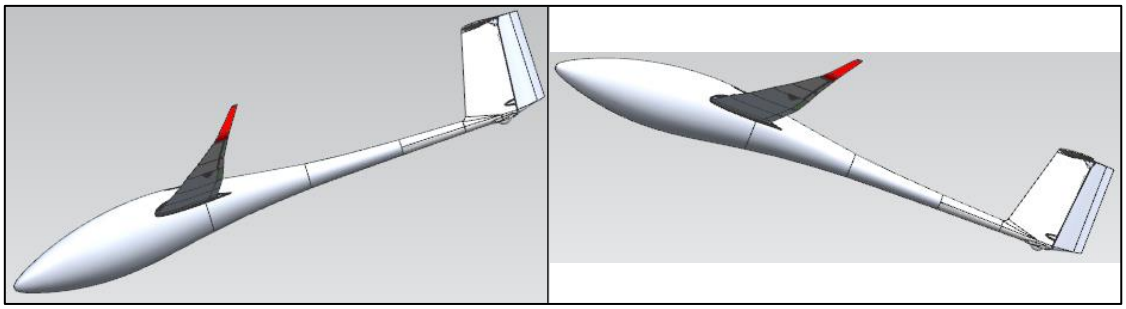

Figure 2-5: **Altitude exchanged for increased speed (left) and speed exchanged for altitude gain (right)**

Both actions result in no change in the total energy, since energy was exchanged and not gained or lost (Nicks, 1976). The potential energy (altitude) of the sailplane is converted into kinetic energy (speed) when descending and vice versa when ascending in still air. This is known as total energy compensation, where the change in total energy is equal to the sum of the change in potential and kinetic energy (Nicks, 1976; Reid, 2009a).

$$\Delta E_T = \downarrow \Delta E_P + \uparrow \Delta E_K = \downarrow mg\Delta h + \uparrow \tfrac{1}{2}m\Delta V^2 = 0$$

Equation 2-1: **Total energy remains unchanged during descent in still air (Reid, 2009a)**

$$\Delta E_T = \uparrow \Delta E_P + \downarrow \Delta E_K = \uparrow mg\Delta h + \downarrow \tfrac{1}{2}m\Delta V^2 = 0$$

Equation 2-2: **Total energy remains unchanged during ascent in still air (Reid, 2009a)**

A pilot that enters a thermal at a constant velocity will experience the sensation of being pushed into their seat as the rising air mass pushes the sailplane upward. This sensation is the result of an increase in total energy, because altitude is gained without additional control stick input (Nicks, 1976).

$$\uparrow \Delta E_T = \uparrow \Delta E_P + \Delta E_K = \uparrow mg\Delta h + 0$$

Equation 2-3: Total energy gained in a thermal without exchanging speed

A pilot that enters an area of sink at a constant speed will experience the sensation of falling, where the sailplane is forced to flow with the cooler air downward. This sensation is the result of a decrease in total energy, where altitude is lost without additional control stick input (Nicks, 1976).

$$\downarrow \Delta E_T = \downarrow \Delta E_P + \Delta E_K = \downarrow mg\Delta h + 0$$

Equation 2-4: Total energy lost in sink without exchanging speed

Experienced pilots know how to identify potential thermal sources in their surroundings such as clouds, dust devils and soaring birds (Gordon, 2006). They also use the sensation caused by thermals to determine the strength and stability thereof and whether the sailplane is in an area of sink.

Variometers are installed into sailplanes to visually indicate the strength and stability of thermals, as well as sink, more efficiently.

2.3 Variometer

A variometer is an instrument used mostly in sailplanes to indicate and measure the presence of thermals (FAA, 2013; Nicks, 1976). The pilot can determine whether the sailplane is in a thermal and whether or not to search for stronger, more stable thermals by observing the extent and rate of movement of the indicator (FAA, 2013).

A variometer is divided into two compartments by a diaphragm and connected to a flask and static pressure inlet (Figure 2-6) (FAA, 2013). The flask is isolated within the sailplane to prevent temperature from influencing the pressure induced inside the flask acting on the diaphragm (isolated compartment). The static pressure acts on the other side of the diaphragm (second compartment) and the capillary tube that connects the two compartments equalises the pressure between them by delaying the airflow in and out of the isolated compartment. The display needle of the variometer is indirectly connected to the diaphragm, which indicates the change in total energy as the pressure changes within the flask and the diaphragm expands and retracts.

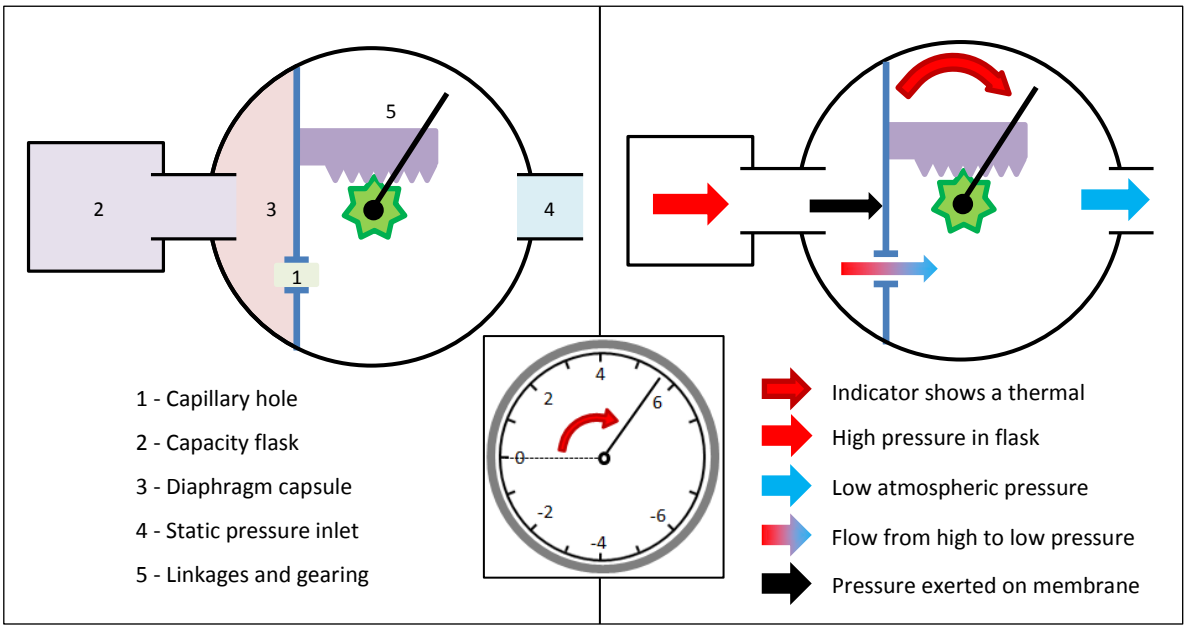

Figure 2-6: **Variometer working principle (FAA, 2013)**

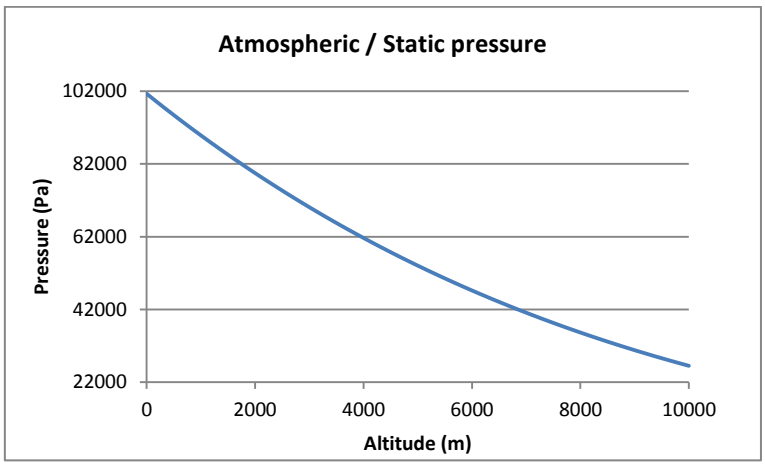

Figure 2-7: **Static pressure decreases as altitude increases**

Static pressure, also known as atmospheric pressure, decreases as altitude increases (Figure 2-7) and is assumed to be around 101 325 Pa at sea level (zero altitude) (Kantrowitz, 1940; Reid, 2009a). A sailplane flying through a thermal at a constant speed will experience an increase in altitude and a decrease in static pressure (Nicks, 1976; Reid, 2009a; Ostroff, et al., 1981).

$$P_{static} = \rho g \Delta h$$

Equation 2-5: **Static pressure (Kantrowitz, 1940; Reid, 2009a)**

The decrease in static pressure causes the pressure in the second compartment to decrease and the pressure in the isolated compartment to expand against the diaphragm (flow from a high pressure area to a low pressure area), moving the display needle of the variometer to indicate the presence of a thermal (Figure 2-6) (FAA, 2013). Air flows slowly through the capillary tube from the isolated flask to the second compartment to equalise the pressure,

causing the diaphragm to gradually return to its original position and the variometer to indicate no change in total energy. A variometer can measure changes in altitude and velocity using a total energy probe (FAA, 2013; Nicks, 1976).

There are various types of total energy probes that use different principles to achieve the same goal; to measure the change in total energy due to the surrounding air mass.

2.4 Total energy measurement and compensation

A total energy probe measures the static pressure around the sailplane and ignores the pressure changes induced by control input (roll, pitch and yaw) and environmental changes (wind, temperature and moisture content) through sufficient compensation. Various probe configurations were created, using the basic principles of a venturi, Bernoulli's equation and the flow around a cylinder, as the understanding of sailplanes and soaring developed.

2.4.1 Venturi compensation

In 1940 Arthur Kantrowitz proposed the use of a venturi to measure the change in pressure for total energy measurement, where the air is assumed to be steady, incompressible and has a constant density (Anderson, 1991; Dawydoff, 1943; Kantrowitz, 1940; Nicks, 1976). The venturi effect states that, according to the conservation of mass, the velocity of the air will increase when it moves from a large area to a constricted area and vice versa (Anderson, 1991).

$$\downarrow V_1 \uparrow A_1 = \uparrow V_2 \downarrow A_2$$

Equation 2-6: Venturi effect according to the conservation of mass (Anderson, 1991)

A venturi is unaffected by angle of attack, even in rough air, making it effective during ascending and descending and uses Bernoulli's principle to account for the dynamic pressure (Dawydoff, 1943; Kantrowitz, 1940). Bernoulli's equation states that the pressure over two areas measured will be constant according to the conservation of mass (Anderson, 1991; McCormick, 1979).

$$P + P_{dynamic} + P_{static} = \text{Constant}$$

Equation 2-7: Bernoulli's equation (Anderson, 1991; McCormick, 1979)

The dynamic pressure is the pressure induced by the change in kinetic energy or velocity (Kantrowitz, 1940; Nicks, 1976; Ostroff, et al., 1981; Reid, 2009a).

$$P_{dynamic} = \tfrac{1}{2}\rho\Delta V^2$$

Equation 2-8: Dynamic pressure (Kantrowitz, 1940; Reid, 2009a)

The implementation of the venturi effect into Bernoulli's equation causes the pressure to increase when the velocity decreases and vice versa.

$$\uparrow P_1 + \downarrow P_{dynamic1} + P_{static1} = \downarrow P_2 + \uparrow P_{dynamic2} + P_{static2}$$

Equation 2-9: Bernoulli's equation according to the venturi effect (Anderson, 1991)

Static pressure decreases as the altitude increases. Therefore, the pressure induced by the change in total energy (total pressure exerted on the diaphragm of a variometer) is equal to the difference between the dynamic and static pressure (Anderson, 1991; Dawydoff, 1943; Kantrowitz, 1940; Nicks, 1976; Reid, 2009a).

$$P_{local} = P_1 - P_2 = \tfrac{1}{2}\rho\Delta V^2 + (-\rho g \Delta h) = P_{dynamic} - P_{static}$$

Equation 2-10: Local pressure (Anderson, 1991; Dawydoff, 1943; Kantrowitz, 1940; Nicks, 1976; Reid, 2009a)

The dynamic pressure is equal to the static pressure if the local pressure remains unchanged (there is no change in the total energy) (Kantrowitz, 1940; Reid, 2009a).

$$0 = P_{dynamic} - P_{static} \quad \rightarrow \quad P_{dynamic} = P_{static}$$

Equation 2-11: Local pressure remains unchanged (Kantrowitz, 1940; Reid, 2009a)

The rate of change in the pressure measured by a variometer is proportional to the difference between the local and static pressure and can be expressed as a non-dimensional value known as a pressure coefficient or C_P (Anderson, 1991; Nicks, 1976; Ostroff, et al., 1981; Reid, 2009a).

$$C_p = \frac{P_{local} - P_{static}}{P_{dynamic}}$$

Equation 2-12: Pressure coefficient (Anderson, 1991; Nicks, 1976; Ostroff, et al., 1981; Reid, 2009a)

The substitution of the unchanged local pressure equation into the pressure coefficient equation reveals that the pressure coefficient to be measured by the probe for sufficient compensation equals -1 (Nicks, 1976; Ostroff, et al., 1981; Reid, 2009a).

$$C_{p_{local}} = \frac{0 - P_{dynamic}}{P_{dynamic}} = -1$$

Equation 2-13: Local pressure coefficient if total energy remains unchanged (Nicks, 1976; Ostroff, et al., 1981; Reid, 2009a)

In 1943 Alexis Dawydoff published a representation of the Kantrowitz venturi, assuming a contraction ratio of √2 to produce a pressure drop equal to the dynamic pressure (Figure 2-8) (Dawydoff, 1943; Kantrowitz, 1940). The Kantrowitz venturi required a contraction ratio and

throat diameter of high tolerance for accurate measurement that made it expensive and difficult to manufacture (Dawydoff, 1943).

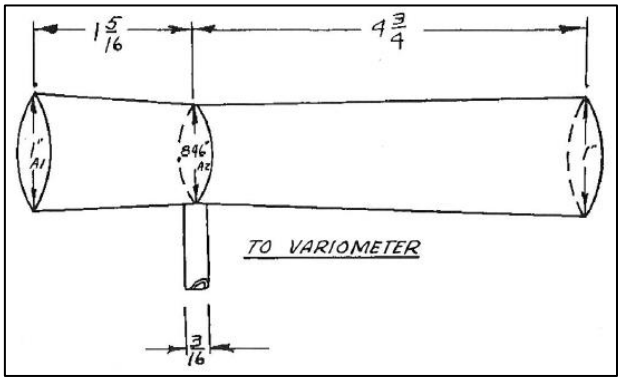

Figure 2-8: Representation of the Kantrowitz venturi (Dawydoff, 1943)

In 1954 Frank Irving presented a similar venturi with a more complex shape (Figure 2-9) (Althaus, 1971). The design has an external disc for a wider yaw operation range and a sudden downstream bore diameter increase. The design improved manufacturability, but was still expensive and induced significant drag.

In 1970 Dieter Althaus presented an improved version of the Irving design to reduce the drag by reducing the size of the venturi and using an outer tube with two cylindrical shaped protrusions to generate a high suction peak (Figure 2-9) (Althaus, 1971; Brandes, 1975). The design induced laminar flow behind the protrusions with low Reynolds numbers that enabled suction to only vary with flight speed (Althaus, 1971). The amount of suction generated was affected by the distance between the protrusions and adjusted using a wind tunnel to obtain a C_P of -1.

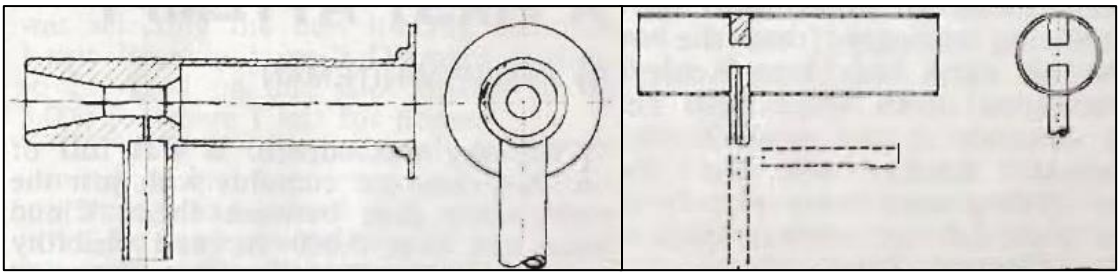

Figure 2-9: Frank Irving (left) and Dieter Althaus (right) venturi (Althaus, 1971)

2.4.2 Braunschweig tube

In 1975 Tom Brandes published the design of the Braunschweig tube, created in 1973 by the Braunschweig University of Germany's gliding club (Figure 2-10) (Brandes, 1975). The probe uses the principle of flow around a cylinder (Figure 2-11) to measure static and dynamic pressure and is positioned perpendicular to the airflow with slots downwind of the tube.

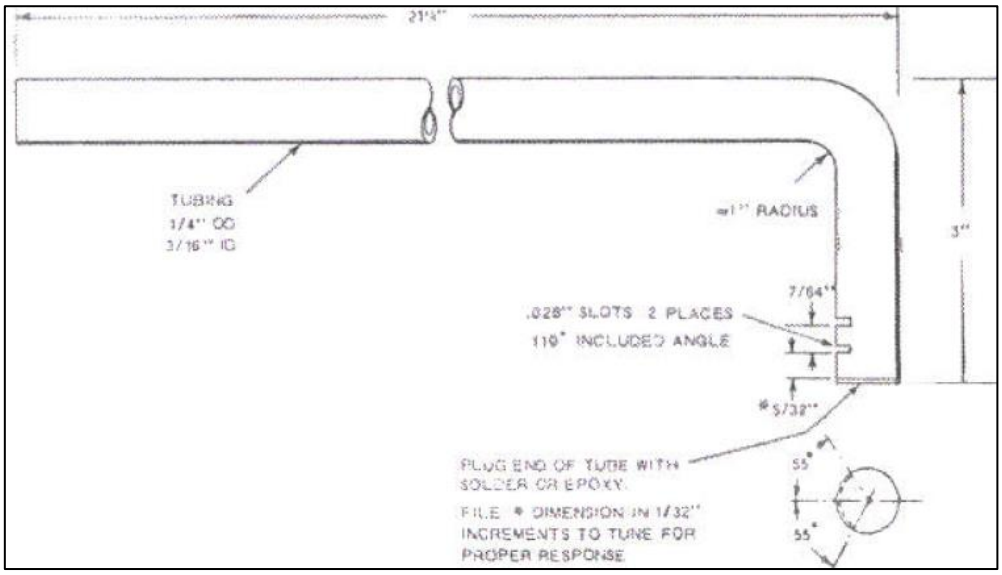

Figure 2-10: **Braunschweig tube (Brandes, 1975)**

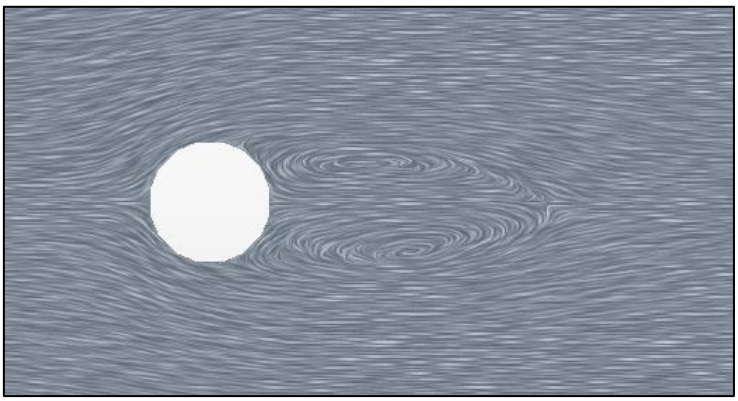

Figure 2-11: **Flow around a cylinder**

The pressure distribution upstream and along a cylinder can be derived from Bernoulli's equation (Anderson, 1991; Ngo & Gramoll, 2016).

$$P_1 + \tfrac{1}{2}\rho V^2 = P_s + \tfrac{1}{2}\rho {V_{\theta s}}^2$$

Equation 2-14: **Pressure distribution along a cylinder (Anderson, 1991; Ngo & Gramoll, 2016)**

The radial and tangential velocity of a cylinder can be simplified when derived along the surface (Anderson, 1991; Ngo & Gramoll, 2016).

$$V_r = V\left[1 - \left(\frac{a}{r}\right)^2\right]\cos\theta = V\left[1 - \left(\frac{r}{r}\right)^2\right]\cos\theta = 0$$

Equation 2-15: **Radial velocity along a cylinder (Anderson, 1991; Ngo & Gramoll, 2016)**

$$V_\theta = -V\left[1 + \left(\frac{a}{r}\right)^2\right]\sin\theta = -V\left[1 + \left(\frac{r}{r}\right)^2\right]\sin\theta = -2V\sin\theta$$

Equation 2-16: **Tangential velocity along a cylinder (Anderson, 1991; Ngo & Gramoll, 2016)**

The pressure coefficient of the cylinder can be derived by substituting the tangential velocity equation into the pressure distribution equation (Anderson, 1991; Ngo & Gramoll, 2016).

$$C_P = \frac{P_s - P_1}{\frac{1}{2}\rho V^2} = 1 - 4(\sin\theta)^2$$

Equation 2-17: Pressure coefficient along a cylinder (Anderson, 1991; Ngo & Gramoll, 2016)

The theoretical pressure coefficient downwind of the cylinder (at 180°) equals one (Figure 2-12) (Ngo & Gramoll, 2016). The placement of slots downwind of the probe creates a vacuum within the probe and, therefore, creates a negative C_P of -1. The slots enabled the probe to measure changes in velocity and altitude with sufficient compensation, but required high accuracy which made manufacturability difficult (Brandes, 1975; Nicks, 1976).

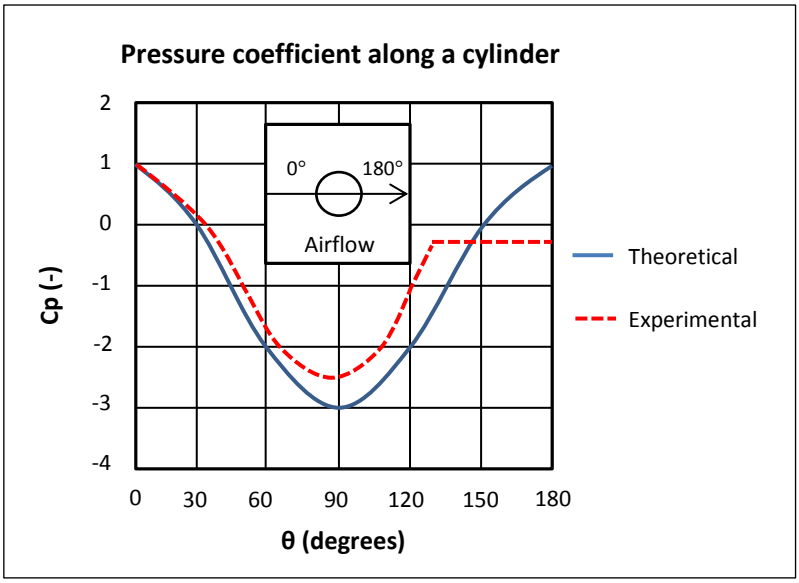

Figure 2-12: Theoretical and experimental pressure coefficient along a cylinder (Ngo & Gramoll, 2016)

2.4.3 Total energy sensor

The design of the total energy sensor is based on the Braunschweig tube and incorporates holes drilled downwind of the tube, simplifying manufacturability and making it less expensive (Johnson, 1998; Nicks, 1976). In 1976 Oran Nicks published a design where he used wind tunnel and flight tests to analyse various design configurations to create the ideal total energy sensor (Figure 2-13) (Nicks, 1976). The design includes (1) a cylindrical tube with a diameter ranging from 4.8 mm to 6.4 mm, (2) a pressure orifice facing downstream around a third of the diameter of the probe, (3) the pressure orifice positioned twice the diameter of the probe from the end, (4) a forward swept angle of 20°, (5) the probe positioned in free stream air and (6) the end of the probe squared off with a slight bevel (Johnson, 1998; Nicks, 1976; Reid, 2009b). The probe provides excellent compensation up to 6 096 metres and is unaffected by normal pitch, roll and yaw configurations from 65 km/h to 240 km/h (Nicks, 1976; Reid, 2009b).

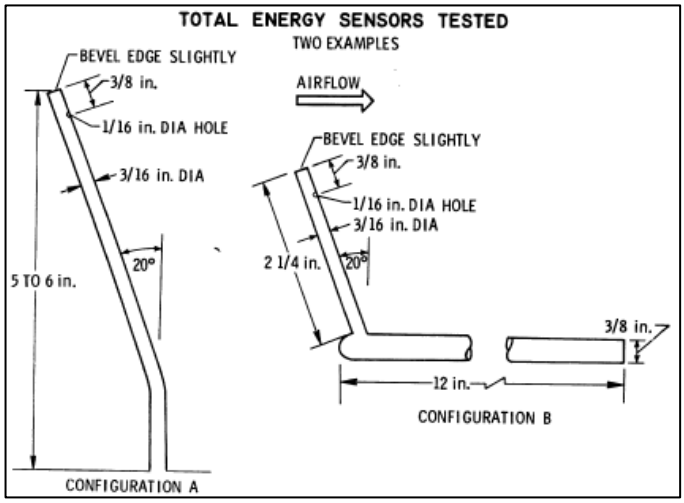

Figure 2-13: **Ideal total energy sensor for the fuselage (configuration A) and tail fin (configuration B) (Nicks, 1976)**

In 1998 Richard, H. Johnson published a design based on the Nicks total energy sensor for the fuselage (Figure 2-14) (Johnson, 1998). The swept angle was removed and the distance of the pressure orifice from the end of the tube and the height of the pressure orifice above the fuselage was varied. The design measured less compensation errors and minimal changes during ascending and descending compared to the Nicks total energy sensor.

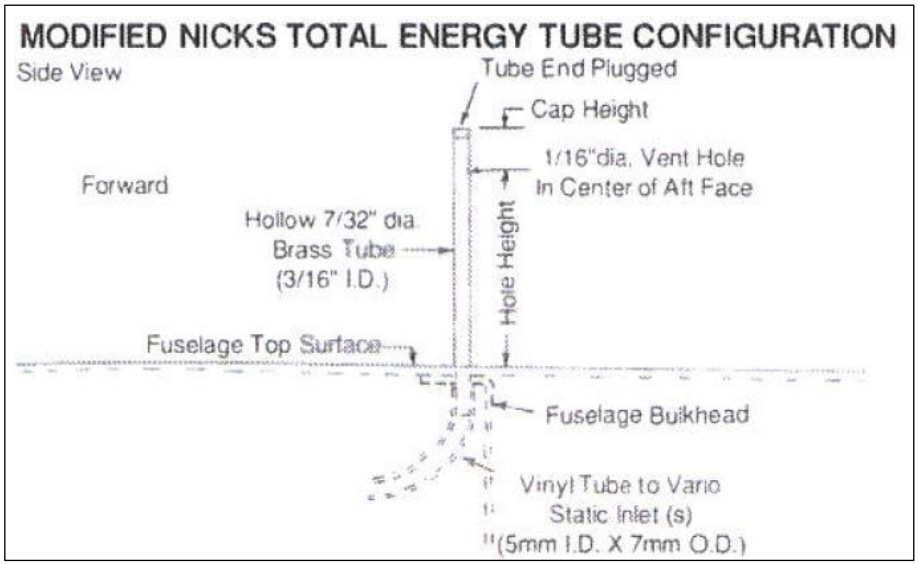

Figure 2-14: **Modified Nicks total energy sensor for the fuselage (Johnson, 1998)**

2.4.4 Total energy vent

Modern total energy probes are positioned ahead and away from the surface of the sailplane to measure free stream air and prevent disturbed air from creating false readings on the variometer (FAA, 2013; Nicks, 1976). This, however, is not necessary as long as the probe measures a C_P of -1 and is preferably located on surfaces not influenced by the fuselage and

wings. In 1952 Hugh Kendall published the design of total energy measuring vents in the form of blisters along the nose of a sailplane (Figure 2-15) (Kendall, 1952).

The blisters were positioned on each side at the assumed zero pressure point of the nose. The inlet was located at the highest point of the blister and the insert was threaded and fitted through the fuselage to adjust the height thereof in flight. The two vents were connected together with rubber tubing and connected to the outlet of the variometer and the suction side of the airspeed indicator. The position errors were almost the same as other airspeed indicators. The suction improved with increased airspeed and the variometer was insensitive to fluctuations in the airspeed over short periods.

In 1952 Philip Wills moved from 27th to 1st place in the world championships by using the total energy blister (Wills, 1952). According to Wills he preferred the blisters over the Irving venturi due to the manufacturing costs being significantly less, but that the blisters would require more precision and calibration as the technique of soaring changed. Therefore, as the design of sailplanes kept changing for continuous aerodynamic improvement, the design of the blister had to be adapted and tested for each and made the design redundant.

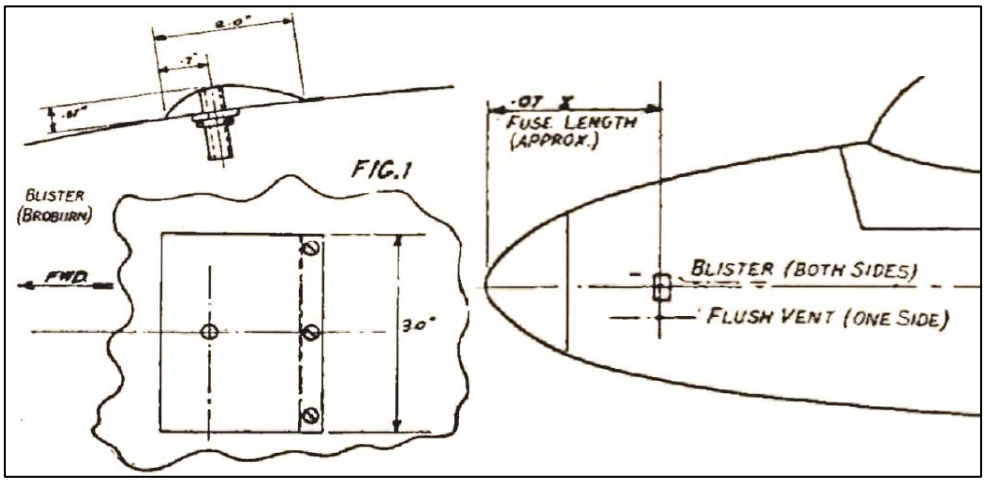

Figure 2-15: Total energy blister (Kendall, 1952)

In 2015 Frans van der Walt designed total energy measuring vents in the shape of bulges on the surface of a vertical tail fin (Figure 2-16) (Van der Walt, 2015). A Nicks total energy sensor was tested along with the bulges in a wind tunnel and compared to CFD data obtained and the theoretical pressure drop expected to be measured by the bulges (Figure 2-17). The CFD showed that the bulge design responded better than the Nicks total energy sensor, however, the wind tunnel tests showed otherwise. The bulge design can be improved through further design and accurate manufacturing techniques.

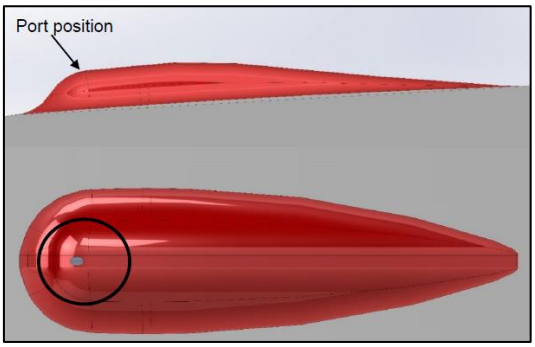

Figure 2-16: **Total energy bulge (Van der Walt, 2015)**

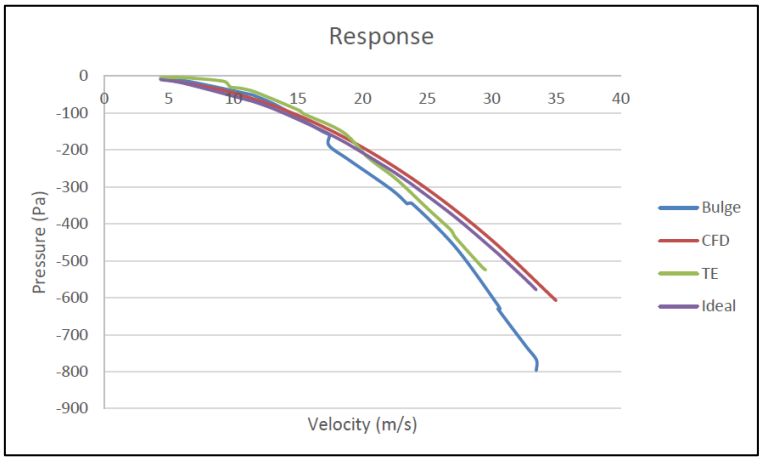

Figure 2-17: **Bulge response compared to a Nicks total energy sensor, CFD and theoretical data (Van der Walt, 2015)**

The aerodynamic design of a sailplane is based on the boundary layer theory, where the presence of probes on the external surface can disturb the layer and induce unnecessary drag.

2.5 Boundary layer theory

A boundary layer is a thin layer of medium (air) that forms on the surface of an object (aerofoil) moving through it due to the shear stresses induced by the viscosity of the medium and the pressure exerted on the medium by the object (Figure 2-18) (Anderson, 1991; McCormick, 1979). The air particles on the surface of an aerofoil slow down to a standstill, causing the successive particles in the upper boundary to slow down due to shear stresses. This thin layer of slow moving air flows along the aerofoil and is known as the laminar boundary layer. At some distance from the leading edge disturbances, such as surface roughness, can no longer be suppressed and the laminar boundary transitions to a turbulent boundary.

The turbulent boundary layer is thicker than the laminar boundary with a velocity profile of fluctuating, superimposed velocity components. Toward the trailing edge the air experiences an increase in static pressure which tends to oppose the flow. The slower boundary layer is unable to resist the adverse pressure gradient and separates from the aerofoil.

Reverse flow occurs along the aerofoil after the separation point with the static pressure almost constant and equal to that of the separation point. Downstream of the trailing edge the separated flow closes to form a wake, which varies with the size and shape of the aerofoil.

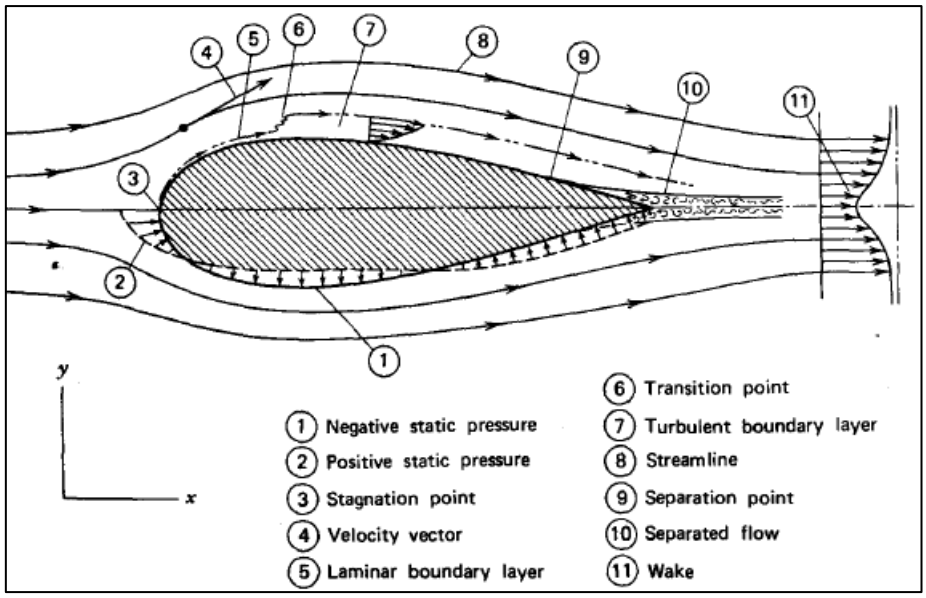

Figure 2-18: Boundary layer formation on an aerofoil (McCormick, 1979)

Oil tests can be used to visualise the boundary layer of an aerofoil (Figure 1-2) (Hendrix, 2012). The leading edge of an aerofoil is exposed to a high pressure that creates a nearly clean surface on the leading edge. The oil gradually moves along the surface to create thick streaks (laminar boundary) until it forms a bubble at the transition point. The oil escapes the bubble and speeds up to initially form smooth thin streaks and then thicker streaks toward the trailing edge (turbulent boundary).

The placement of the total energy probe on a sailplane can affect the compensation capabilities of the probe, as well as the amount of drag induced on the surface of a sailplane.

2.6 Total energy probe placement

Various areas have been identified and tested where the total energy probe can be installed. These areas include the nose, wings, fuselage, horizontal tail plane and vertical tail fin.

A probe installed into the nose of a sailplane ensures that it measures free stream air ahead of the sailplane. However, the release hook mechanism in the nose in the JS-1C leaves a small area where air is vented into the cockpit and the presence of a probe would disturb and diminish this airflow and inconvenience the pilot (Figure 2-19) (Aucamp, 2014). The probe can also be damaged by the towing cable of a tug plane as the sailplane follows indirectly to avoid the wake created by the propeller of the tug plane (Figure 2-20).

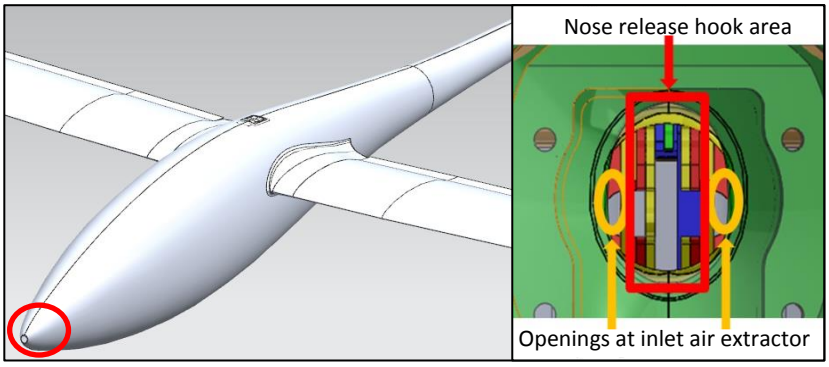

Figure 2-19: **Small openings available in the nose of the fuselage due to the release hook mechanism (Aucamp, 2014)**

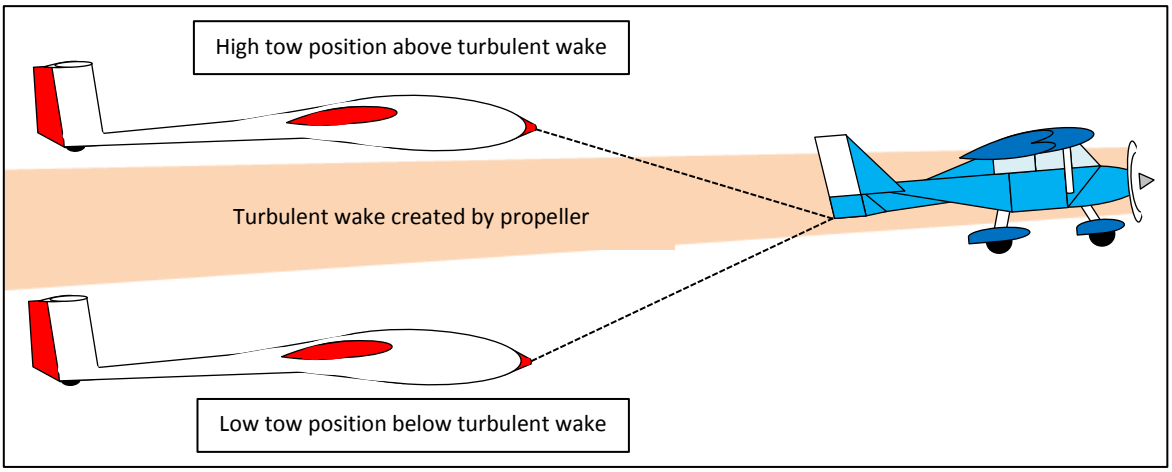

Figure 2-20: **Sailplane follows indirectly behind a tug plane to avoid the wake created by the propeller (FAA, 2013)**

A large area of the nose is subjected to laminar flow, where the probe can trigger the transition point prematurely and induce drag on the other surfaces downwind of the probe.

The placement of a probe on the wings and wing tips will cause drag on the main lift inducing surfaces of the sailplane. Another concern is that the wings need to be dismantled and/or the wing tips need to be changed. The disassembly and reassembly of the probe pneumatic line, along with the wings, is inconvenient and has a high probability for incorrect connection, leaks and damage.

A probe installed into the fuselage of a sailplane is extended away from the body to be positioned in free stream air (Figure 2-21) (Johnson, 1998; Nicks, 1976). This location is acceptable compared to the tail plane; however the probe has to be modified to provide sufficient compensation when conducting manoeuvres. The probe causes the transition point of the boundary layer to trigger prematurely, inducing drag on the surfaces downwind of the probe.

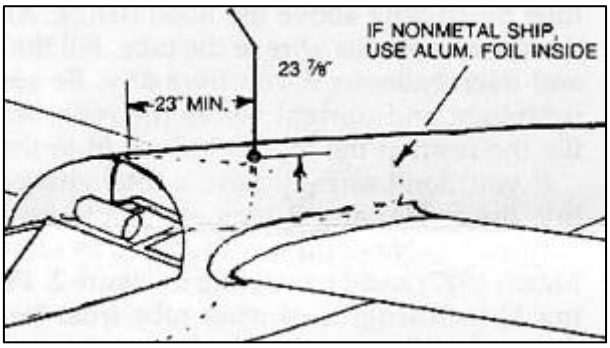

Figure 2-21: **Total energy probe modified for the fuselage (Sebald, 1981)**

The horizontal tail plane tip probe configuration is based on a Request for Change document (RFC) compiled by the company who designed the JS-1C to reduce the parasitic drag caused by the probe (Figure 2-22) (JS, 2014). No further records on the testing done by the company on the experimental concept were found. The placement can be beneficial, since minimum surface area is located downwind of the probe to induce drag. The assembly and disassembly of the tail plane, as with the wings and wing tips, could inconvenience the pilot and lead to probe line connection errors.

Figure 2-22: **The total energy probe on the JS-1C moved to the tip of the horizontal tail plane (JS, 2014)**

The tail fin is identified as the best area to install a total energy probe, where the probe is positioned ahead of the fin in free stream air and the pressure over the wings and body rarely affect the probe (Figure 1-2) (Nicks, 1976). However, a large part of the fin is subjected to laminar flow, which the probe prematurely triggers to turbulent to induce drag over the surface of the fin.

The characteristics of the total energy probe can be analysed during various flight manoeuvres to determine its compensation capabilities.

2.7 Total energy system testing

There are two simple tests used to determine the compensation characteristics of a total energy probe during climb, dive and sideslip (skid or slip sideways that causes rotation in the vertical axis) manoeuvres.

2.7.1 Climb and dive manoeuvre test

A straight and inclined trajectory manoeuvre is used to evaluate the compensation of the probe during a dive and climb (Figure 2-23). The test is conducted early morning before thermals become active (Brözel, explained by Knauff & Nadler, 2002):

1. Fly at the speed for minimum sink or minimum speed plus 10 km/h (V_{MIN}) and maintain for 10 seconds. The sink rate is defined as the rate of descent measured in still air, for example, a sink rate of 1 m/s means the sailplane loses 1 metre of altitude every second as it flies through still air.
2. Push steadily forward into a dive of 10° to 15° pitch nose down attitude and maintain. Any dust should remain on the floor with little to no G-forces indicated.
3. Pull back before reaching the never exceed speed (V_{NE}) into a climb of 10° to 15° pitch nose up attitude and maintain. A typical load factor between 2 G to 3 G should be indicated.
4. Level out at 0° attitude at the speed specified in the first step.

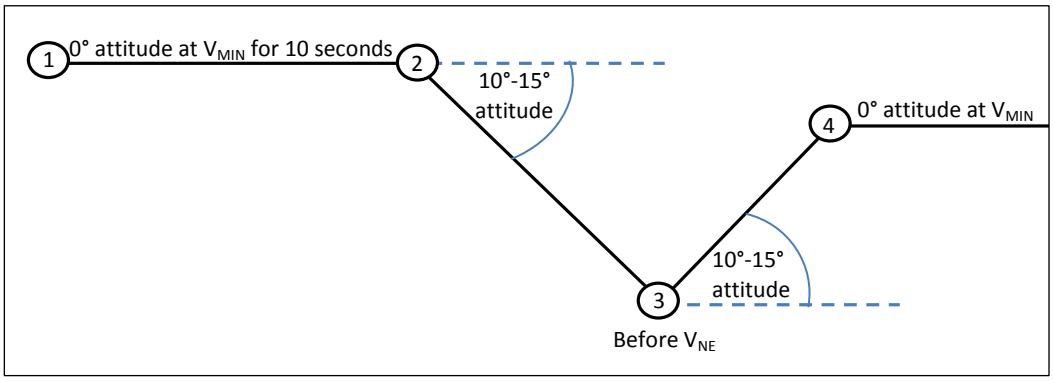

Figure 2-23: Straight and inclined trajectory manoeuvre

The following will be observed if the system compensates adequately (Brözel, explained by Knauff & Nadler, 2002):

1. The actual minimum sink rate of the sailplane is indicated.
2. The G-force is smaller than one when entering the dive and the variometer indicates close to zero. The position of the total energy probe aft of the centre of gravity on the vertical tail fin causes the positive excursion of the system to increase due to the effect of the longitudinal air column between the variometer and the probe. The effect becomes stronger due to the length of the air column and pitch changes, which should not exceed a total reading of approximately 5 m/s.
3. The airspeed will increase linearly with time in the dive and the proper sink rate corresponding to the actual airspeed is indicated. However, the sink rate indicated will be delayed due to the response rate of the variometer.

4. A deflection in the negative direction is indicated when pulling out of the dive and the indicator gradually moves from the negative to the positive direction in the climb as the speed decreases.

The average readings in observation three and four should correspond to the actual sink rate of the sailplane (Brözel, explained by Knauff & Nadler, 2002).

2.7.2 Sideslip manoeuvre test

In a strong thermal it is nearly impossible to maintain a zero sideslip angle due to air circulation within a thermal (Brözel, explained by Knauff & Nadler, 2002). The influence of sideslip can be tested by inducing a sideslip of 30° and maintaining for 3 seconds (Figure 2-24). The sideslip is then straightened without haste and the sailplane prevented from rolling and pitching throughout the manoeuvre.

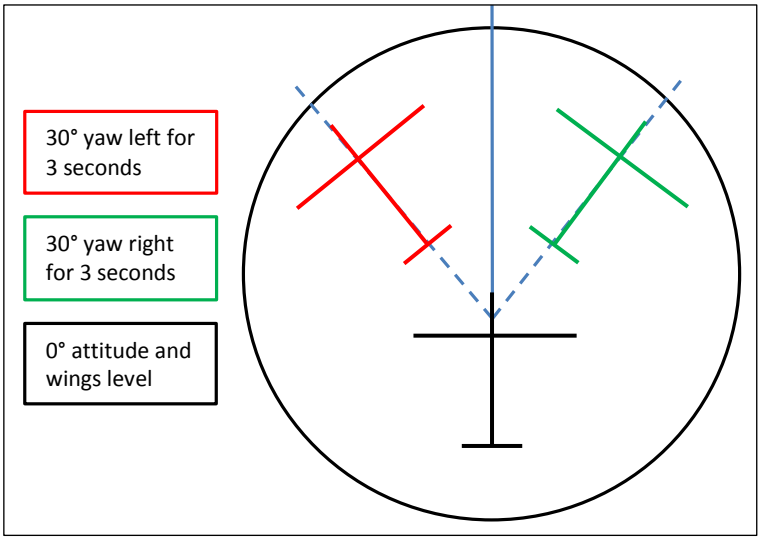

Figure 2-24: Sideslip manoeuvre test

The variometer should transit steadily and smoothly from strong sink to the actual sink rate (Brözel, explained by Knauff & Nadler, 2002). The absolute value indicated during the manoeuvre is not important; only the smooth transition is required. However, the variometer should not indicate less than the actual sink rate after the manoeuvre is completed.

A conclusion of the literature study was created to briefly summarise the elements described therein.

2.8 Conclusion

The literature required to complete the dissertation was shortly summarised and conclusions were made based on the information obtained.

The basic principles of total energy compensation are explained and how a variometer reflects this information in-flight based on surrounding lift sources. A theoretical model of an ideal total energy probe can be created to determine the maximum pressure a total energy probe configuration or design may measure.

The effect of obstructions (such as external sensors) on the airflow over aerofoils and other surfaces are discussed that can change the aerodynamic performance of a sailplane. Alternative areas on a sailplane where external sensors can be installed based on possible benefits and losses were identified where the total energy probe can be moved to or redesigned for. The total energy probe configuration or design must promote drag reduction in the new or current location without reducing the compensation capabilities of the probe. The vertical tail fin, horizontal tail plane and fuselage should be considered for alternative locations and any changes to the wings should be avoided to ensure maximum lift generation.

The compensation characteristics of a total energy probe during different flight manoeuvres can be evaluated in-flight. Flight test data is required to determine the current compensation capabilities of the total energy probe installed on the JS-1C. The data will establish the minimum compensation characteristics and maximum drag criteria for total energy probe configurations and designs.

A theoretical model that replicates an ideal total energy probe was created to calculate the maximum pressure a total energy probe design may measure in straight and level flight without exceeding that of the theoretical model (over-compensation).

CHAPTER 3: THEORETICAL TOTAL ENERGY PROBE COMPENSATION

Two theoretical models are presented, namely a simple model where altitude gain is linear and a more realistic model where altitude gain is non-linear. Both models represent a sailplane flying through still air and through a thermal. For the calculations presented, a sailplane travelling at an initial velocity of 60 m/s gains 150 meters in one minute. Standard mean sea level conditions are assumed.

3.1 Linear altitude gain

The simple model represents a sailplane gaining altitude by flying in a straight line from mean sea level (zero altitude) to 150 metres. Altitude gain in such a manner is not realistic, but serves as a simple method to explain the compensation characteristics of a basic total energy probe and the theory of flow around a cylinder.

3.1.1 Altitude gain in still air

In still air where the total energy remains constant, the sailplane has an initial local pressure of:

$$\mathrm{P_{local1}} = \mathrm{P_{static1}} - \mathrm{P_{dynamic1}} = 101\,325 - (0.5 * 1.225 * 60^2) = 99\,120\ \mathrm{Pa}$$

The pressure coefficient is:

$$\mathrm{C_{p1}} = \frac{\mathrm{P_{local1}} - \mathrm{P_{static1}}}{\mathrm{P_{dynamic1}}} = \frac{99\,120 - 101\,325}{0.5 * 1.225 * 60^2} = -1$$

The sailplane increases its altitude by 150 metres and reaches a velocity of:

$$\mathrm{mgh_1} + ½\mathrm{mV_1}^2 = \mathrm{mgh_2} + \mathrm{mV_2}^2$$

$$½\left(60^2 - \mathrm{V_2}^2\right) = \mathrm{g}(150 - 0)$$

$$\mathrm{V_2} = 25.6\ \mathrm{m/s}$$

The change in density due to altitude is assumed constant and, therefore, the new static pressure is:

$$\mathrm{P_{static2}} = \mathrm{P_{static1}} - \rho \mathrm{g} \Delta \mathrm{h} = 101\,325 - (1.225 * 9.81 * 150) = 99\,522.4\ \mathrm{Pa}$$

The new local pressure and pressure coefficient is:

$$P_{local2} = P_{static2} - P_{dynamic2} = 99\,522.4 - (0.5 * 1.225 * 25.6^2) = 99\,120 \text{ Pa}$$

$$C_{p2} = \frac{P_{local2} - P_{static2}}{P_{dynamic2}} = \frac{99\,120 - 99\,522.4}{0.5 * 1.225 * 25.6^2} = -1$$

This corresponds with the theory that a total energy probe will sufficiently compensate for changes in velocity and altitude when the total energy remains unchanged (Figure 3-1 and Figure 3-2).

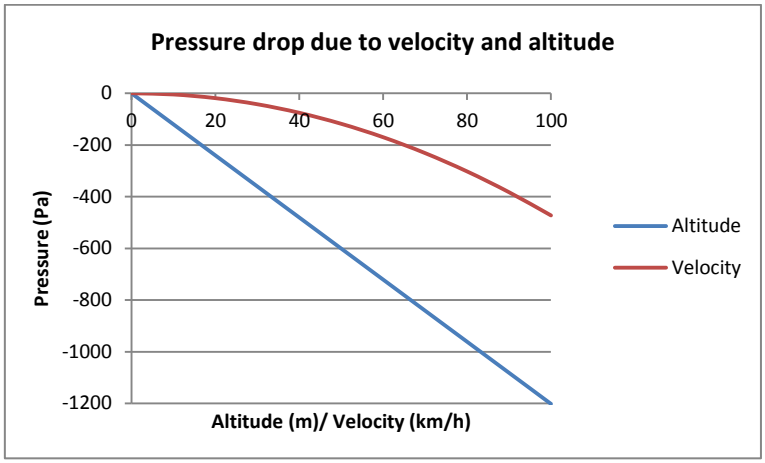

Figure 3-1: **Total energy probe response to change in altitude and velocity**

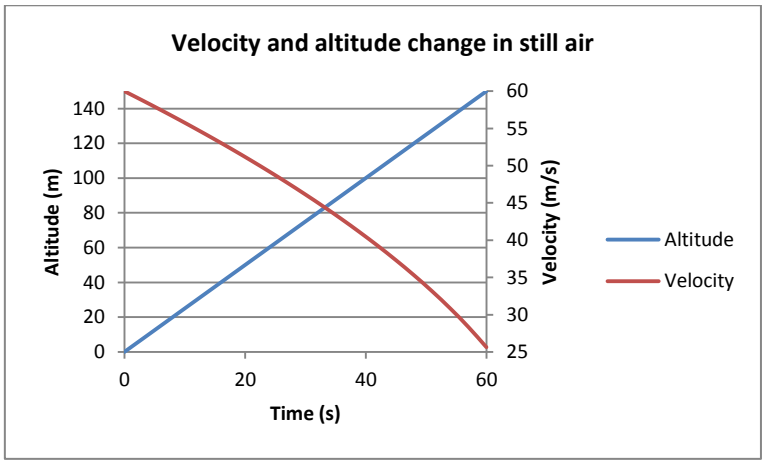

Figure 3-2: **Velocity and altitude change in still air for linear altitude gain**

In a climb, the potential energy increases as altitude is gained and kinetic energy reduces as speed is lost. The total energy remains constant as the kinetic energy is converted to potential energy (Figure 3-3). The total pressure measured by the total energy probe must remain constant to ensure the variometer reads zero during the ascent. Therefore, as atmospheric pressure decreases with altitude gain, the dynamic pressure must decrease as the velocity decreases (Figure 3-4). The dynamic pressure measured by the total energy probe is negative, because the orifice is located downwind of the probe and creates a vacuum.

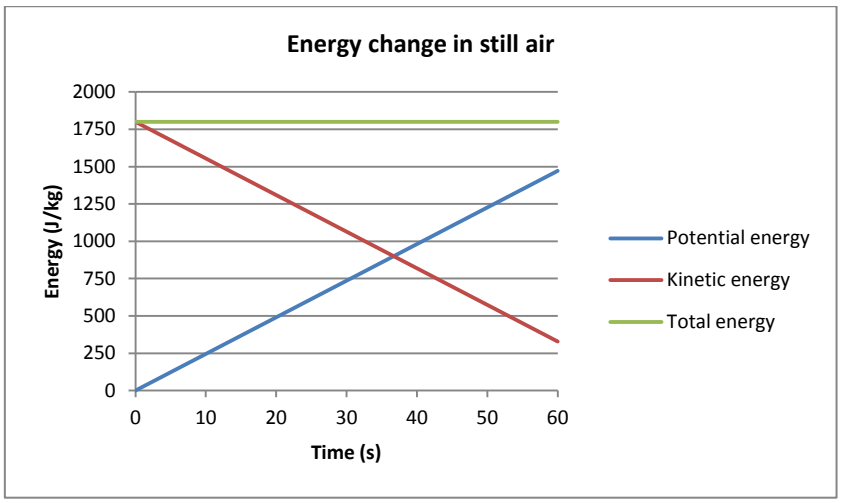

Figure 3-3: **Energy change in still air for linear altitude gain**

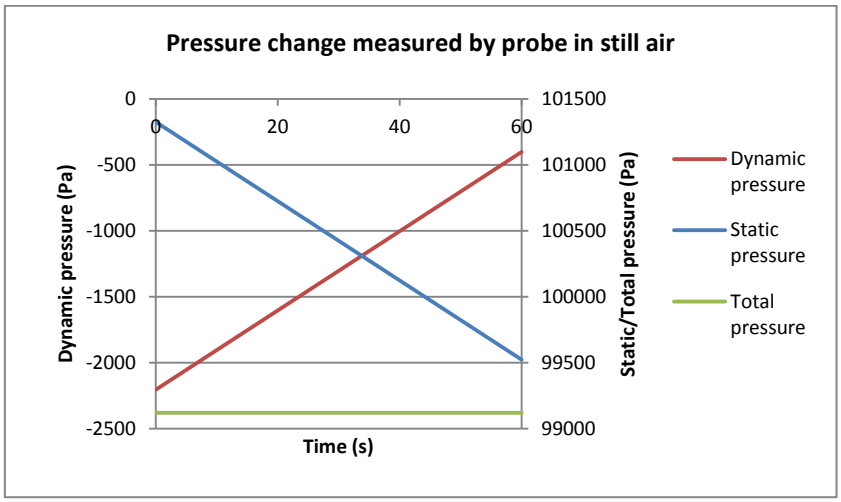

Figure 3-4: **Pressure change measured by the total energy probe in still air for linear altitude gain**

The pressure drop measured by the total energy probe due to altitude is linear, while the pressure drop due to velocity is quadratic (Figure 3-5).

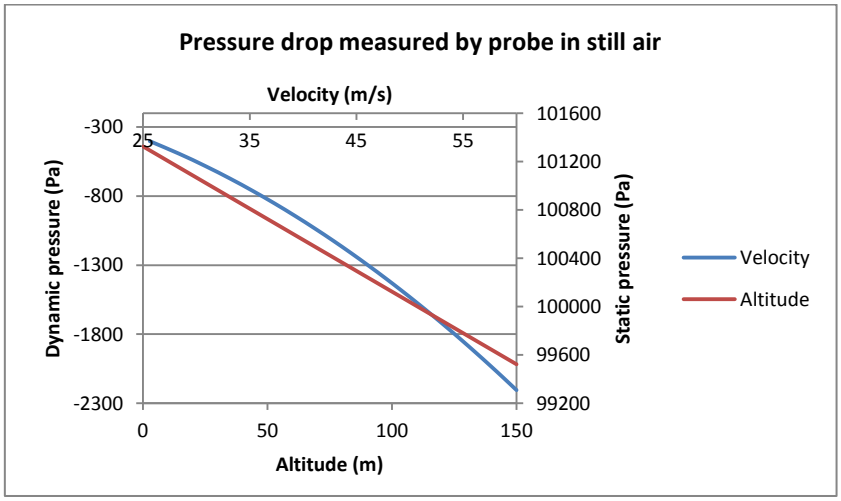

Figure 3-5: **Pressure drop measured by the total energy probe in still air for linear altitude gain**

The same principles are applied when the sailplane flies through a thermal.

3.1.2 Altitude gain in a thermal

The sailplane gains altitude in a thermal without having to reduce speed (Figure 3-6). The kinetic energy remains constant, while the potential energy increases with altitude gain. Since the kinetic energy is not converted to potential energy, the total energy increases (Figure 3-7). The total pressure measured by the total energy probe decreases as the static pressure decreases and the variometer indicates a reading greater than zero during the ascent (Figure 3-8).

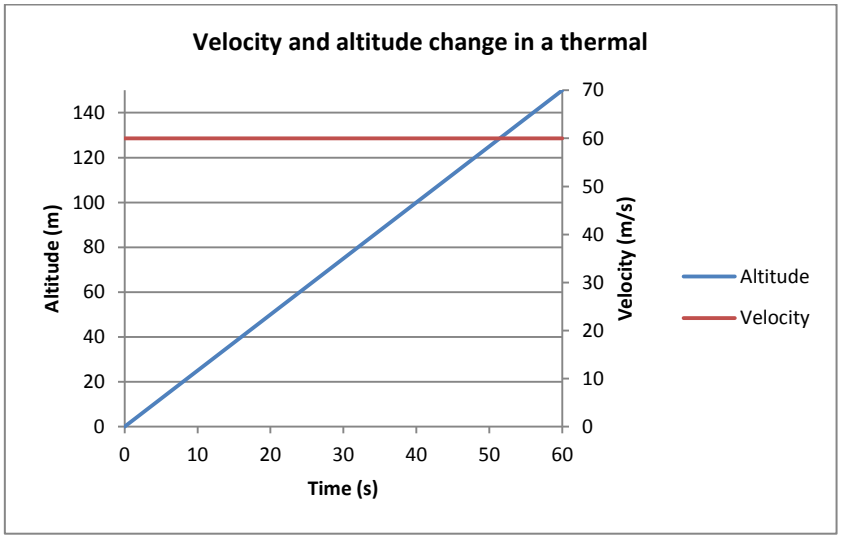

Figure 3-6: **Velocity and altitude change in a thermal for linear altitude gain**

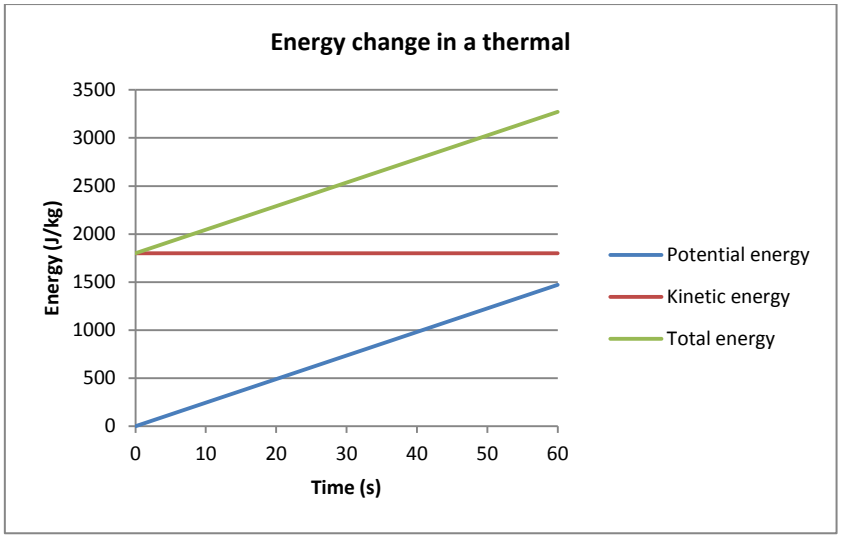

Figure 3-7: **Energy change in a thermal for linear altitude gain**

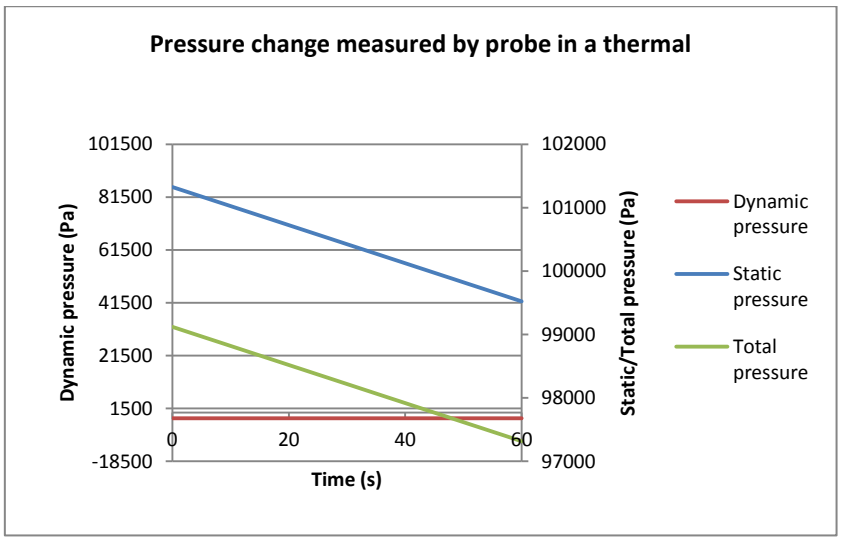

Figure 3-8: **Pressure change measured by the total energy probe in a thermal for linear altitude gain**

A more realistic model with non-linear altitude gain can be created using the same principles as the simple, linear altitude gain model.

3.2 Non-linear altitude gain

The more realistic model represents a sailplane gaining altitude by flying in what resembles an s-curve with the same parameters as that of the simple model.

3.2.1 Altitude gain in still air

A pilot gains altitude in still air by pulling the sailplane into a climb (1) until it reaches the best angle of climb, where the most altitude is gained in the least amount of time or ground distance travelled. This angle is maintained (2) just before the desired altitude is reached and the pilot (3) levels the sailplane out of the climb at the desired altitude (Figure 3-9).

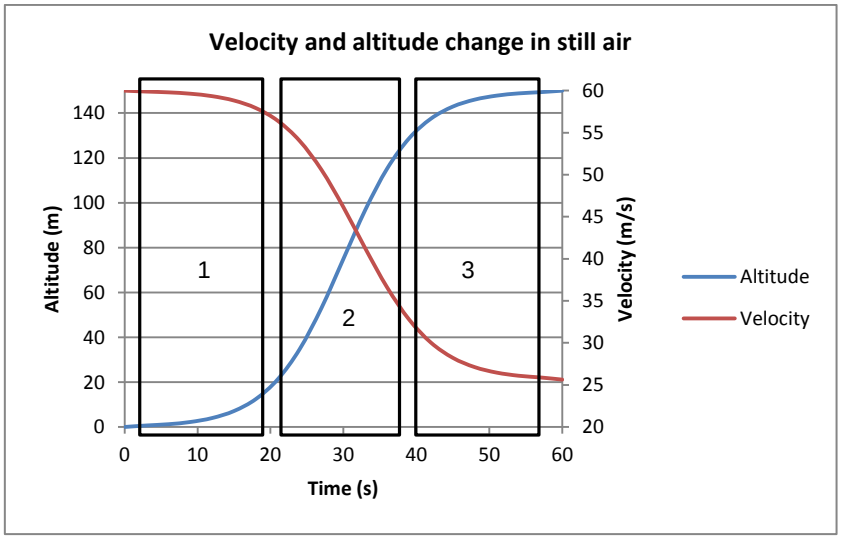

Figure 3-9: **Velocity and altitude change in still air for non-linear altitude gain**

As with the simple model, both the total energy (Figure 3-10) and pressure (Figure 3-11) remain unchanged as the kinetic energy is converted to potential energy in still air during the ascent.

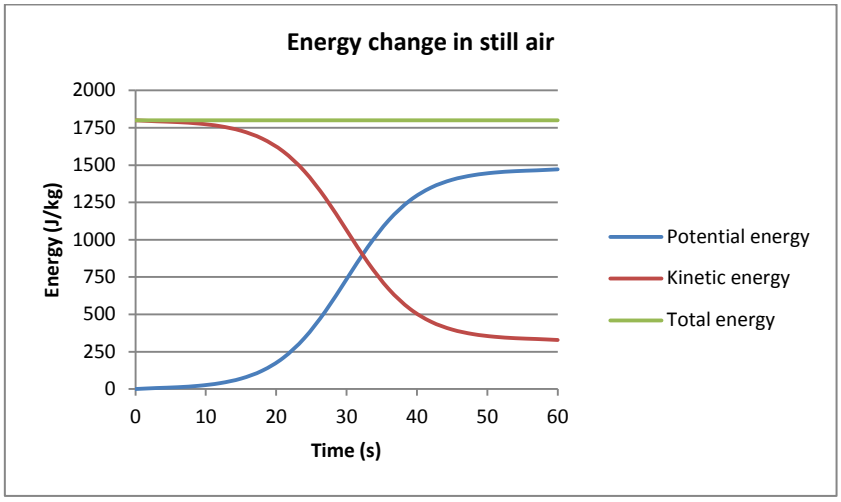

Figure 3-10: **Energy change in still air for non-linear altitude gain**

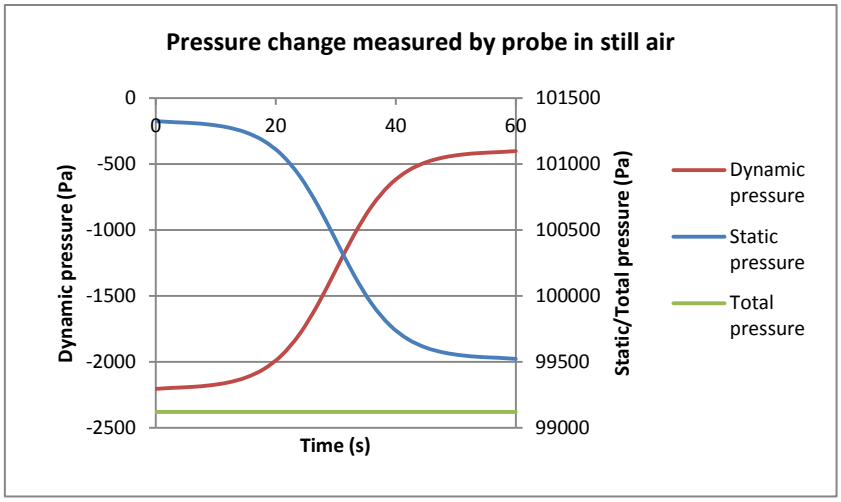

Figure 3-11: **Pressure change measured by the total energy probe in still air for non-linear altitude gain**

The same principles also apply to the non-linear model when flying through a thermal.

3.2.2 Altitude gain in a thermal

The sailplane gains altitude without reducing speed using the additional lift generated by the thermal (Figure 3-12). The total energy increases (Figure 3-13), since the kinetic energy is not converted to potential energy and the total pressure measured by the total energy probe decreases (Figure 3-14) as the static pressure decreases due to the vacuum.

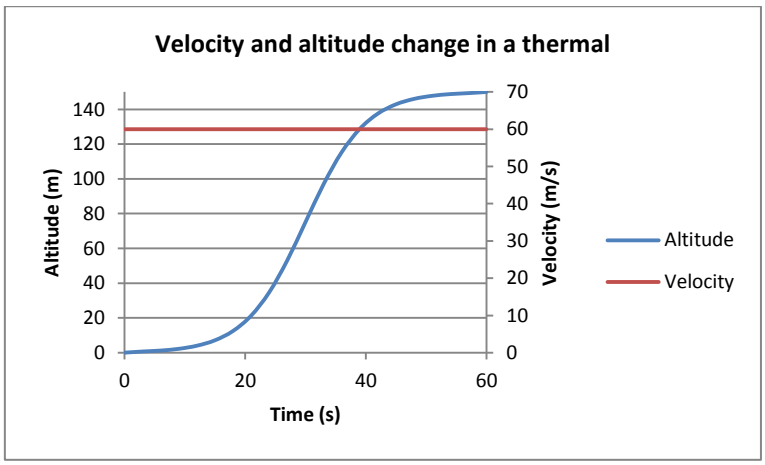

Figure 3-12: **Velocity and altitude change in a thermal for non-linear altitude gain**

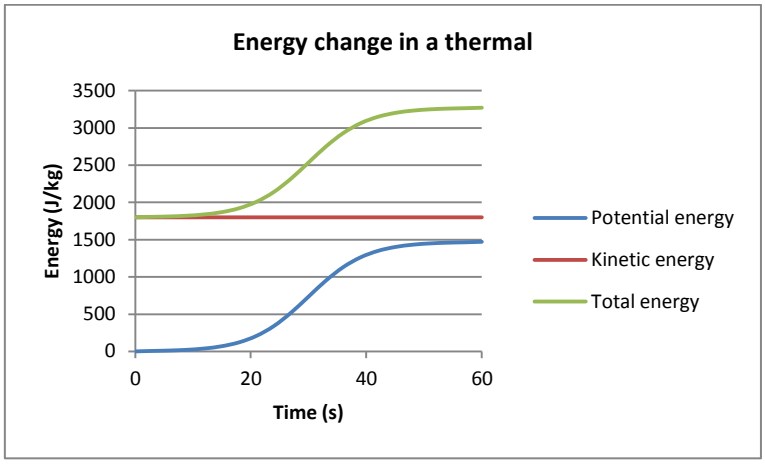

Figure 3-13: **Energy change in a thermal for non-linear altitude gain**

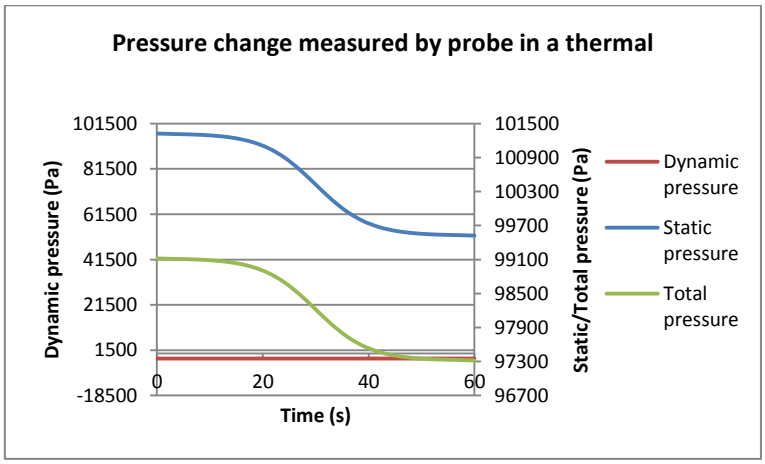

Figure 3-14: **Pressure change measured by the total energy probe in a thermal for non-linear altitude gain**

The theoretical altitude gain of a sailplane is much more complex than presented, as the thermal itself can influence the climbing performance of a sailplane, namely the strength and stability of the thermal.

3.3 Conclusion

Theoretical models of an ideal total energy probe in still air and through a thermal were created for both simple and complex altitude gain. The models explain the principle of total energy compensation and how a pilot uses a variometer to visually exploit this principle to identify lift sources for prolonged flight and altitude gain.

The models presented can be compared to the current total energy probe to determine the minimum pressure a total energy probe configuration or design may measure in straight and level flight without measuring less than that of the current probe (under-compensation). The probe may not measure a pressure coefficient greater than the theoretical C_P of -1 to prevent over-compensation.

A simple, baseline CFD program was created to recreate and analyse different total energy probe designs and configurations, all with the same setup and settings, for more accurate comparison.

CHAPTER 4: COMPUTATIONAL FLUID DYNAMICS SETUP

The chapter describes the setup of a simulation created in StarCCM+ CFD software for a model suspended in a wind tunnel. The aim is to create a baseline CFD program that can be used to analyse different designs or configurations, all with the same setup and settings, for more accurate comparison. Note that models that intentionally touch the walls of the wind tunnel, such as a car where the behaviour of the airflow between the car and road is desired, require additional settings that are not discussed.

4.1 Create the CAD models

Create solids of the wind tunnel and model, in this case the JS-1C, using any CAD software capable of exporting generated solids as parasolids. The sailplane is symmetric and only the tail section thereof is of interest for the base analysis: therefore, both the sailplane and wind tunnel models were halved and only the tail section kept (Figure 4-1). This simplifies the simulation by reducing the surface area and complex geometry the mesh is applied to, which minimizes the simulation and makes it faster.

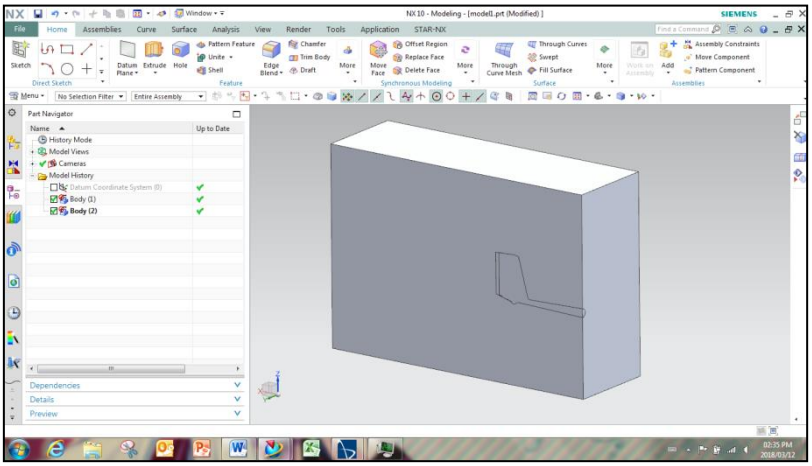

Figure 4-1: Sailplane and wind tunnel block solids created in CAD software

Export the two models separately as parasolids. The creation of separate bodies enables easy editing of the CFD when the model changes or different configurations/modifications are compared.

4.2 CFD program setup

Create a new simulation, and a 3D-CAD model in the “Geometry” folder (Figure 4-2). Import the two parasolids created, with the wind tunnel block imported first. The software assigns the first body imported as the main body and all other bodies after that as tools.

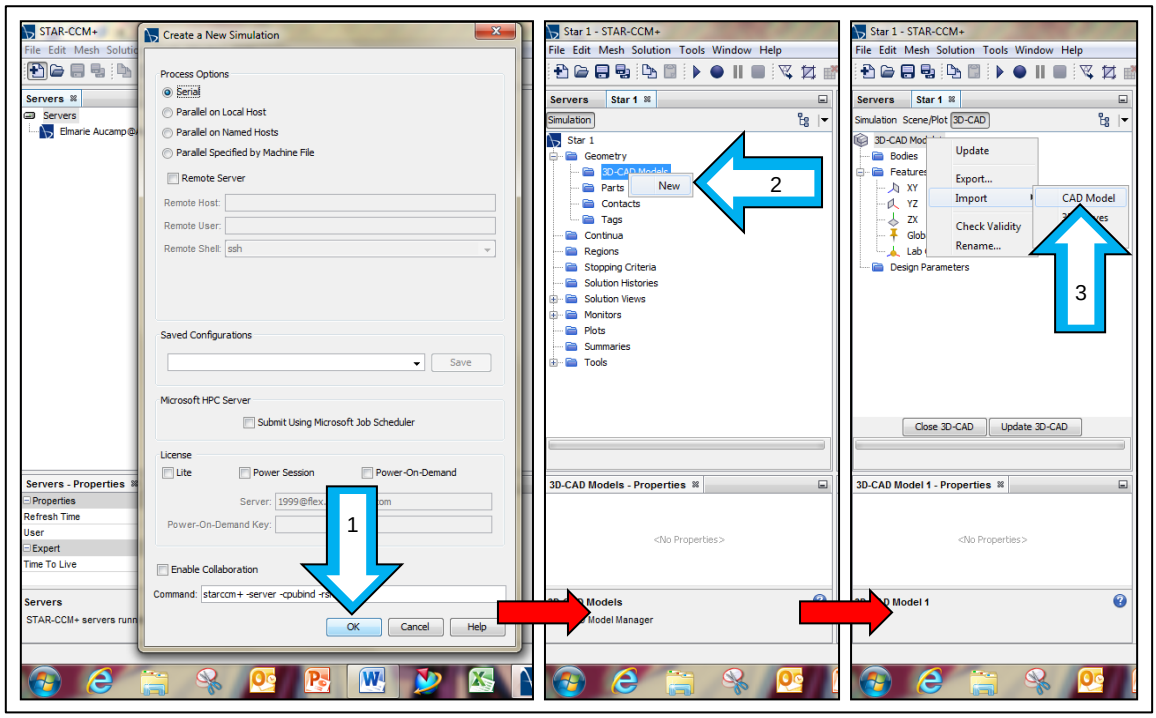

Figure 4-2: **A new simulation and 3D-CAD model created in CFD software**

Subtract the imported bodies listed in the “Bodies” folder to create a single body (Figure 4-3). Note that the software assigned the wind tunnel block as the main body and the other as the tool. Update the 3D-CAD model and close it.

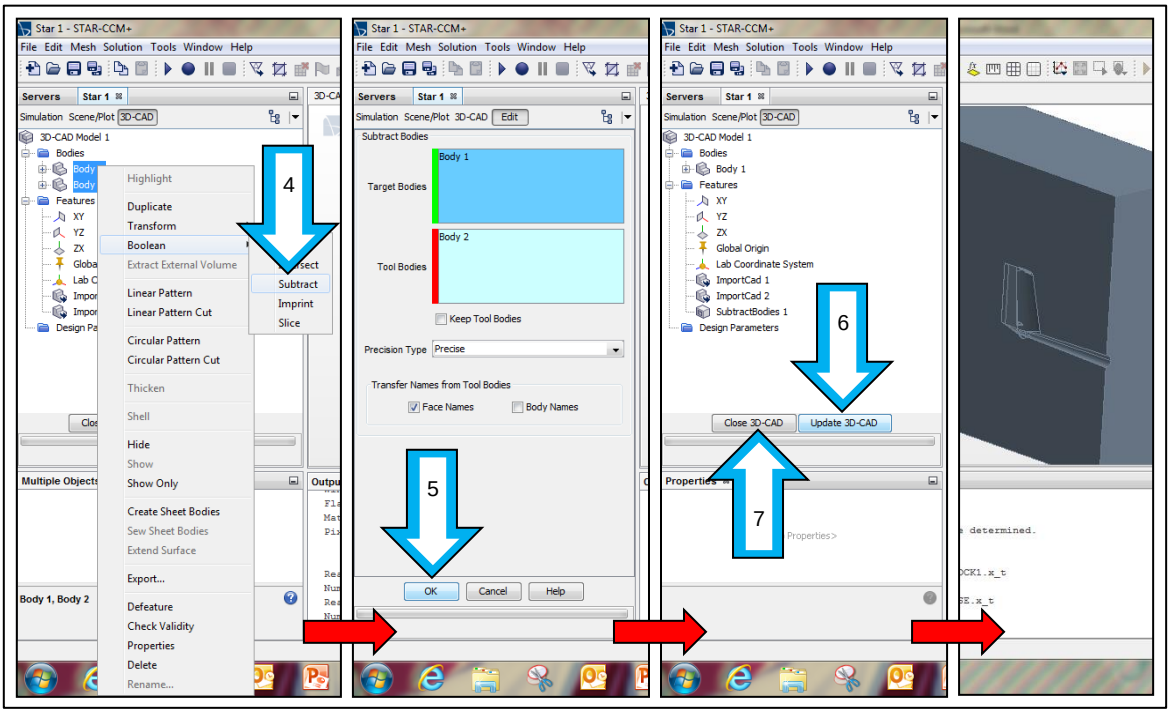

Figure 4-3: **Single body created by subtracting the imported parasolids**

Create a new geometry part from the 3D-CAD model, deselect the “Create Part Contacts from Coincident Entities” option and create a new geometry scene (Figure 4-4).

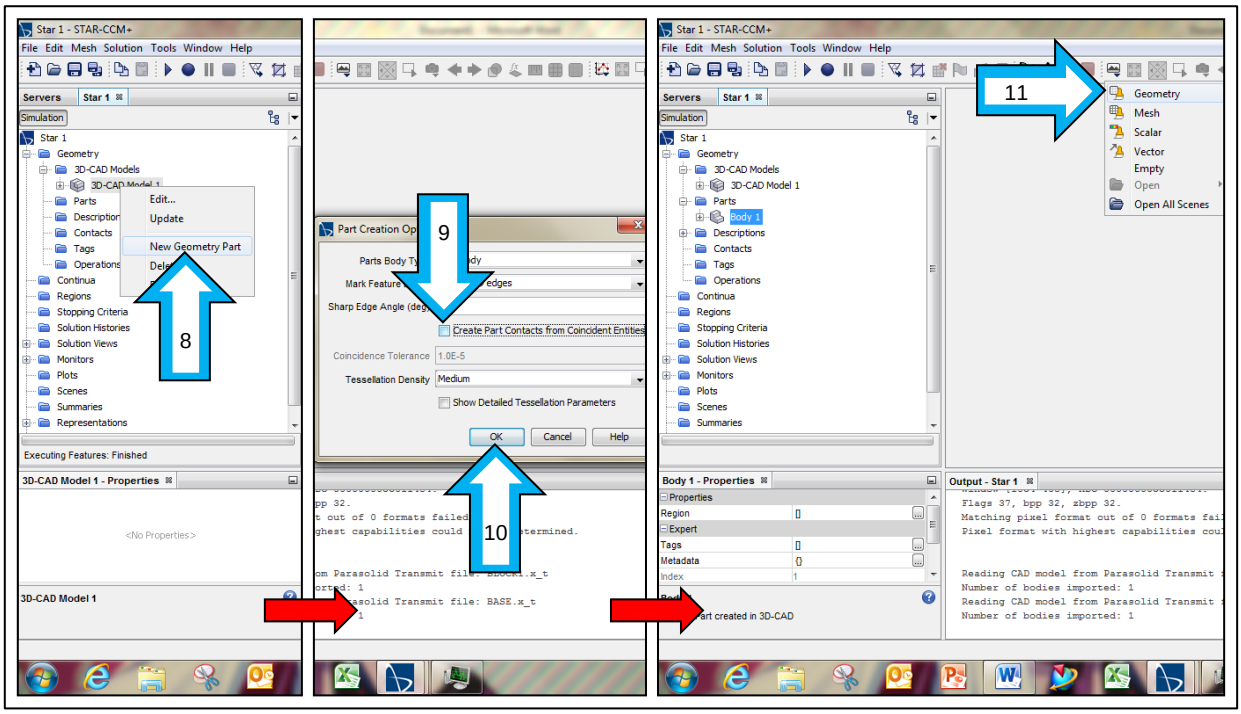

Figure 4-4: A new geometry part created from the 3D-CAD model with its own geometry scene

Repair the surfaces of the geometry part and the CAD itself (Figure 4-5 and Figure 4-6).

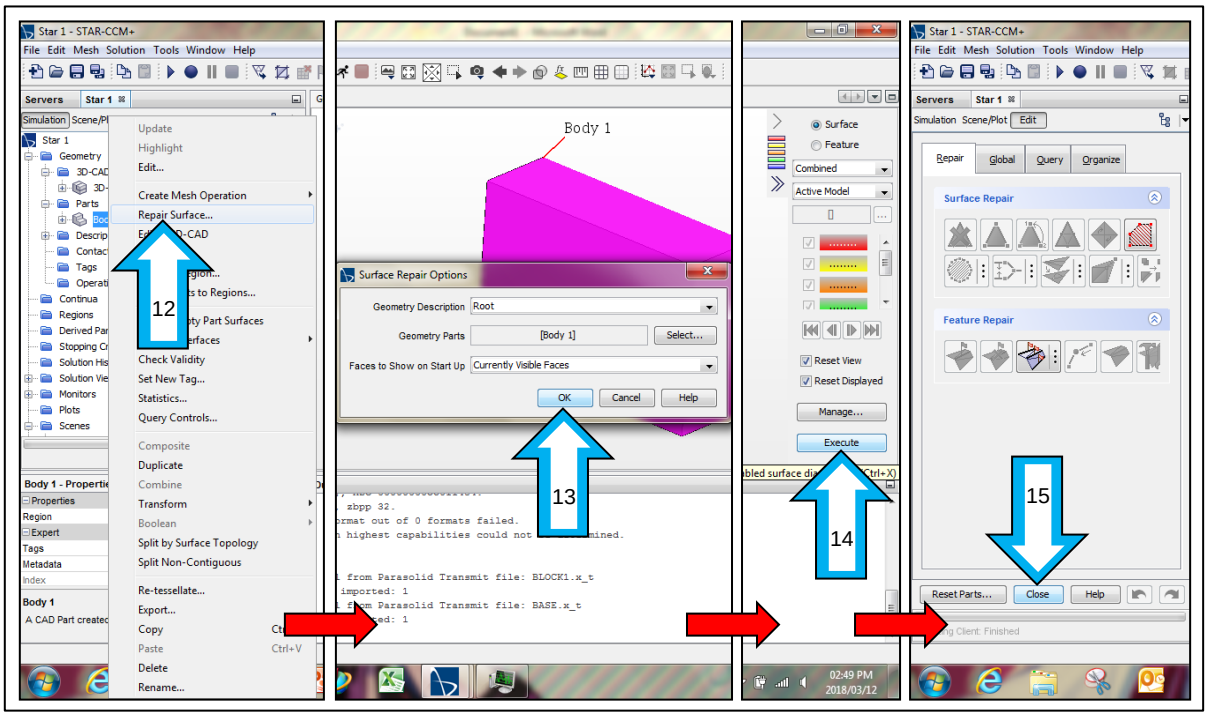

Figure 4-5: Surfaces of the geometry part evaluated and repaired

Split the surfaces of the geometry part into sections that separate the various wind tunnel surfaces from the tail section surfaces. Select the surface that bears the impression of the tail section in the geometry scene, assign it a name (in this case “Split plane”) and select “Create” (Figure 4-7).

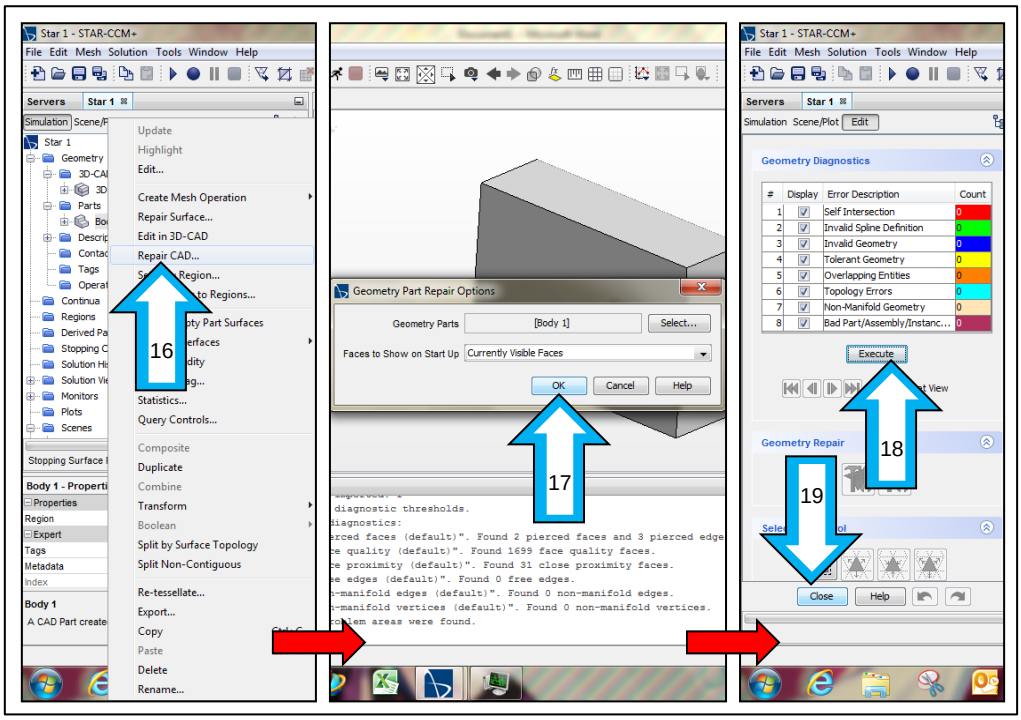

Figure 4-6: **Geometry part CAD evaluated and repaired**

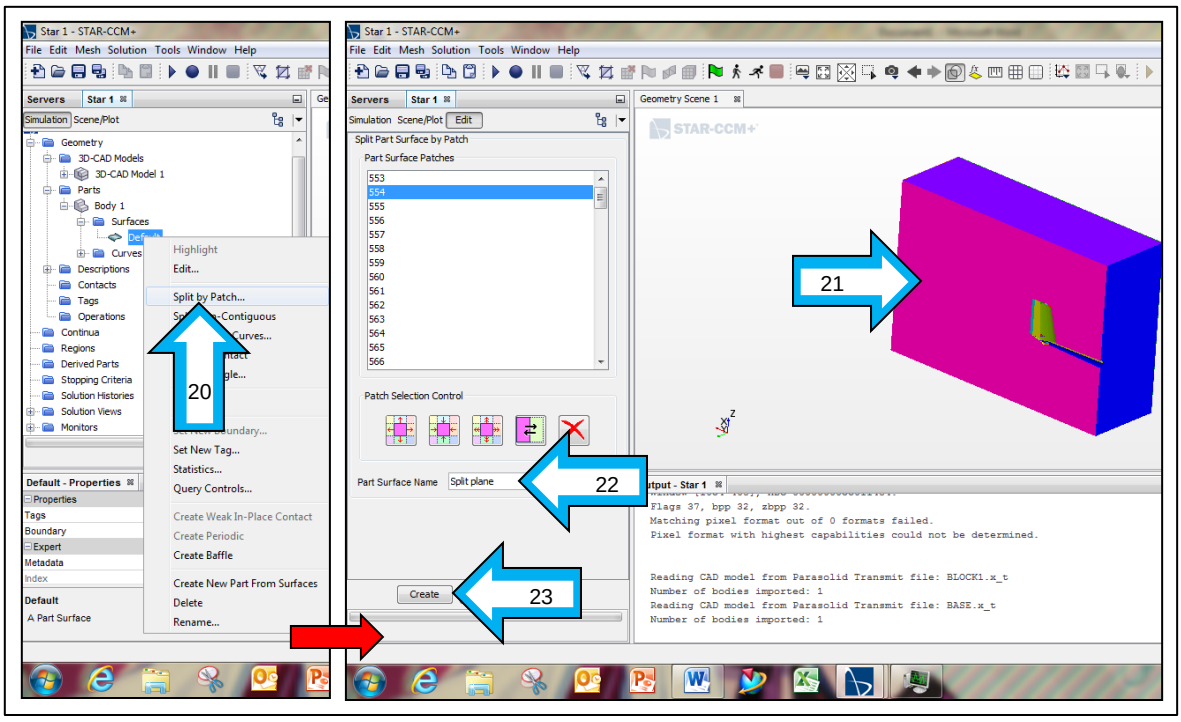

Figure 4-7: **Split the surface of the geometry part to create the split plane**

Split the rest of the wind tunnel block surfaces into the wind tunnel inlet, outlet and outer walls (Figure 4-8). The remaining surfaces represent the tail section, namely the “Sailplane” surface.

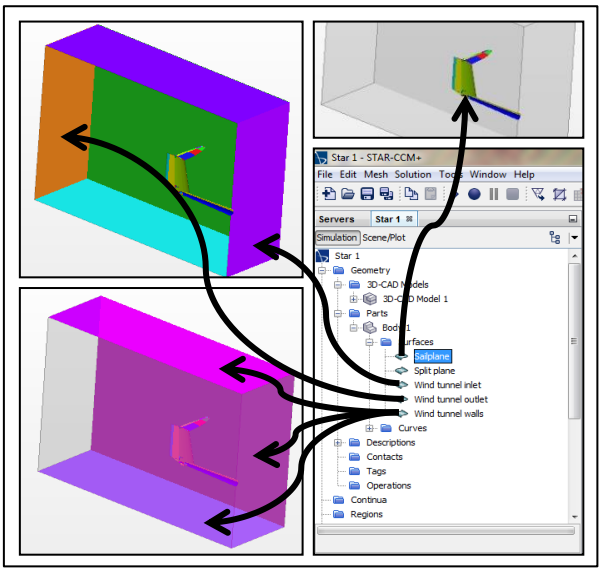

Figure 4-8: **Remaining geometry part surfaces split into sections**

Assign the surfaces to a single region and create a boundary for every surface (Figure 4-9).

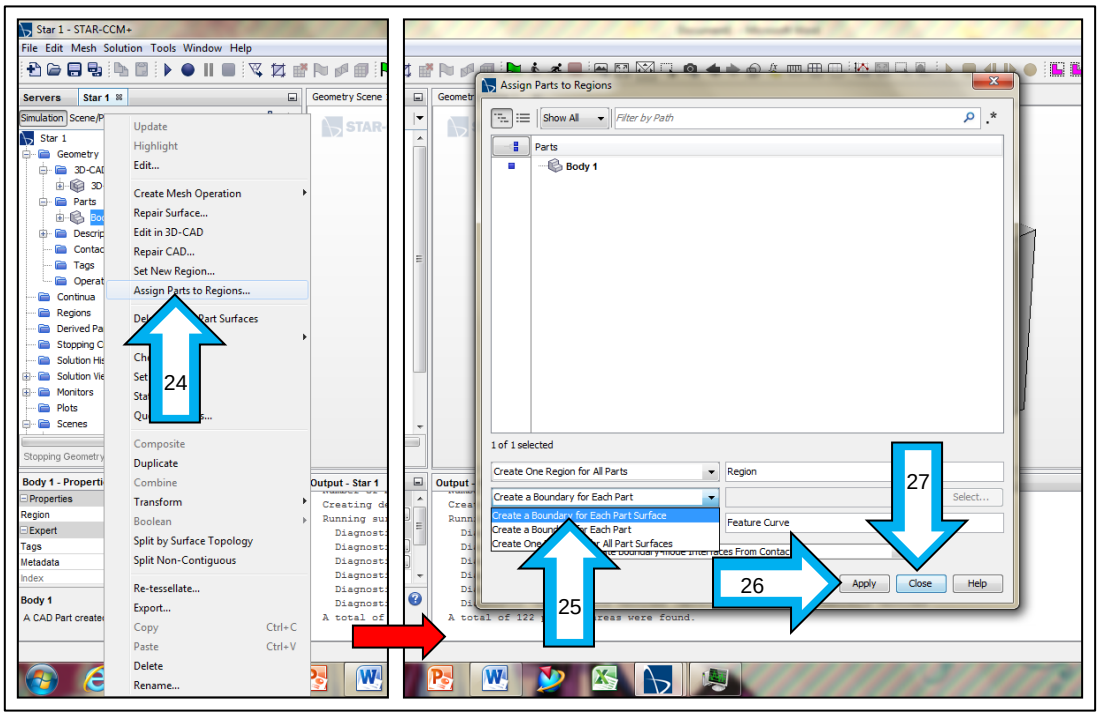

Figure 4-9: **Assign the geometry part surfaces to a single region with each their own boundary**

Create a new mesh continuum in the “Continua” folder and assign meshing properties (Table 4-1). Discretion is used when selecting the mesh type, where in this case the polyhedral mesh was chosen.

Table 4-1: **Mesh continuum properties**

Category	Property
Surface mesh	Surface remesher
Volume mesh	Polyhedral mesher
Optional models	Prism layer mesher

Note that the software automatically transfers each selection to the right side of the command screen to the “Enabled Models” category (Figure 4-10).

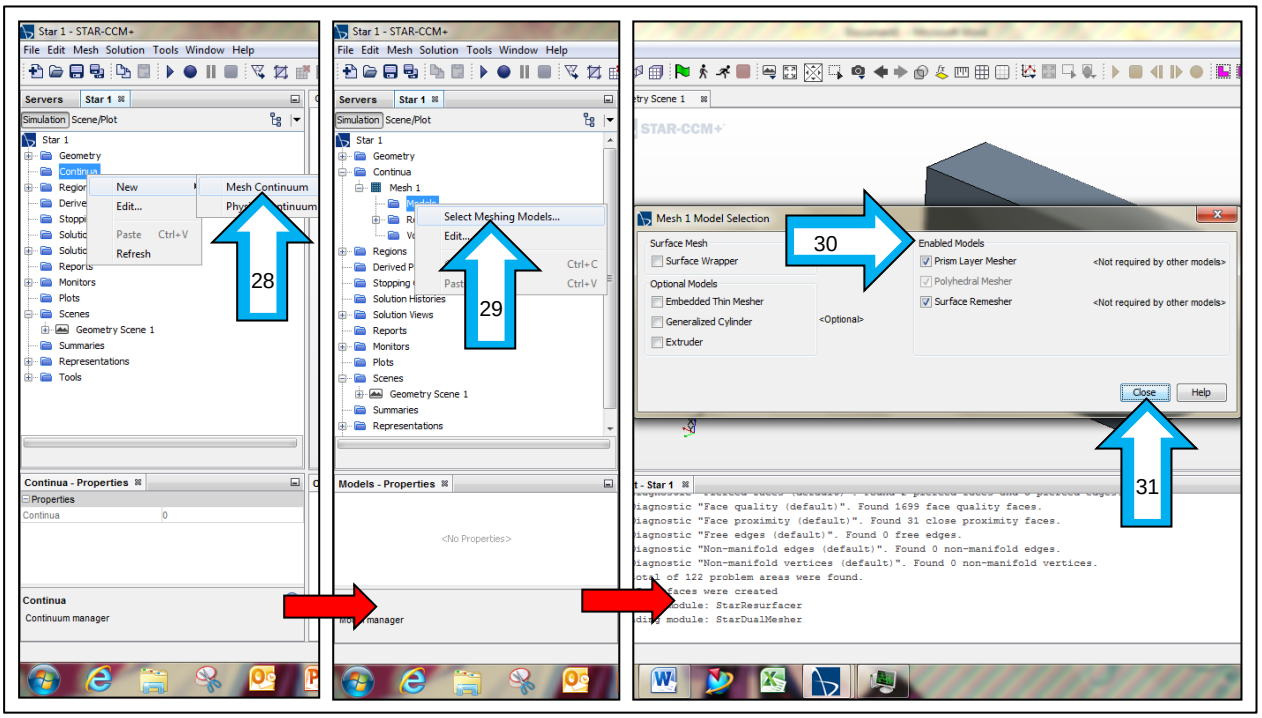

Figure 4-10: Create a new mesh continuum

Change the number of prism layers to 15 and the prism layer thickness to an absolute value of 6 mm (Figure 4-11).

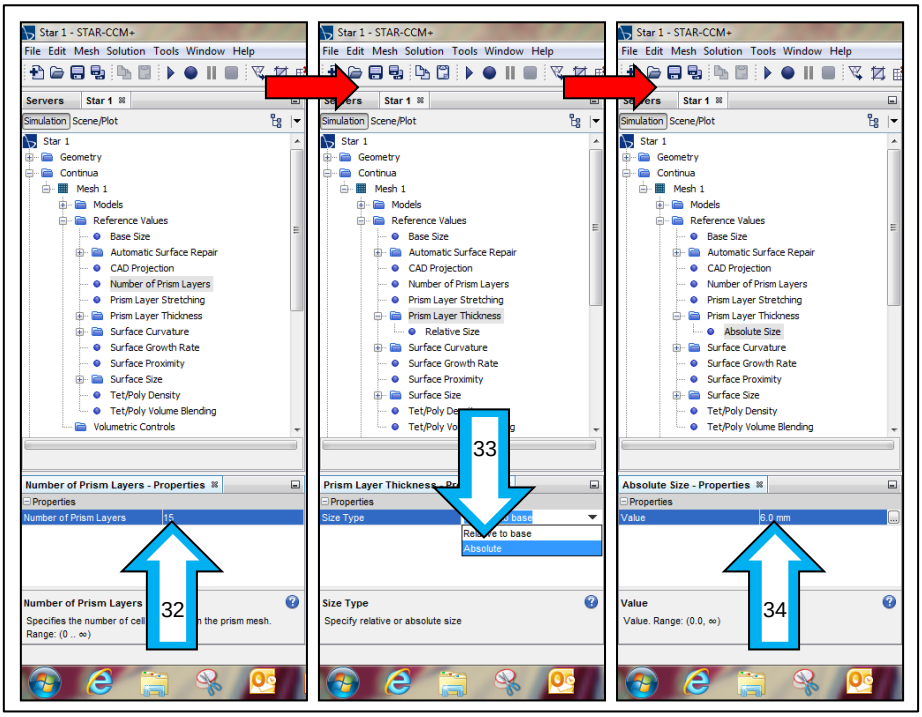

Figure 4-11: Set the mesh continuum prism layer amount and thickness

Enable the custom surface size option under the tail section boundary (“Sailplane” boundary) and change the relative minimum and target sizes to 0.1 % and 2 % respectively (Figure 4-12).

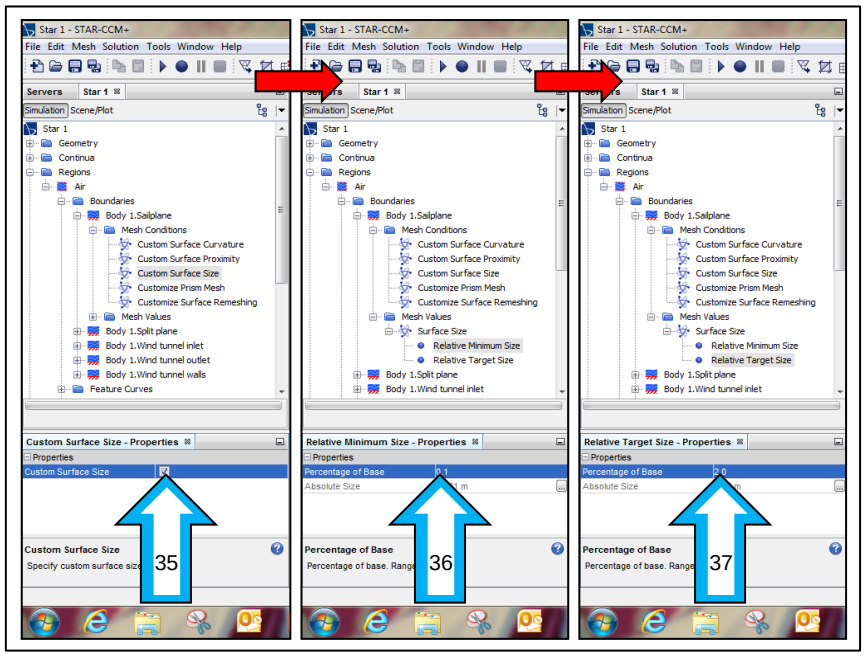

Figure 4-12: **Set the mesh continuum surface size under the tail section boundary**

Change the type of the wind tunnel inlet boundary to a velocity inlet and the wind tunnel outlet to a pressure outlet (Figure 4-13). Generate the volume mesh and wait until the software has finished; the larger and more complex the geometry created and the finer the mesh settings assigned, the longer the software will take to generate the mesh.

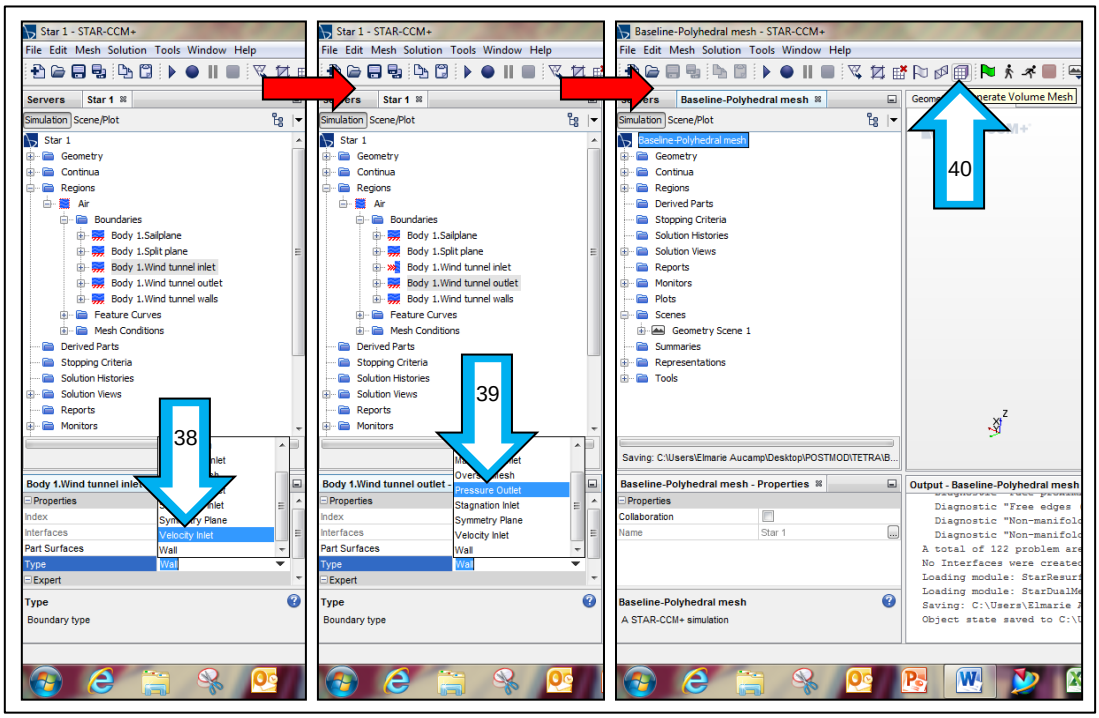

Figure 4-13: **Assign the wind tunnel inlet and outlet boundary types and generate the volume mesh**

Create a mesh scene and identify a small or fine detailed area on the tail section for evaluation (Figure 4-14). The mesh should conform to the surfaces of the tail; if the mesh is too course the surfaces become distorted and small detail is lost. The surface size of the sailplane boundary can be further reduced until the desired mesh size is reached (Figure 4-12). The volume mesh must be re-meshed as changes are made.

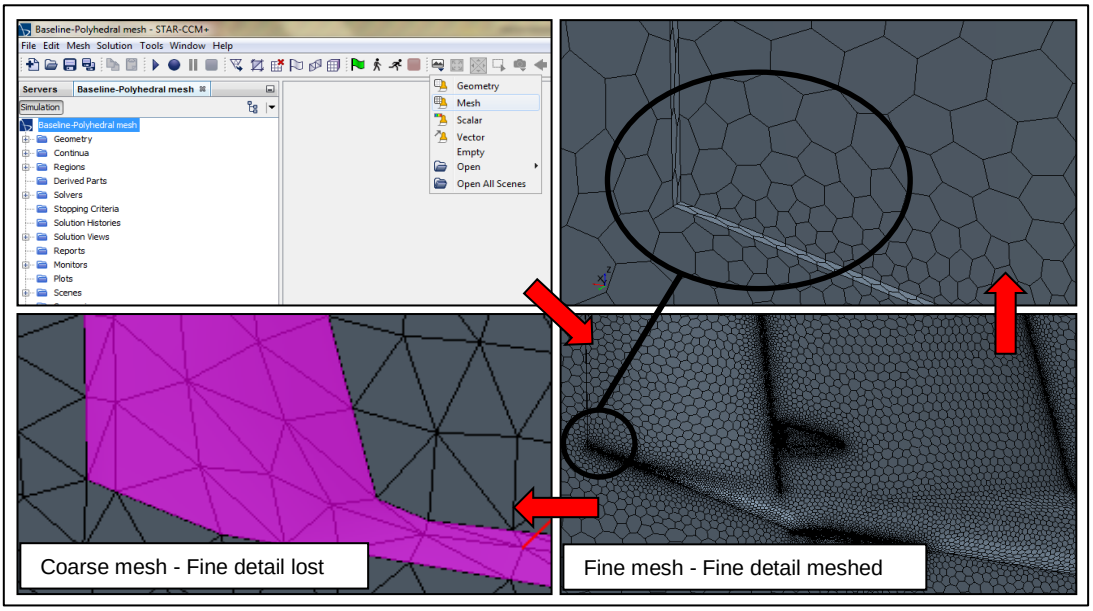

Figure 4-14: **Mesh scene created and the mesh quality evaluated**

Create a scalar field function (in this case “Gamma-ReTheta wall distance”) and set the definition as “$WallDistance>0.006?1:0” (Figure 4-15). This limits the thickness of the first boundary layer that forms over the surfaces of the tail section to 6 mm.

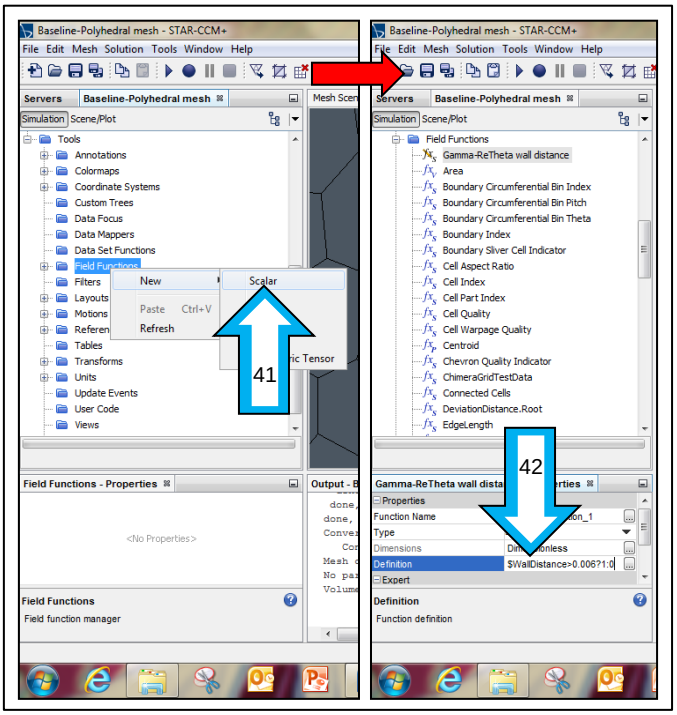

Figure 4-15: **Create a scalar field function**

The software automatically generates a physics continuum when the volume mesh is created and the following properties can be assigned (Table 4-2):

Table 4-2: Physics continuum

Category	Property
Time	Steady
Material	Gas
Flow	Segregated flow
Equation of state	Constant density
Viscous regime	Turbulent
Reynolds-averaged turbulence	K-Omega turbulence
Transition	Gamma-ReTheta transition

Note that the “Three Dimensional” property is automatically assigned before any selections are made and that additional properties are automatically added as selections are made (Figure 4-16).

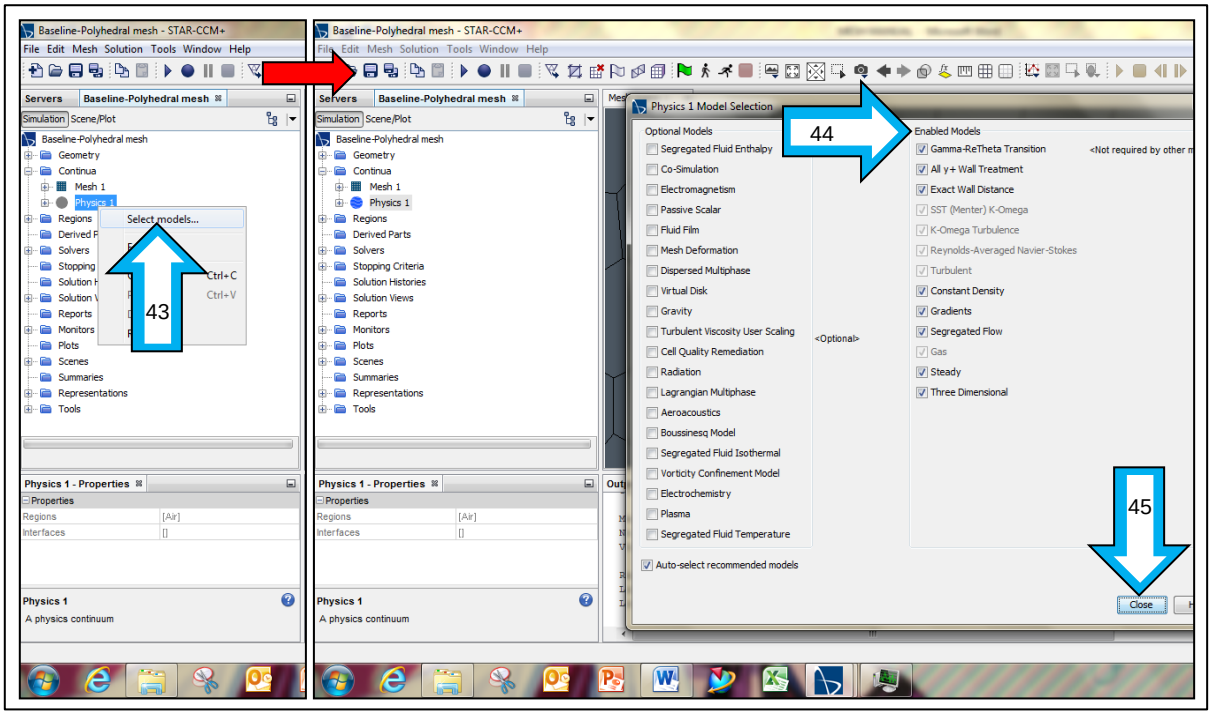

Figure 4-16: Select physics continuum properties

Assign the scalar field function created to the Gamma-ReTheta transition model (Figure 4-17).

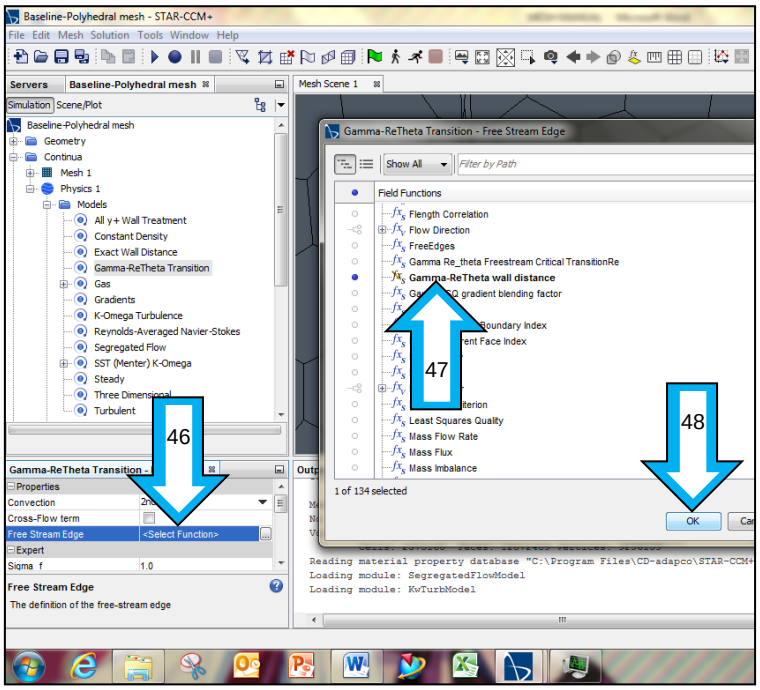

Figure 4-17: Assign the scalar field function created to the Gamma-ReTheta transition model

Disable the “Customize Prism Mesh” option for all the wind tunnel surfaces, including the split surface (Figure 4-18).

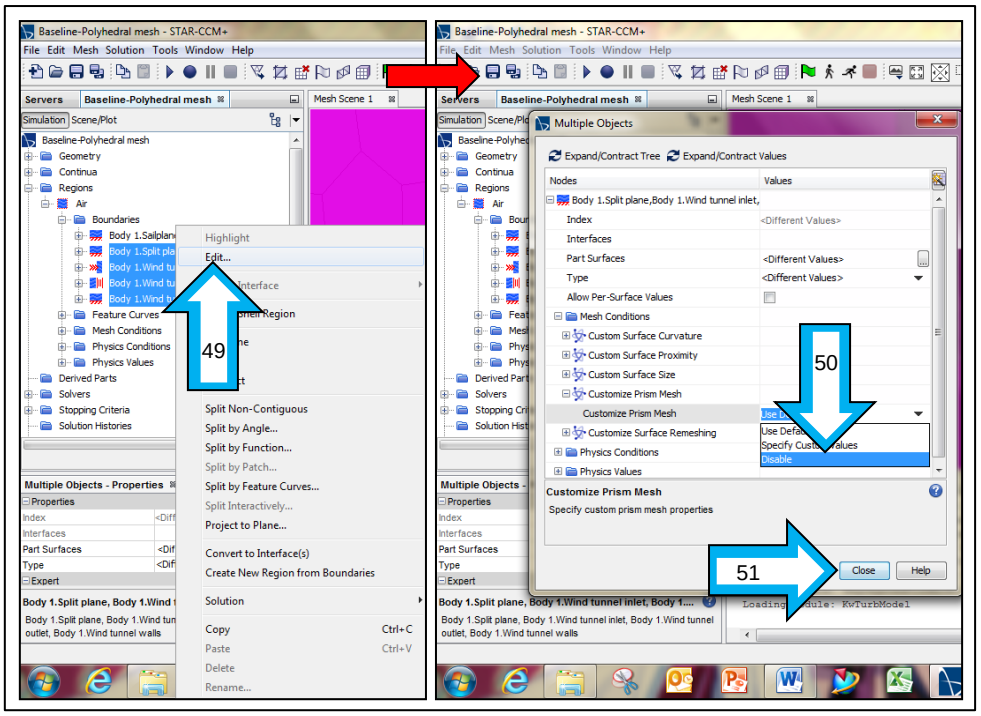

Figure 4-18: Disable the wind tunnel and split plane boundary prism mesh settings

Change the shear stress specification method of the split surface and wind tunnel outer walls to “Slip” (Figure 4-19).

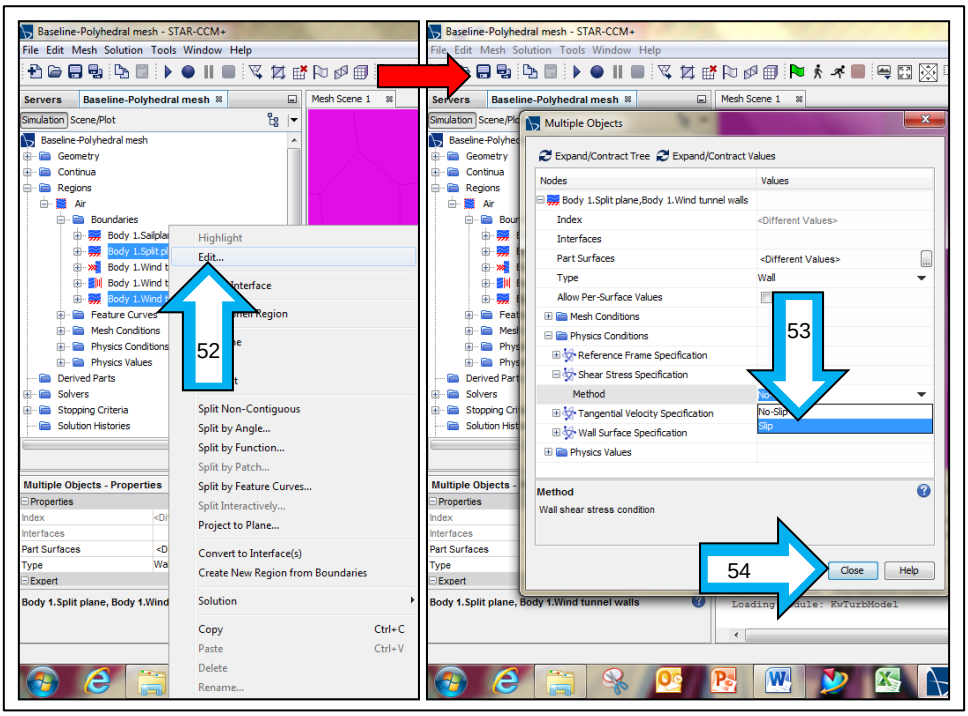

Figure 4-19: Change the wind tunnel outer wall and split plane boundary shear stress specification

Set the velocity of the airflow that the wind tunnel must generate under the wind tunnel inlet boundary (Figure 4-20) and create a report. Reports are used to record and display graphical data of variables as the program runs where, in this case, a “Force” report was created to record the drag over the surfaces of the tail section.

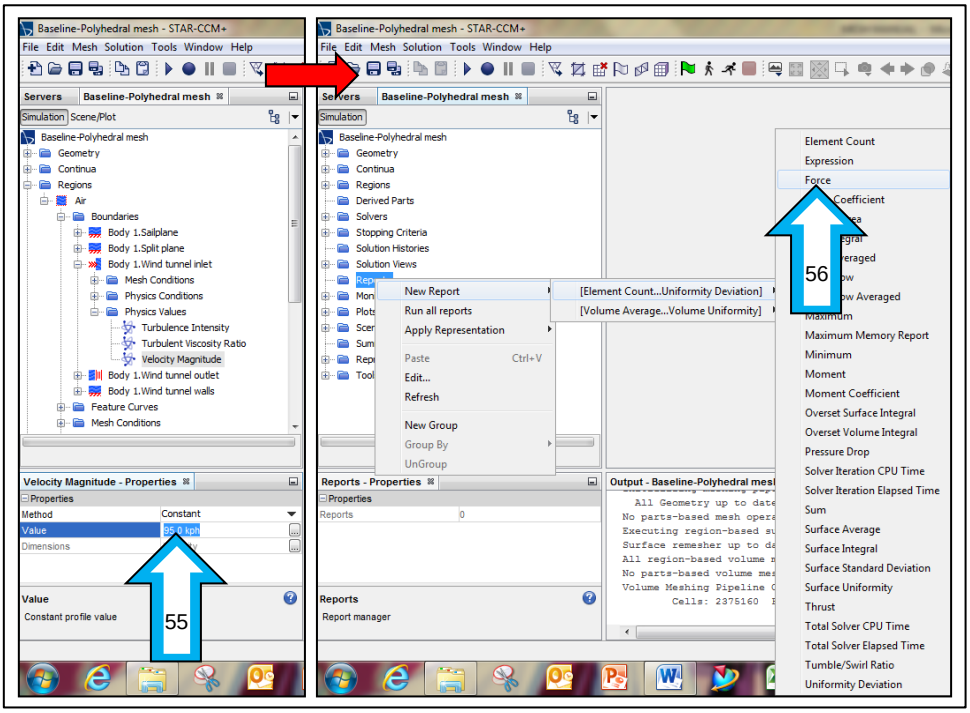

Figure 4-20: Set the velocity to be generated by the wind tunnel and create a force report

Assign the tail section boundary to the “Force” report created (Figure 4-21).

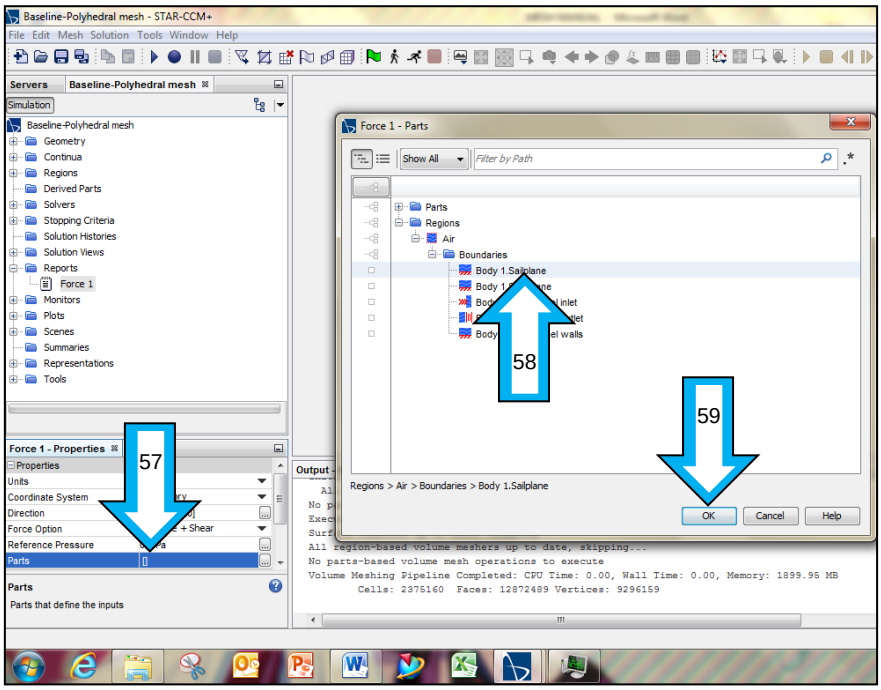

Figure 4-21: **Assign the tail section boundary to the force report**

Create a graph to display the data recorded by the “Force” report and run the program (Figure 4-22).

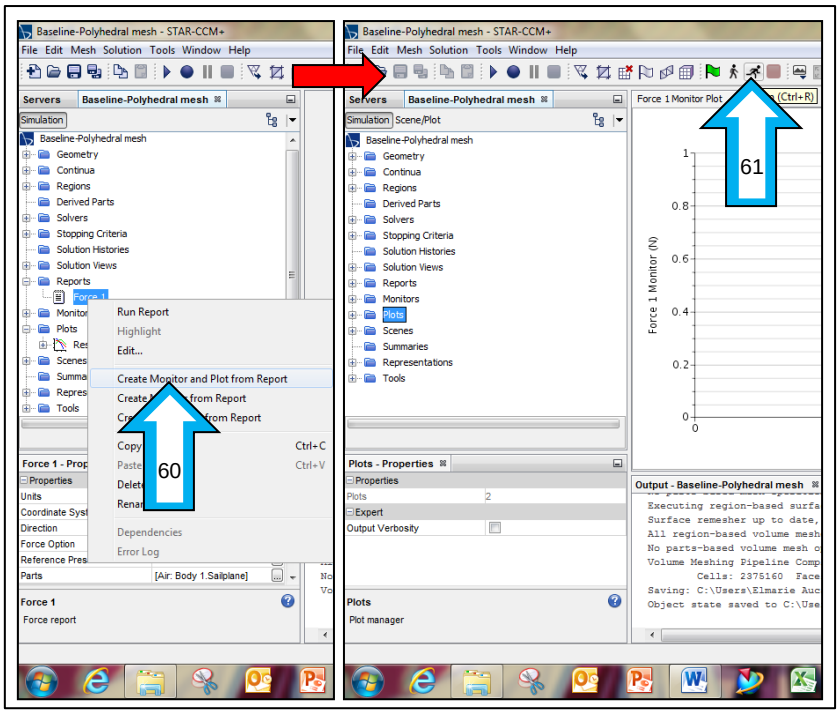

Figure 4-22: **Create a plot from the force report and run the program**

Ensure that the density of the airflow in the wind tunnel is set accordingly before running the program (Figure 4-23); if it is used to recreate data from a flight test the temperature of the air at the altitude the test was conducted is used to calculate the density.

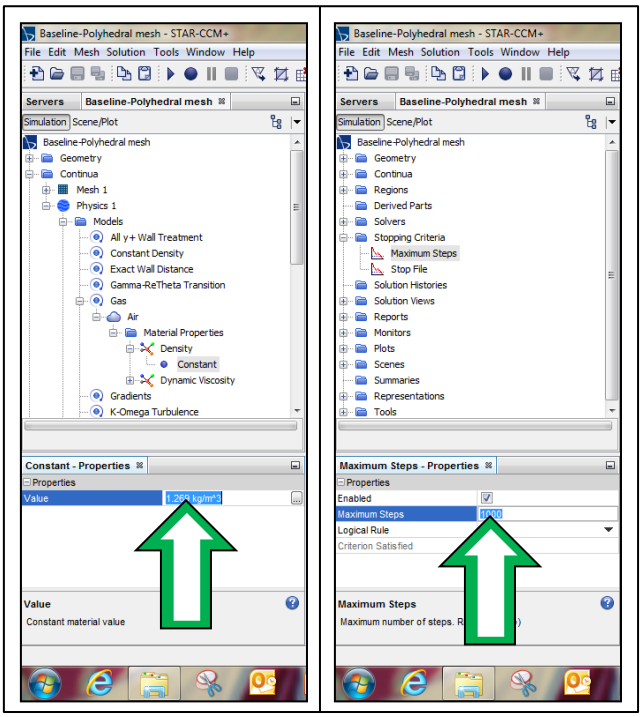

Figure 4-23: Set the density if recreating flight test data (left) and assign stopping criteria (right)

The more complex or detailed the CFD program becomes the more time or runs it will require for the variable data to converge. The program can be left to run until manually stopped or criteria can be assigned to stop the program after certain conditions have been met. The program was set to automatically stop after reaching 3000 iterations or steps.

4.3 Select a different mesh and physics continuum

The meshing continuum can be changed anytime if needed by deselecting the previous properties chosen and selecting the new properties (Figure 4-10). Note that the “Polyhedral Mesher” option is locked (parent criteria) and can only be unlocked when the sub section (child criteria) thereof, namely “Prism Layer Mesher”, is first deselected. The same applies to the physics continuum (Figure 4-16).

4.4 Simulate a different CAD model

The method described to create the geometry in the CFD software enables the freedom to change the CAD of the model simulated with a certain limitation. The original wind tunnel block imported cannot be deleted, otherwise all the surfaces and boundaries generated will be reset; a new simulation will have to be set up. However, the block can be resized and translated as needed. The program can be used to evaluate different models, such as the total energy probe moved to different areas on the tail section, all with the same base programming. The second body and subtract feature under the “Features” folder is deleted (Figure 4-24) and the same

steps are used to import and subtract the new body from the wind tunnel block (Figure 4-2 and Figure 4-3).

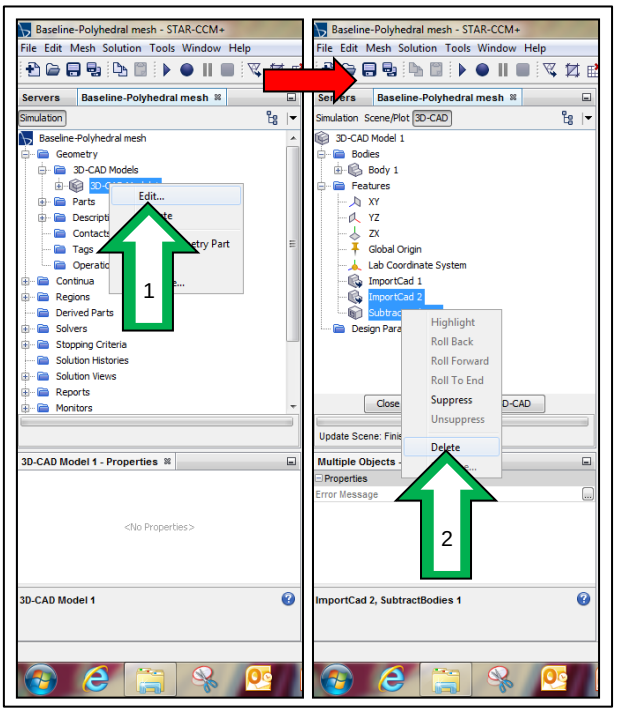

Figure 4-24: Delete the tail section body and subtract feature to change the 3D-CAD model

Update and close the modified 3D-CAD geometry, update the part created from the 3D-CAD geometry and re-mesh the volume mesh (Figure 4-25).

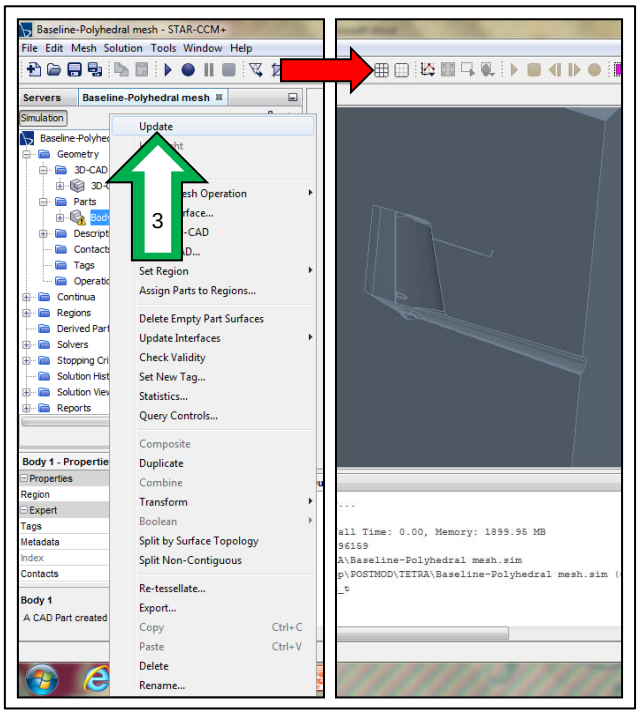

Figure 4-25: Always update the part geometry after changes are made

It is important to update the part after any modifications made, otherwise the program will continue to use the previous mesh generated.

4.5 Total energy probe variables

Variables measured by the total energy probe can be recorded by creating additional reports (Figure 4-20). Discretion is used when selecting the type of report used to record, for instance, the pressure inside the probe; there are different report types, such as “Maximum” and “Pressure”, which will record the exact same data. A derived part is created inside the total energy probe and assigned to the report created (Figure 4-21 and Figure 4-26).

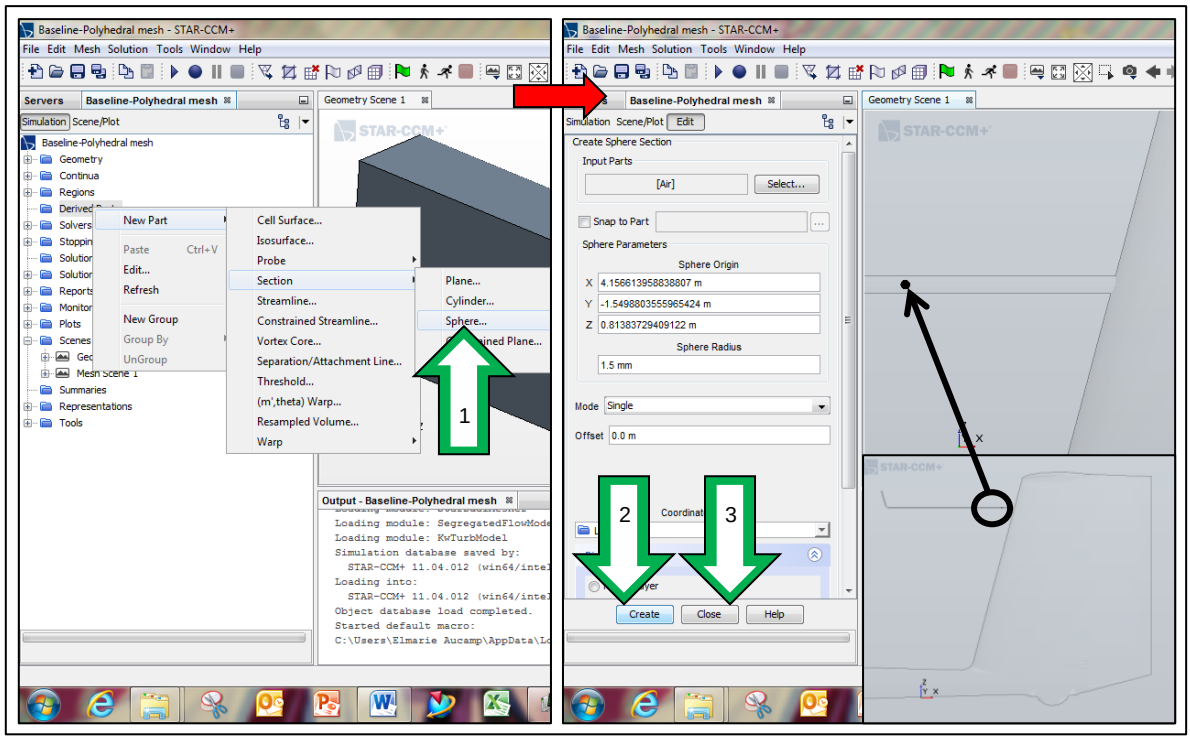

Figure 4-26: Derived part created inside the total energy probe

Ensure that the geometry scene is open when creating the derived part, as the software automatically creates the part in the current open scene.

4.6 Conclusion

The CFD program presented enables simple and flexible editing of a CAD model suspended in a wind tunnel where the same base programming is used to accurately compare different configurations or designs.

The current probe was subjected to flight tests to determine the compensation characteristics thereof during various flight manoeuvres. The flight data obtained was used to (1) determine the minimum pressure a total energy probe design may measure in straight and level flight to prevent under-compensation and (2) validate the CFD program calculations in chapter 6.

CHAPTER 5: BASELINE COMPENSATION CHARACTERISTICS ANALYSIS

The compensation capabilities of the current total energy probe was analysed to determine the characteristics thereof during various flight manoeuvres. Two variometers were fitted for the tests; an LX9000 instrument for electric compensation and an S100 instrument to represent mechanical compensation.

The LX9000 is a flight computer used as a high-end vario navigation system with a flight recorder function (lxnav, 2016a). The S100 is also a navigation system with a standalone digital variometer and flight recorder function (lxnav, 2016b). Both instruments are connected to the pitot-static probe to calculate various parameters during flight such as the current altitude and airspeed flown. The pneumatic line of the pitot-static probe is also connected to the total energy port of the LX9000, where it calculates and displays the variometer reading according to the total and static pressure measured (electric variometer). The total energy probe pneumatic line is connected to the total energy port of the S100 to represent a mechanical variometer (paragraph 2.3).

The S100 is also an electric variometer, where it displays calculation outputs based on the pressure measured by the probes. However, connecting the total energy probe to the instrument forces it to use the dynamic pressure measured by the probe without having to calculate it using the total and static pressure. The S100 then applies a mathematical filter to recreate the smooth and delayed indicator display of a mechanical variometer.

5.1 Current total energy probe

The current total energy probe, as designed by the manufacturer, over-compensated during flight testing when the probe was initially installed on the JS-1C during production. The probe was modified to reduce the pressure drop by extending the end with 4 mm, and the compensation capabilities thereof was verified through extensive flight testing. The following assumptions were made:

1. If the installation of the probe was not according to the specifications of the manufacturer and caused the probe to over-compensate, then the modification to the probe would cause it to compensate, as designed, with a C_P of -1.
2. If the probe was installed according to the specifications of the manufacturer and the probe, as designed, measured a C_P of -1, then the modification to the probe would cause it to under-compensate.

The LX9000 instrument, if set to compensate 100 %, would use appropriate algorithms to calculate the total energy gained or lost according to the pressures measured by the pitot-static probe. Therefore, it should give an average C_P of -1 during straight and level flight, which can verify the assumptions made when compared to the S100 instrument.

5.2 Straight and level flight

The indicated airspeed (IAS) of the LX9000 was used as reference to fly at various goal speeds throughout the tests (Table 5-1). The calibrated airspeed (CAS) was calculated using instrument correction (obtained through instrument calibration) and position correction (obtained through the certification process).

Table 5-1: Calibrated airspeed calculated for the LX9000 and S100 instruments

		LX9000			S100		
Goal speed	Position correction	Instrument correction	IAS	CAS	Instrument correction	IAS	CAS
km/h	km/h	km/h	km/h	km/h	km/h	km/h	km/h
100	-1.7	1.5	95.6	95.4	-2.7	87.0	82.6
120	-2.1	2.6	117.2	117.7	-4.5	110.3	103.7
150	-0.6	2.0	154.5	155.9	-4.5	149.4	144.3
170	-0.7	2.6	173.4	175.3	-4.6	168.9	163.6
200	-1.6	3.5	202.1	204.0	-3.1	198.3	193.6

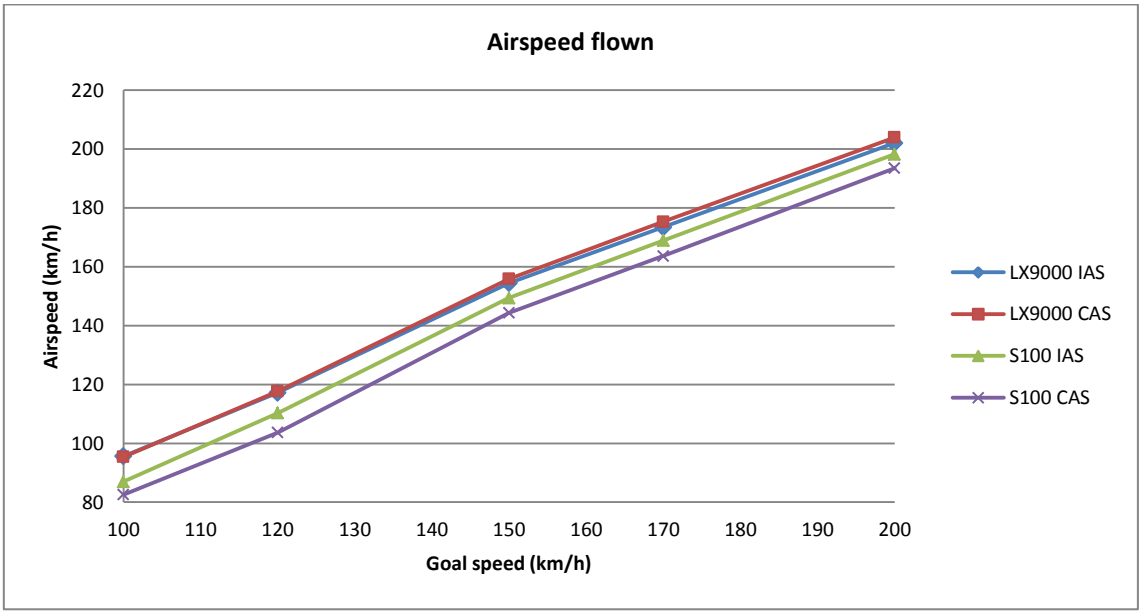

Figure 5-1: Indicated and calibrated airspeeds of the LX9000 and S100 instruments at various goal speeds

The total energy probe under-compensated and caused the indicated airspeed to under-read, but improved as the airspeed increased (Figure 5-1).

Table 5-2: Pressure coefficient measured by the LX9000 and S100 instruments

Theoretical model		LX9000		S100	
CAS	Pressure drop	Pressure drop	Cp	Pressure drop	Cp
km/h	Pa	Pa	-	Pa	-
95	-446	-446	-1.0	-334	-0.8
118	-679	-679	-1.0	-526	-0.8
156	-1189	-1189	-1.0	-1020	-0.9
175	-1505	-1505	-1.0	-1311	-0.9
204	-2037	-2037	-1.0	-1834	-0.9

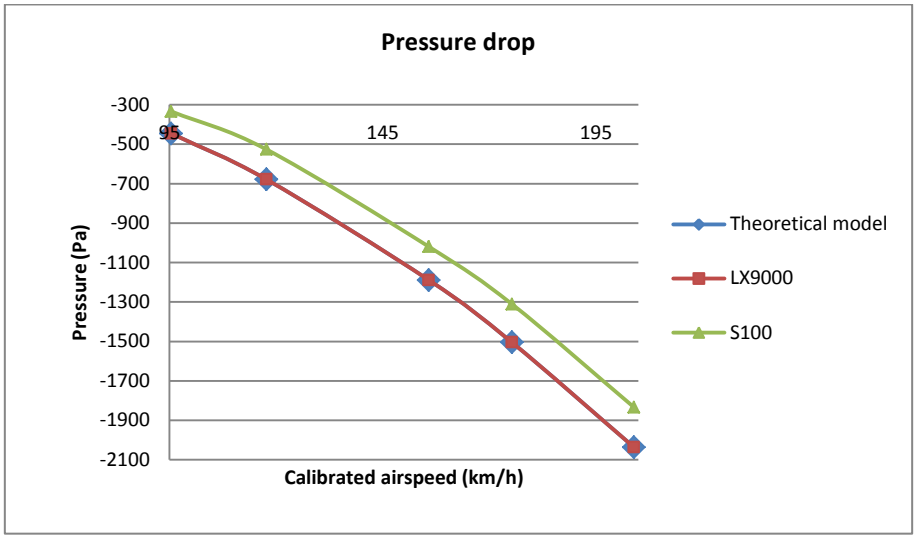

Figure 5-2: Pressure drop measured by the LX9000 and S100 instruments

The average pressure coefficient measured by the total energy probe was -0.83 (Table 5-2). This correlates with the second assumption made in paragraph 5.1, where the modified probe under-compensates on purpose, as determined through the extensive flight tests conducted on the JS-1C (Figure 5-2). This contradicts the theory of a total energy probe compensating efficiently when it measures a C_P of -1.

The current total energy probe and pitot-static probe was analysed during pitch manoeuvres to determine the compensation characteristics thereof according to the movements of the variometer indicators (LX9000 and S100).

5.3 Pitch manoeuvres

The flight test methods described in paragraph 2.7 were used to evaluate the compensation characteristics of the probes during pitch.

5.3.1 Total energy probe

The following observations were made according to the S100 instrument readings:

1. The variometer indicated the minimum sink rate of the sailplane of approximately 0.7 m/s when flying at the minimum sink speed.
2. An average reading of +0.2 m/s was indicated when the control stick was pushed forward to position the sailplane into a nose down attitude to initiate a dive. The slight deviation from 0 m/s is due to the probe positioned aft of the centre of gravity.
3. The average variometer reading during the dive had three characteristics:
    - A gradual increase in sink after entering the dive up to 3 m/s at 150 km/h.
    - A gradual increase in sink to 5m/s up to 220 km/h.
    - The indicator reached the maximum deflection position after 230 km/h.

    The sink rate was calculated during straight and level flight to compare to that indicated on the variometer. Two points in the flight data were chosen where the airspeed flown remained constant. The altitude lost between the chosen points was divided by the time lapse between them to calculate the sink rate at each designated speed (Table 5-3). The sink rate measured during straight and level flight increased slightly as the airspeed increased compared to that calculated. The probe measured a sink rate nearly twice than that measured during straight and level flight during the dive, but improved as the speed increased (Figure 5-3). At 95 km/h the sink rate measured was affected by the reading increase caused when the control stick was pushed forward to initiate the dive and at 204 km/h the probe over-compensated by 10 %
4. The control stick was pulled back to pull the sailplane out of the dive before reaching V_{NE}, which caused the variometer to briefly measure a greater sink rate. The variometer showed a sudden increase (indicator moving from the negative to the positive direction) after entering the climb and then gradually slowed to 0 m/s with the indicator overshooting slightly, indicating a maximum average reading of +1 m/s.

Table 5-3: Sink rate calculated for and measured by the S100 instrument

CAS	Calculated sink rate in straight and level flight	Measured sink rate in straight and level flight	Measured sink rate in the dive
km/h	m/s	m/s	m/s
95	-0.6	-0.6	+0.1
118	-0.7	-0.8	-1.6
156	-1.1	-1.4	-3.0
175	-1.6	-1.8	-3.4
204	-2.5	-3.2	-3.5

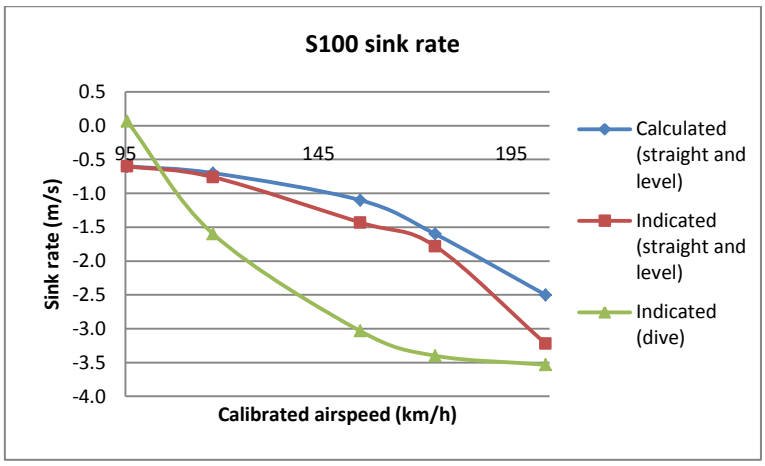

Figure 5-3: Sink rate calculated for and measured by the S100 instrument

The average readings in (3) and (4) indicate that the total energy probe does not compensate adequately during climb and dive manoeuvres. The variometer is a lagging instrument, where it needs time to catch up with the increasing (3) and decreasing (4) speed and would, therefore, under-read temporarily until it caught up when the speed no longer changed. The sudden increase in (4) should have been gradual.

5.3.2 Pitot-static probe

The following observations were made according to the LX9000 instrument readings:

1. The variometer indicated the minimum sink rate of the sailplane of approximately 0.7 m/s when flying at the minimum sink speed.
2. An average reading of +0.1 m/s was indicated when the control stick was pushed forward to position the sailplane into a nose down attitude to initiate a dive. The slight deviation from 0 m/s is due to the probe positioned aft of the centre of gravity.
3. The average variometer reading during the dive had two characteristics:
    - A gradual increase in sink after entering the dive up to 1 m/s at 150 km/h.
    - A gradual increase in sink up to the maximum deflection position after 220 km/h.

    The sink rate measured during straight and level flight increased slightly as the airspeed increased compared to the calculated sink rate (Table 5-4). The electric variometer under-compensated in the dive compared to that measured during straight and level flight (Figure 5-4).
4. The control stick was pulled back to pull the sailplane out of the dive before reaching V_{NE}, which caused the variometer to briefly measure a greater sink rate. The variometer showed a gradual increase (indicator moving from the negative to the positive direction) after entering the climb up to 0 m/s without overshooting to the positive direction.

Table 5-4: Sink rate calculated for and measured by the LX9000 instrument

CAS	Calculated sink rate in straight and level flight	Measured sink rate in straight and level flight	Measured sink rate in the dive
km/h	m/s	m/s	m/s
95	-0.5	-0.6	-0.2
118	-0.6	-0.8	-0.4
156	-1.3	-1.5	-0.9
175	-1.4	-1.8	-0.9
204	-2.8	-3.1	-0.8

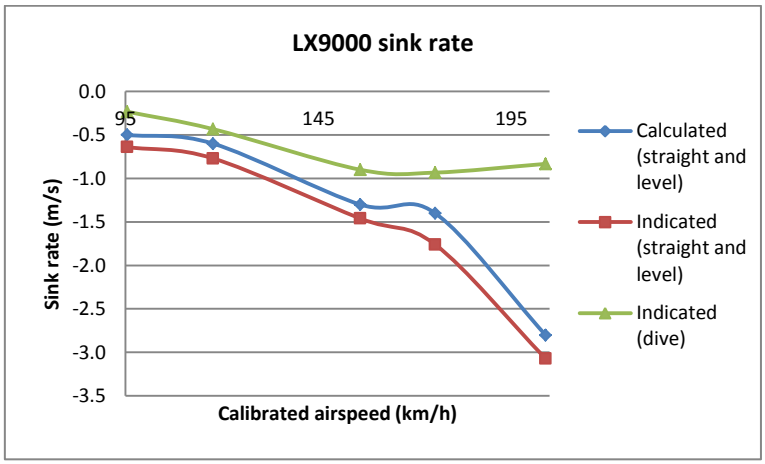

Figure 5-4: Sink rate calculated for and measured by the LX9000 instrument

The average readings in (3) and (4) indicate that the electric variometer compensates adequately during climb and dive manoeuvres. The variometer under-reads as it tries to catch up with the change in airspeed, as expected.

The total energy and pitot-static probes were analysed during sideslip manoeuvres to determine the compensation characteristics thereof according to the movements of the variometer indicators.

5.4 Sideslip manoeuvres

The flight test methods described in paragraph 2.7 were used to evaluate the compensation characteristics of the probes during sideslip.

5.4.1 Total energy probe

The following observations were made according to the S100 instrument readings:

1. The variometer reading indicated a strong increase in sink when the sideslip was induced.
2. The release of the rudder to perform the recovery caused a gradual transition back to the minimum sink rate of the sailplane.

3. The variometer did not indicate less than the minimum sink rate after each sideslip recovery.

5.4.2 Pitot-static probe

The following observations were made according to the LX9000 instrument readings:

1. The variometer reading indicated a strong increase in sink when the sideslip was induced.
2. The release of the rudder to perform the recovery caused a gradual transition to 0 m/s.
3. The variometer indicated less than the actual sink rate after each sideslip recovery, but gradually stabilised back to the minimum sink rate the longer the recovery was maintained.

5.4.3 Discussion

The total energy probe is less sensitive to sideslip than the pitot-static probe and recovers adequately after sideslip is induced.

5.5 Discussion

The actual pressure coefficient measured by various total energy probes to compensate efficiently during manoeuvres may vary from the theoretical Cp value of -1 due to their design (paragraph 5.2). The total energy probe design should, however, perform the same as or better than the current probe without exceeding the theoretical model. The performance observed during flight testing showed that the current probe did not compensate efficiently during pitch manoeuvres, but performed adequately during sideslip manoeuvres.

5.6 Conclusion

The compensation characteristics of the current total energy probe installed on the JS-1C was established through flight tests.

The minimum pressure a total energy probe configuration or design may measure in straight and level flight was identified using the flight test data obtained. The probe must measure a pressure coefficient greater than -0.83 (current total energy probe) to prevent under-compensation, but no greater than -1.00 (theoretical model) to prevent over-compensation in straight and level flight. The probe should also try to include the benefits of an electric variometer to reduce pitch sensitivity, while maintaining good compensation during sideslip.

The CFD program was used to calculate the pressure measured by the current total energy probe during different flight manoeuvres and compared to the flight test data for validation.

CHAPTER 6: COMPUTATIONAL FLUID DYNAMICS ANALYSIS AND VALIDATION

The CFD program created in chapter 4 was used to calculate the theoretical pressure measured by the current total energy probe during different flight manoeuvres at the same flight conditions as that of the flight tests. The data measured in-flight and that calculated in CFD was compared to validate the ability of the CFD program to recreate flight test data.

6.1 Dynamic pressure validation

The CFD program has different meshing models that can be used to calculate the pressure measured by the current total energy probe. The current probe was simulated using each meshing model and compared to the flight test data to determine which mesh would recreate the flight test data more accurately.

6.1.1 Meshing models

The pressure measured by the current total energy probe was calculated using different meshing models and compared to that measured in-flight (Figure 6-1 and Table 6-1). The pressure calculated using the polyhedral and tetrahedral mesh was nearly the same. Both meshing models conformed closely to the theoretical model at lower airspeeds, while conforming to the current total energy probe at higher airspeeds.

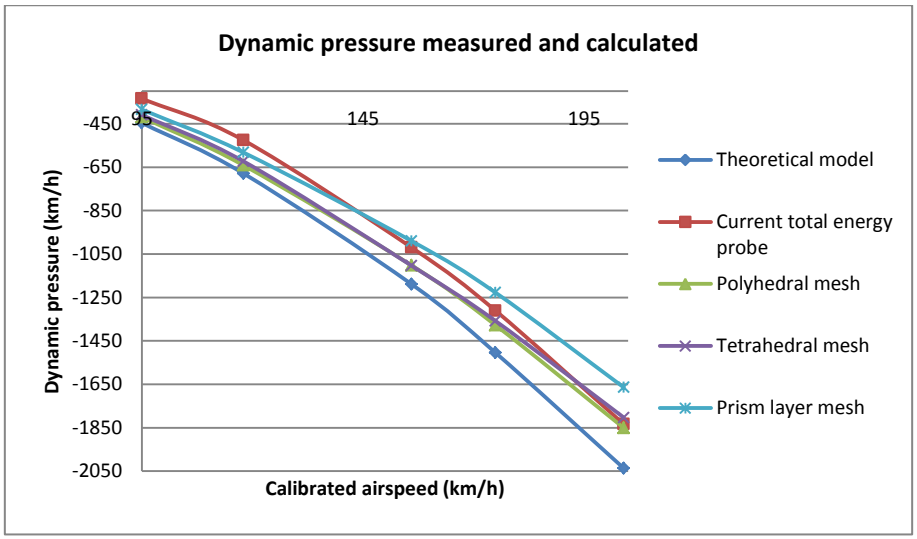

Figure 6-1 **Flight test data compared to the CFD calculations**

Table 6-1: Flight test data compared to the CFD calculations

Dynamic pressure (Pa)					
Data obtained	CAS				
	95 km/h	118 km/h	156 km/h	175 km/h	204 km/h
Theoretical model	-446	-679	-1189	-1505	-2037
Flight test	-334	-526	-1020	-1311	-1834
CFD: Polyhedral mesh	-419	-641	-1102	-1378	-1851
CFD: Tetrahedral mesh	-409	-623	-1104	-1359	-1803
CFD: Prism layer mesh	-384	-582	-990	-1228	-1664

The CFD program, assigned with a polyhedral mesh, was used to calculate the pressure measured by the current total energy probe with and without the modification described in paragraph 5.1.

6.1.2 Current total energy probe

The current total energy probe, with and without the modification described in paragraph 5.1, was analysed using the CFD program during straight and level flight (Figure 6-2). The following assumption was made based on the data obtained in paragraph 5.2: If the probe was installed according to the specifications of the manufacturer and the probe, as designed, measured a C_P of -1, then the modification to the probe would cause it to under-compensate with a C_P of -0.86.

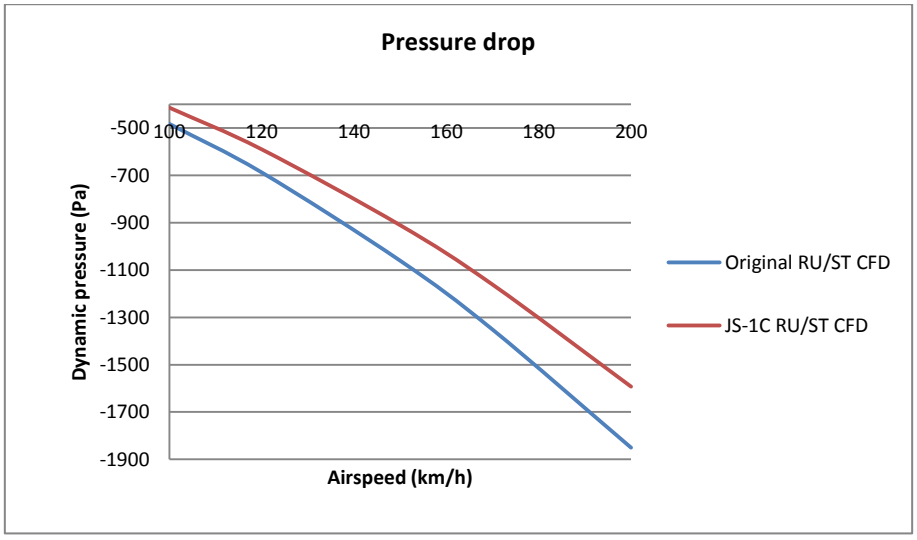

Figure 6-2: Pressure drop calculated for the original and modified total energy probes

The average pressure coefficient measured in-flight (-0.83) and that calculated by the CFD program (-0.86) was compared and showed that the program gave an error of around 3 %. The CFD also correlates with the second assumption made in paragraph 5.1, where the modified probe under-compensates on purpose (Figure 5-2).

6.1.3 Discussion

The tetrahedral mesh calculated a pressure closer to that measured by the current total energy probe. However, the polyhedral mesh created a much more stable pressure curve and was therefore chosen as the preferred meshing model to recreate flight test data with an error of around 3 % (Figure 6-3).

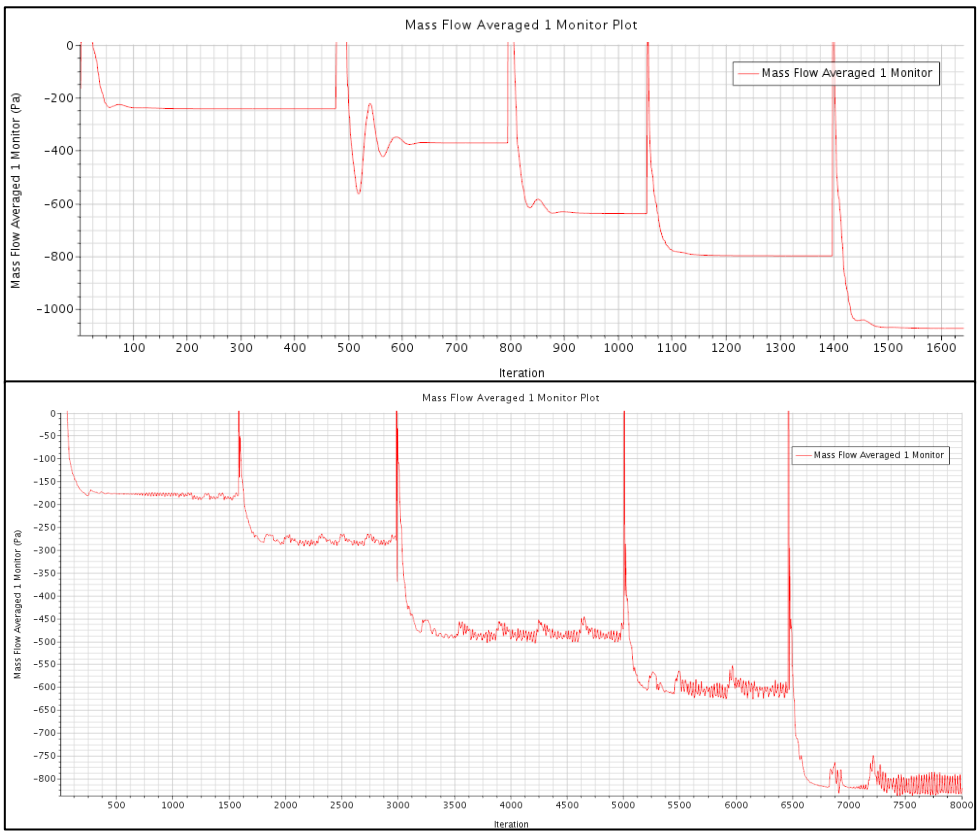

Figure 6-3: Polyhedral (top) and tetrahedral (bottom) mesh pressure curves

The current probe was analysed using the CFD program during pitch manoeuvres, where the pressure drop calculated during the manoeuvres should be the same as or close to the pressure drop calculated during straight and level flight. The smaller the difference calculated, the less sensitive the probe; the greater the difference calculated, the more sensitive the probe.

6.2 Pitch manoeuvres

A CFD model of the current probe was created where the model was repositioned to simulate a pitch of 10° nose up (climb) and nose down (dive) attitude (Figure 6-4 and Table 6-2).

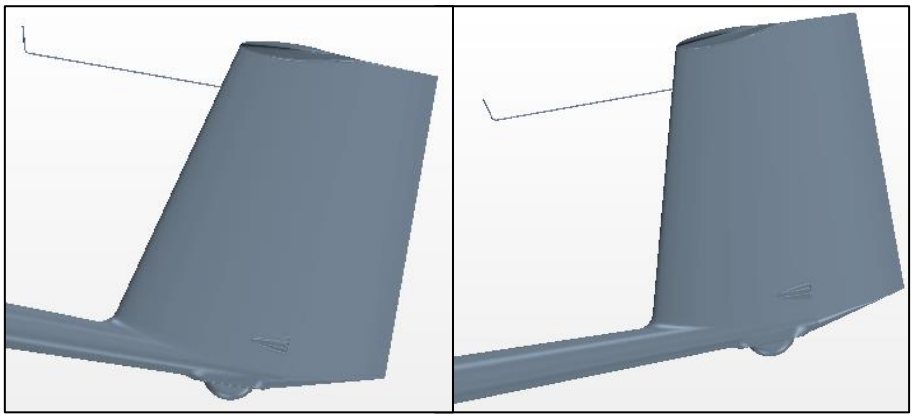

Figure 6-4: **CFD model repositioned to simulate a 10° pitch nose up (left) and nose down (right) attitude**

Table 6-2: **Pressure drop calculated using CFD for the current total energy probe during pitch manoeuvres**

CAS	Straight and level	Pitch 10° down		Pitch 10° up	
km/h	Pressure drop (Pa)	Pressure drop (Pa)	Difference (%)	Pressure drop (Pa)	Difference (%)
95	-387	-374	-3	-385	-1
118	-591	-572	-3	-582	-2
156	-1016	-986	-3	-978	-4
175	-1270	-1237	-3	-1214	-4
204	-1710	-1667	-3	-1641	-4

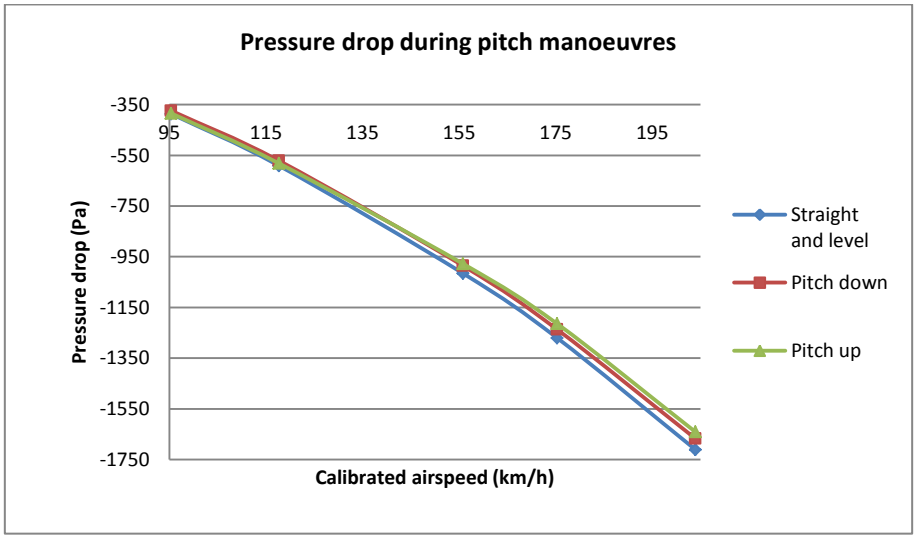

Figure 6-5: **Pressure drop calculated using CFD for the current total energy probe during pitch manoeuvres**

An average pressure drop difference of 3 % was calculated for both pitch manoeuvres (Figure 6-5) when compared to straight and level flight.

The current probe was analysed using CFD during sideslip manoeuvres. As with the pitch manoeuvres the pressure drop calculated should be the same as or close to that calculated during straight and level flight.

6.3 Sideslip manoeuvres

The CFD model of the current probe used to calculate the pressure drop during pitch manoeuvres was modified, where the model was repositioned to simulate a sideslip of 10° (Figure 6-6 and Table 6-3).

Figure 6-6: **Pitch CFD model modified to simulate a 10° sideslip**

Table 6-3: **Pressure drop calculated using CFD for the current total energy probe during a sideslip manoeuvre**

CAS	Straight and level	Sideslip 10°	
km/h	Pressure drop (Pa)	Pressure drop (Pa)	Difference (%)
95	-387	-437	13
118	-591	-671	14
156	-1016	-1174	16
175	-1270	-1456	15
204	-1710	-1970	15

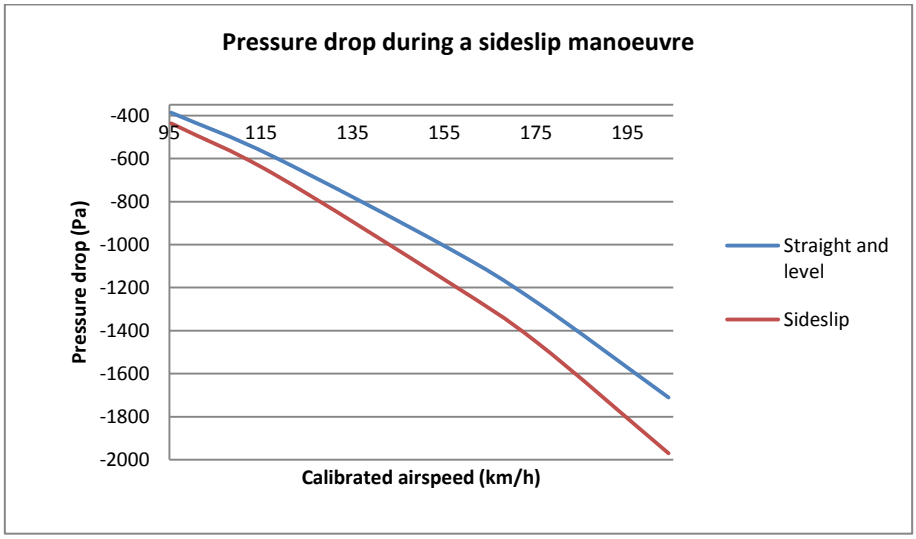

Figure 6-7: **Pressure drop calculated using CFD for the current total energy probe during a sideslip manoeuvre**

An average pressure drop difference of 14 % was calculated for the sideslip manoeuvre when compared to straight and level flight (Figure 6-7).

6.4 Discussion

The CFD calculations show that the current probe should be less sensitive to pitch manoeuvres and more susceptible to sideslip manoeuvres. This is the opposite of that observed during the flight tests. Since the CFD program cannot replicate behaviour while in the process of conducting or recovering from a manoeuvre, only the manoeuvre when maintained can be evaluated. However, the behaviour of the variometer indicator during different flight manoeuvres, as stated in paragraph 2.7, is more important than the exact value indicated and the measured data only becomes relevant after each manoeuvre is completed (Brözel, explained by Knauff & Nadler, 2002). In other words, only after the recovery of each manoeuvre does one look at the data. Attention is given to whether the variometer indicates the same data as that shown before the manoeuvre was initiated, or whether the variometer fluctuates and how long it takes before reaching the same data as that shown before the manoeuvre was initiated.

Theoretically, if a manoeuvre is maintained, a perfect total energy probe should measure the same pressure as that measured during straight and level flight. Therefore, although CFD cannot be used to replicate variometer behaviour, it can be used to look at the data obtained when a manoeuvre is maintained without initiation or recovery.

6.5 Conclusion

The ability of the CFD program to replicate flight test data was validated. The polyhedral mesh was chosen as the preferred meshing model for flight test data replication, as it calculated a pressure closer to that measured by the current total energy probe with a stable pressure curve.

The CFD program can be used to calculate the pressure measured by total energy probe configurations or designs in straight and level flight within a 3 % error margin, as well as the theoretical pressure difference measured when pitch and sideslip manoeuvres are maintained. It cannot, however, be used to recreate or evaluate the behaviour of designs during manoeuvre initiation and recovery.

The theoretical drag force of a simple aerofoil was calculated and compared to the CFD program created in chapter 4 for validation. An ideal JS-1C model without a total energy probe was then created and compared to the current total energy probe to calculate the theoretical drag the probe induced on the surfaces of the JS-1C fin.

CHAPTER 7: BASELINE DRAG ANALYSIS

The ability of the CFD program created in chapter 4 to calculate the theoretical drag force of the current total energy probe must be verified. A simple aerofoil was created and the theoretical drag thereof calculated in CFD. An ideal JS-1C model without a total energy probe was then created and compared to the current total energy probe model to determine the theoretical drag the probe induced over the surfaces of the JS-1C fin.

7.1 Drag force validation

There is no data available regarding the actual drag force that is exerted on the JS-1C sailplane. A theoretical drag force was calculated for a simple aerofoil and compared to the CFD program for validation.

7.1.1 Theoretical drag

The theoretical drag force over the cross-section of the fin where the total energy probe is positioned was calculated using variables derived from the flight test data (Table 7-1).

Table 7-1: Variables derived from the flight test data

Property	Symbol	Value	Unit
Density	ρ	1.269	kg/m^3
Airspeed	V	94	km/h
Dynamic viscosity	μ	1.86x10-5	Pa*s
Chord length	D	0.776	m
Frontal area	S	8.999	m^2

The airflow over the aerofoil is assumed either fully laminar or turbulent and the drag force over the full chord length was calculated.

$$P_{dynamic} = \frac{1}{2} * \rho * V^2 = \frac{1}{2} * 1.269 * \left(\frac{95}{3.6667}\right)^2 = 441.849\ kg/m * s^2$$

$$Re_{total} = \frac{\rho * V * D}{\mu} = \frac{1.269 * \left(\frac{94}{3.6667}\right) * 0.776}{1.86 * 10^{-5}} = 1\ 401\ 627$$

$$C_{D\ laminar\ total} = 1.328 * Re_{total}^{-\frac{1}{2}} = 1.328 * 1\ 401\ 627^{-\frac{1}{2}} = 0.00112$$

$$C_{D\ turbulent\ total} = 0.455 * (\log_{10} Re_{total})^{-2.58} = 0.455 * (\log_{10} 1\ 401\ 627)^{-2.58} = 0.00420$$

$$D_{laminar\ total} = P_{dynamic} * S * C_{D\ laminar\ total} = 441.849 * 8.999 * 0.00112 = 4.46\ N$$

$$D_{\text{turbulant total}} = P_{\text{dynamic}} * S * C_{D\ \text{turbulant total}} = 441.849 * 8.999 * 0.00420 = 16.70\ \text{N}$$

Although the polyhedral mesh can recreate the flight test data within a 3 % error margin (paragraph 6.5), a different mesh may be required to more accurately recreate the drag.

7.1.2 Meshing models

XFOIL, which is a numerical panel method used to analyse two dimensional aerofoils subjected to various flow conditions, was compared to the theoretical and CFD drag calculated (Edi, et al., 2008). The drag coefficient calculated in XFOIL suggested that it assumed that turbulent airflow occurred over the full chord length (Table 7-2).

Table 7-2: Total drag calculated and compared to XFOIL and CFD

Data obtained	Pressure coefficient	Drag	Difference
	-	N	%
Theoretical model	0.0042	16.70	0.0
XFOIL	0.0047	17.91	7.2
CFD: Polyhedral mesh	0.0058	22.28	33.4
CFD: Tetrahedral mesh	0.0048	18.20	9.0
CFD: Prism layer mesh	0.0087	33.51	100.6

As in paragraph 6.1, the prism layer mesh does not use the same base programming as the other meshing models and calculated an error of 100 %. XFOIL recreated the calculated drag force with a 7 % error, while the tetrahedral mesh recreated the calculated drag force more closely than the other meshing models with a 9 % error.

The tail section of the JS-1C was simulated using different meshing models to determine how CFD would calculate the drag force of a more complex geometry (Table 7-3 and Figure 7-1).

Table 7-3: Drag calculated using different meshing models for the JS-1C

Meshing model	CAS				
	95 km/h	118 km/h	156 km/h	175 km/h	204 km/h
Total drag (N)					
Polyhedral	4.66	6.97	11.76	14.73	19.94
Tetrahedral	5.00	7.45	12.61	15.67	21.15
Prism layer	7.29	10.94	18.46	22.89	30.52
Difference (%)					
Polyhedral	0.0	0.0	0.0	0.0	0.0
Tetrahedral	7.2	7.0	7.2	6.4	6.1
Prism layer	56.5	56.9	56.9	55.4	53.1

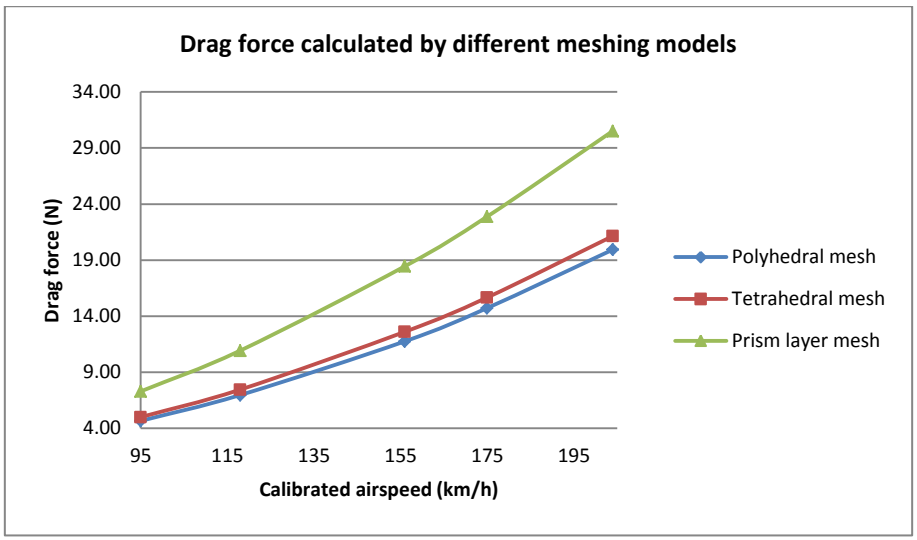

Figure 7-1: **Drag calculated using different meshing models for the JS-1C tail section**

The polyhedral mesh calculated the lowest drag force and the difference between the polyhedral and tetrahedral mesh has significantly decreased compared to that calculated in Table 7-2 (decrease from 18 % difference to 7 % difference). The prism layer mesh calculated the highest drag force as expected.

7.1.3 Discussion

The drag force calculated by the different CFD meshing models for a simple aerofoil does not correspond with that calculated for a complex geometry. The drag curve of each mesh remained relatively constant at different airspeeds and none of the curves crossed one another.

The following assumption was made: The meshing model required for accurate drag recreation is unknown and each mesh will calculate a different drag force. However, as long as the same CFD program (with the same meshing model assigned) is used to evaluate different total energy probe configurations and designs, the CFD should be able to reflect the drag behaviour of the different configurations and designs. In other words, it can determine which design or configuration induces the least or most drag compared to one another, but discretion is used when determining exactly with how much drag force they differentiate from one another.

Therefore, since the polyhedral mesh was chosen to recreate flight test data (paragraph 6.5), it was chosen to calculate the drag force induced by different total energy probe configurations and designs.

The ability of the CFD program to recreate external airflow was validated using an oil test conducted on the JS-1C.

7.2 External airflow validation

The CFD was compared to a photo taken of an oil test conducted on the JS-1C vertical tail fin during the creation of the company RFC document (paragraph 2.6) (Figure 7-2).

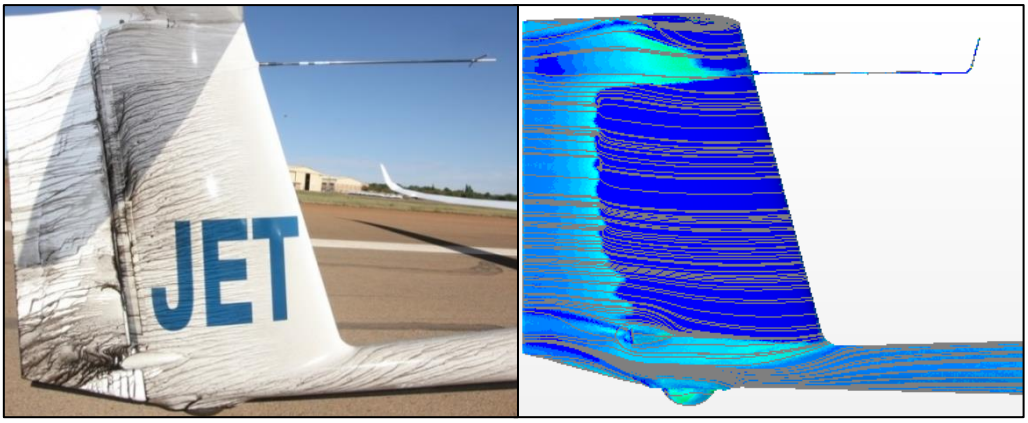

Figure 7-2: JS-1C oil test (left) compared to CFD (right) (JS, 2014)

The darker area on the CFD model indicates the laminar boundary layer and the lighter area the turbulent boundary layer. Since the probe is installed in an area least affected by the pressure over the wings and fuselage, the simulation closely replicates the oil test in the area of the probe. The simulation differentiates slightly at the bottom half of the fin where the pressure over the wings and fuselage would affect the airflow over the skin.

The transition point of the oil test occurs where the zigzag tape along the trailing edge of the fin trips the laminar boundary to turbulent to minimize the formation of air bubbles that increase the drag over the surface of the fin. The detail of the zigzag tape was excluded and a smooth contact edge between the fin and rudder was created to simplify the geometry of the CFD model. This caused the transition point to shift towards the inner edge of the rudder, creating a larger laminar boundary. As the fin is of interest and not the rudder, the shift in the transition point was deemed acceptable.

It was concluded that the simulation provided sufficient visual confirmation on external airflow replication compared to the oil test and, therefore, can be used for external airflow comparison to total energy probe designs. An ideal model of the JS-1C fin without the total energy probe was created to compare with the current probe CFD and determine the theoretical drag induced by the probe.

7.3 Ideal JS-1C drag

The current probe CFD was modified to exclude the total energy probe to recreate an ideal JS-1C fin model without parasitic drag (Figure 7-3).

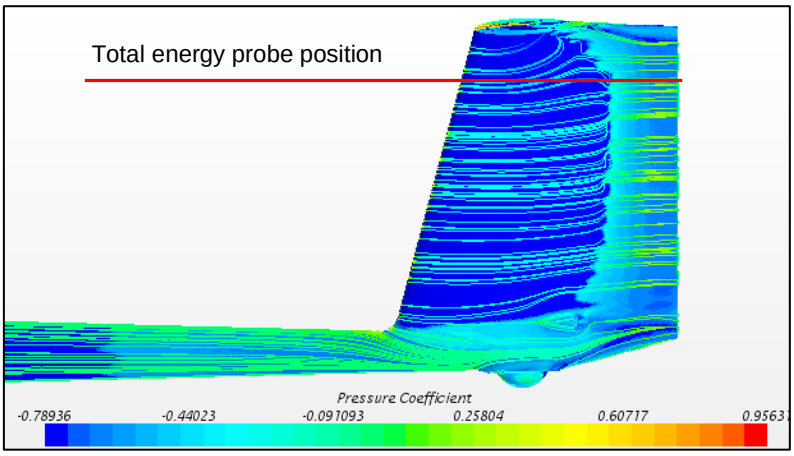

Figure 7-3: **Ideal JS-1C CFD without the total energy probe**

A two dimensional XFOIL simulation was done to verify the transition point calculated in the CFD, as well as verify the behaviour of the boundary layer on the ideal JS-1C fin (Figure 7-4).

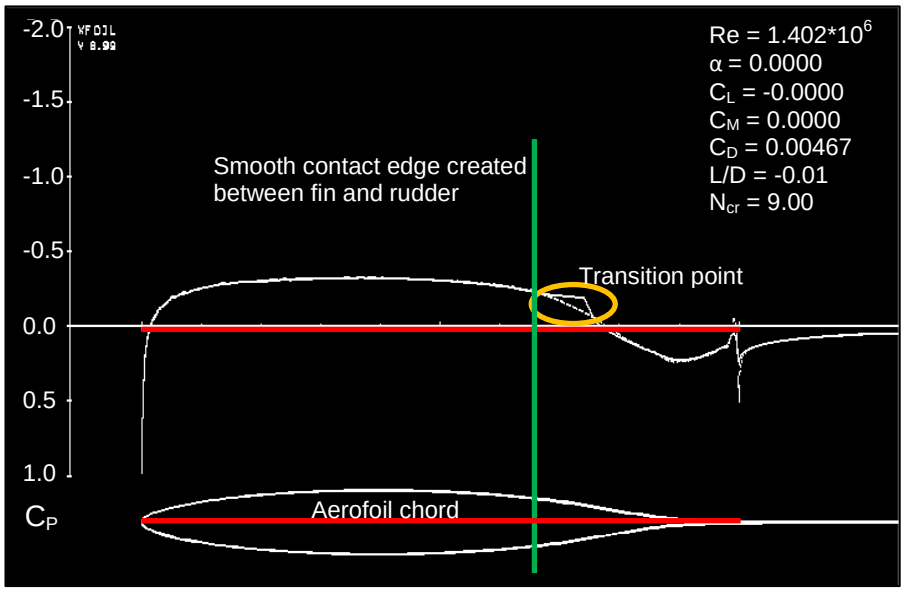

Figure 7-4: **Pressure distribution over the vertical tail fin without the total energy probe**

The simulation shows where the laminar boundary layer is present across the surface of the fin and the transition point from the laminar boundary layer to the turbulent boundary layer. The position of the transition point in the CFD simulation corresponds with the XFOIL simulation and, therefore, the ideal JS-1C CFD can be used as a baseline drag analysis model. The baseline was compared to the current probe CFD to determine the extent of the drag induced by the current total energy probe.

7.4 Theoretical total energy probe drag

The current probe CFD was compared to the baseline CFD (ideal JS-1C without a total energy probe). The laminar boundary layer on the surface of the fin was disturbed by the presence of the probe and created a large turbulent wake across the surface (Figure 7-5).

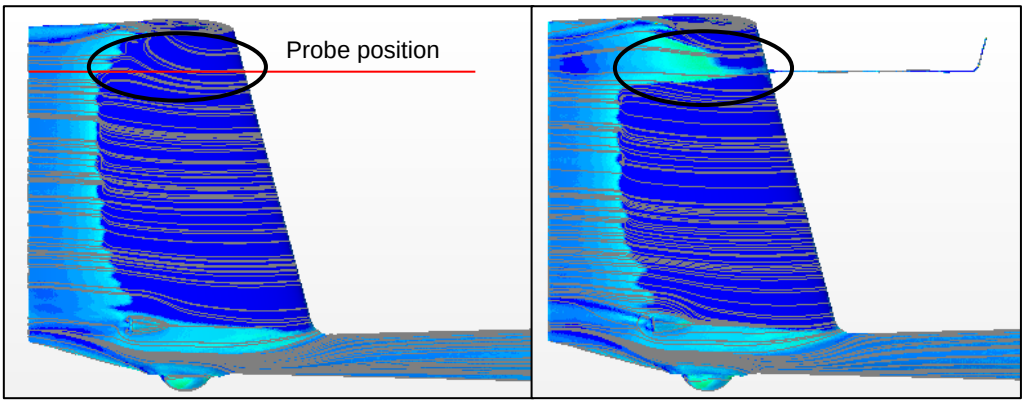

Figure 7-5: **External airflow of the baseline CFD (left) compared to the current probe CFD (right)**

The shear stresses between the air and the surface of the fin cause the air in the area of the turbulent wake to flow towards the bottom surface of the horizontal tail plane on the baseline. The transition from laminar to turbulent airflow in the current probe CFD causes the air to break away from the surface of the fin. The turbulent airflow conforms to the direction of the flight path where it flows nearly parallel with the bottom surface of the horizontal tail plane.

Table 7-4: **Drag calculated over the surface of the tail fin by the current probe**

CAS	Drag (N)		Difference	
km/h	Ideal JS-1C	Current probe	N	%
95	4.42	4.65	0.23	5.2
118	6.62	6.97	0.35	5.2
156	11.23	11.81	0.59	5.2
175	14.36	15.04	0.69	4.8
204	19.84	20.76	0.92	4.6

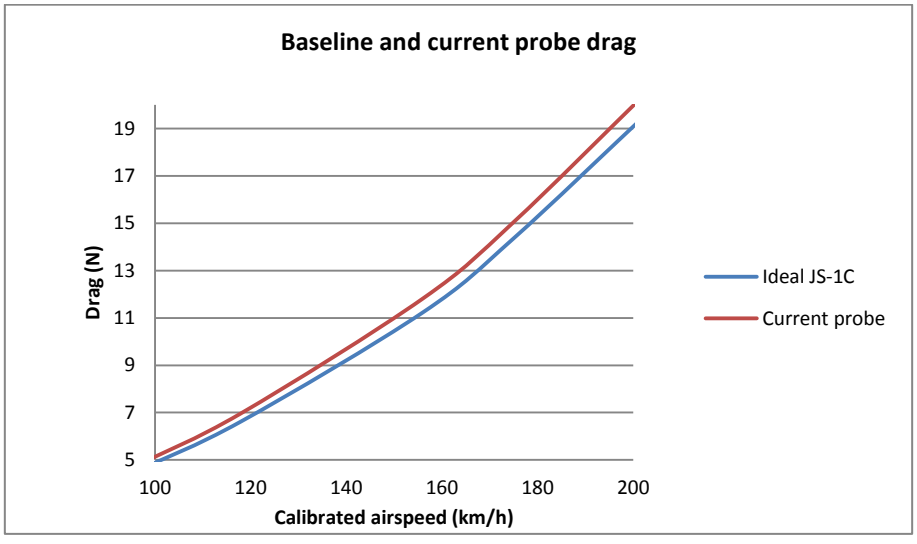

Figure 7-6: **Calculated drag induced over the surface of the fin for the ideal JS-1C and current probe models**

The current total energy probe caused an average drag increase of 5 % over the left surface of the fin (Table 7-4). The drag coefficient remained nearly constant with the change in airspeed at an average of around 0.0046 for both the ideal JS-1C and current probe (Figure 7-6).

7.5 Conclusion

The CFD program was verified for drag force calculation and external airflow replication. The influence of the current total energy probe on the laminar boundary layer of the JS-1C vertical tail fin was determined and the theoretical drag force induced by the probe calculated.

The drag behaviour calculated by the different meshing models for the complex geometry did not correspond with that of the simple aerofoil. It was concluded that the CFD program can determine which total energy probe configuration or design induces the most and least drag if the same meshing model is used to compare the data (paragraph 7.1.3). However, discretion must be used when determining with exactly how much drag force they differentiate from one another.

The polyhedral mesh was therefore chosen to calculate and compare the drag force of total energy probe configurations and designs, since it was chosen to recreate the flight test data (paragraph 6.5).

A baseline CFD model of the JS-1C without a total energy probe was created and compared to the current probe CFD to calculate the drag induced by the probe, which determined the maximum drag a total energy probe configuration or design may induce.

Based on the data collected for the current probe position, concept designs were created and applied to the sides of the vertical tail fin to try and reduce the drag induced by the current total energy probe.

CHAPTER 8: REDESIGN OF THE TOTAL ENERGY PROBE ON THE VERTICAL TAIL FIN

Total energy probe concepts were designed and applied to the sides of the vertical tail fin where they (1) could not be influenced by the pressure over the wings and fuselage and (2) would induce less drag than the current probe.

8.1 Concept design 1 – Prominent fin protrusion

The aim of the design is to move and redesign the probe for the sides of the vertical tail fin. The skin was misshaped to create an incline and form a sudden surface drop (Figure 8-1).

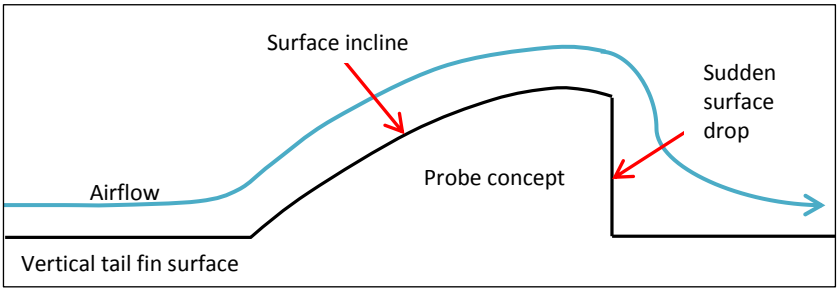

Figure 8-1: **Prominent fin protrusion principle**

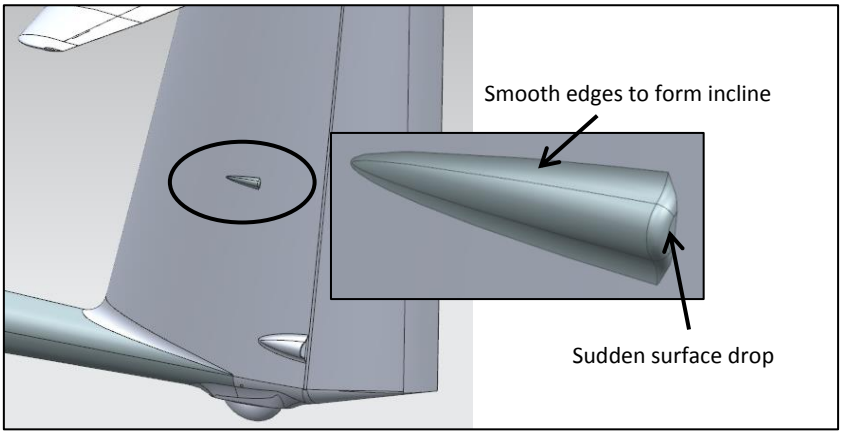

Figure 8-2: **Prominent fin protrusion CAD model**

The air flows along the surface incline and accelerates as it flows over the edge, creating an area of low pressure (Figure 8-2).

8.1.1 Drag analysis

A CFD model was created to analyse the drag along the surface of the probe concept. The design created no turbulent wake up until the surface drop and the wake thereafter was significantly smaller (Figure 8-3) compared to that of the current total energy probe (Figure 7-5).

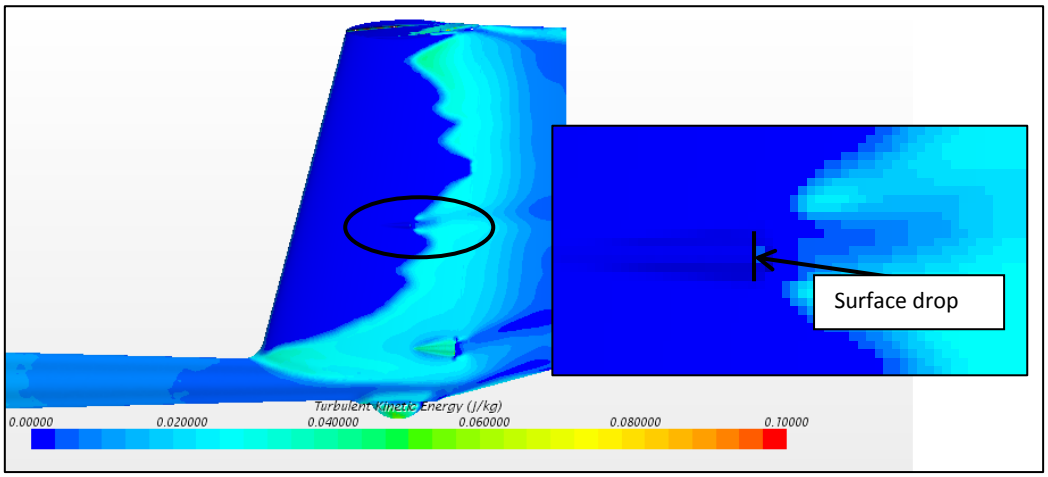

Figure 8-3: **Drag analysis of the prominent fin protrusion using CFD**

Table 8-1: **Drag calculated using CFD for the prominent fin protrusion**

CAS	Drag (N)			Difference from ideal JS-1C		Difference from current probe	
km/h	Ideal JS-1C	Current probe	Concept design 1	N	%	N	%
95	4.42	4.65	4.52	0.11	2.4	-0.12	-2.6
118	6.62	6.97	6.76	0.14	2.1	-0.21	-3.0
156	11.23	11.81	11.55	0.32	2.9	-0.26	-2.2
175	14.36	15.04	14.77	0.41	2.9	-0.28	-1.8
204	19.84	20.76	20.22	0.38	1.9	-0.54	-2.6

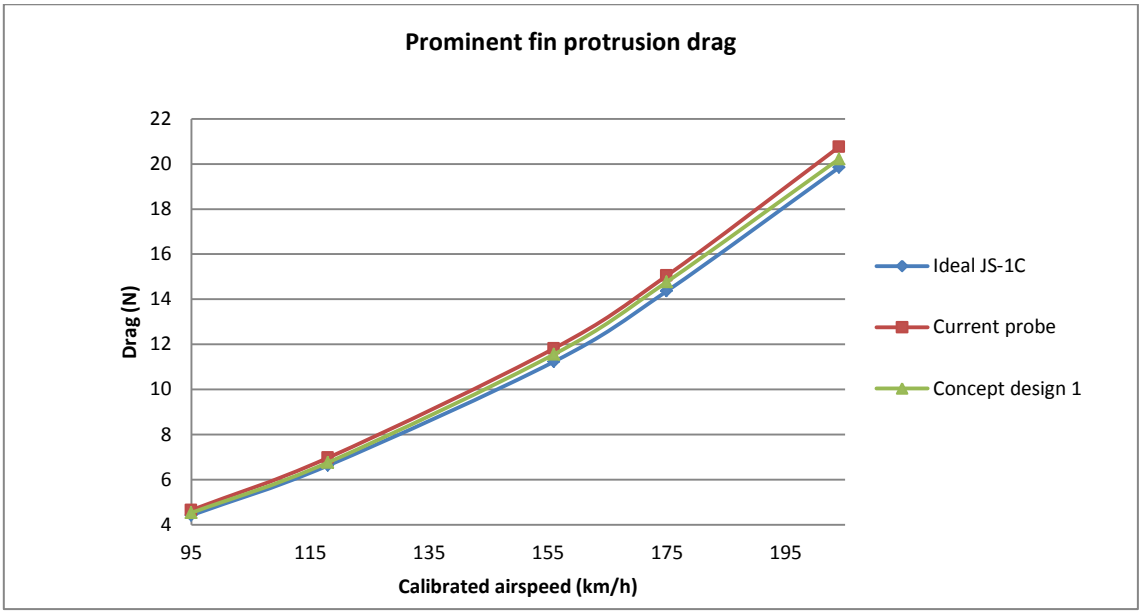

Figure 8-4: **Drag calculated using CFD for the prominent fin protrusion**

The average drag force increase was 2.4 % on the left side of the fin, which is half of that induced by the current probe in paragraph 7.4 of 5 % (Table 8-1 and Figure 8-4).

8.1.2 Compensation characteristics analysis

A plane was created through the cross-section of the design to determine the area of lowest pressure where the probe opening was positioned (Figure 8-5).

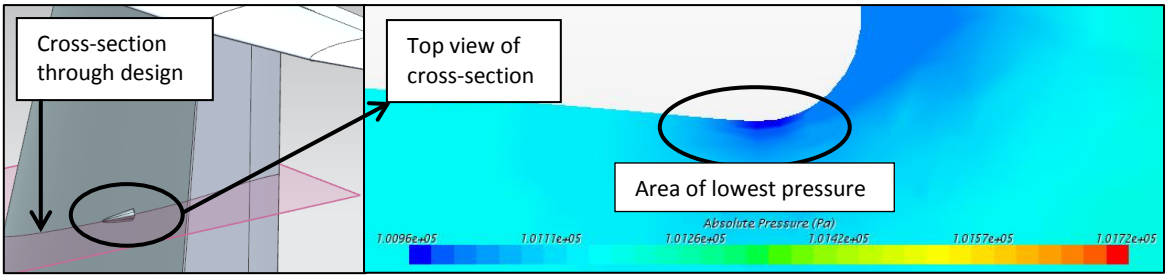

Figure 8-5: **Absolute pressure scalar plane created through the cross-section of the prominent fin protrusion**

The following data was calculated using CFD for straight and level flight (Table 8-2):

Table 8-2: **Pressure drop calculated for straight and level flight using CFD for the prominent fin protrusion**

Theoretical model			Current probe		Concept design 1	
CAS	Pressure drop	Cp	Pressure drop	Cp	Pressure drop	Cp
km/h	Pa	-	Pa	-	Pa	-
95	-446	-1.00	-334	-0.75	-378	-0.85
118	-679	-1.00	-526	-0.78	-596	-0.88
156	-1189	-1.00	-1020	-0.86	-1066	-0.90
175	-1505	-1.00	-1311	-0.87	-1352	-0.90
204	-2037	-1.00	-1834	-0.90	-1852	-0.91

The average pressure coefficient calculated was within the boundary between the theoretical model and current probe of -1.00 and -0.83 respectively. The CFD model for straight and level flight was modified to simulate pitch and sideslip manoeuvres of 10° (Table 8-3).

Table 8-3: **Pressure drop calculated during pitch and sideslip manoeuvres using CFD for the prominent fin protrusion**

CAS	Straight and level	Pitch 10° down		Pitch 10° up		Sideslip 10°	
km/h	Pressure drop (Pa)	Pressure drop (Pa)	Difference (%)	Pressure drop (Pa)	Difference (%)	Pressure drop (Pa)	Difference (%)
95	-378	-444	17.7	-268	-29.1	-317	-16.0
118	-596	-693	16.3	-419	-29.8	-501	-16.0
156	-1066	-1226	15.0	-744	-30.2	-893	-16.3
175	-1352	-1545	14.3	-944	-30.2	-1140	-15.7
204	-1852	-2122	14.6	-1295	-30.1	-1570	-15.2

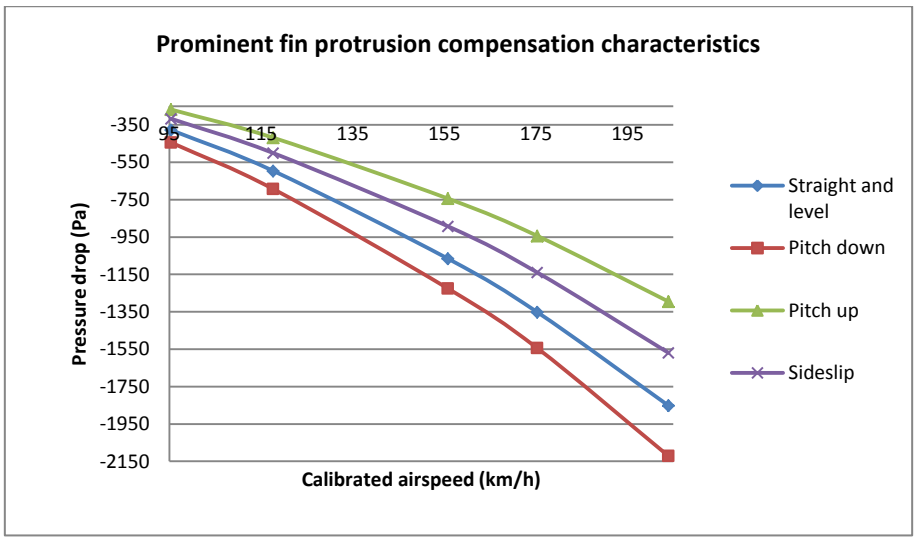

Figure 8-6: Compensation characteristics calculated using CFD for the prominent fin protrusion

The design is much more sensitive to changes in pitch than the current probe, where the average pressure drop change calculated for the climb was 30 % and the dive 16 % (Figure 8-6). The change in sideslip was 16 %, compared to that of the current probe in paragraph 6.3 of 14 %.

8.1.3 Discussion

The design created a large velocity vortex after the surface drop (Figure 8-7). The reduction of the vortex should further reduce the drag induced by the design and reduce the change in pressure drop during manoeuvres.

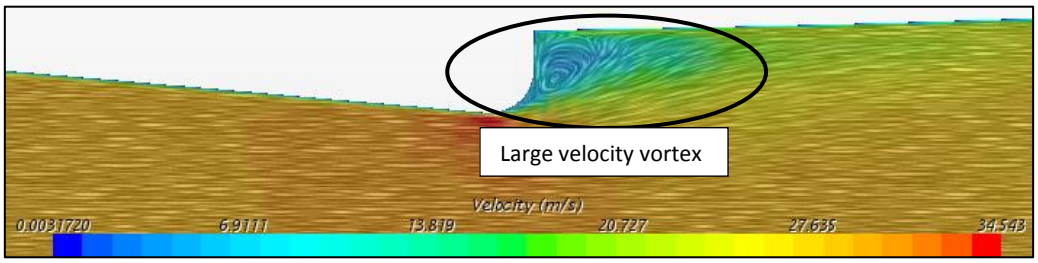

Figure 8-7: Velocity vector plane created through the cross-section of the prominent fin protrusion

8.2 Concept design 2 – Mild fin protrusion

The design is based on the prominent fin protrusion and aimed to reduce the velocity vortex caused by the sudden surface drop (Figure 8-8). The sudden surface drop was sloped to allow the air to flow along the surface more easily after the incline (Figure 8-9).

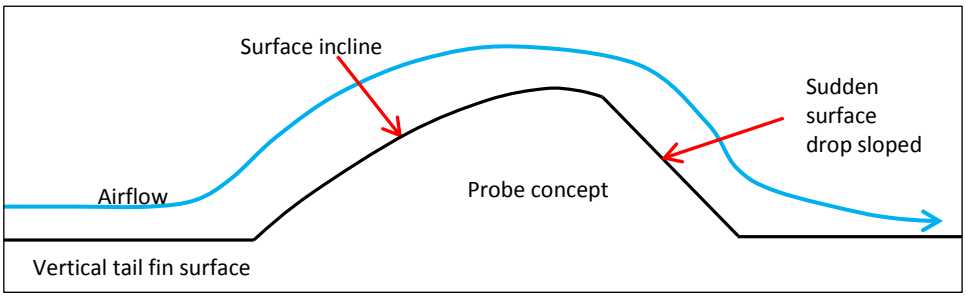

Figure 8-8: **Mild fin protrusion principle**

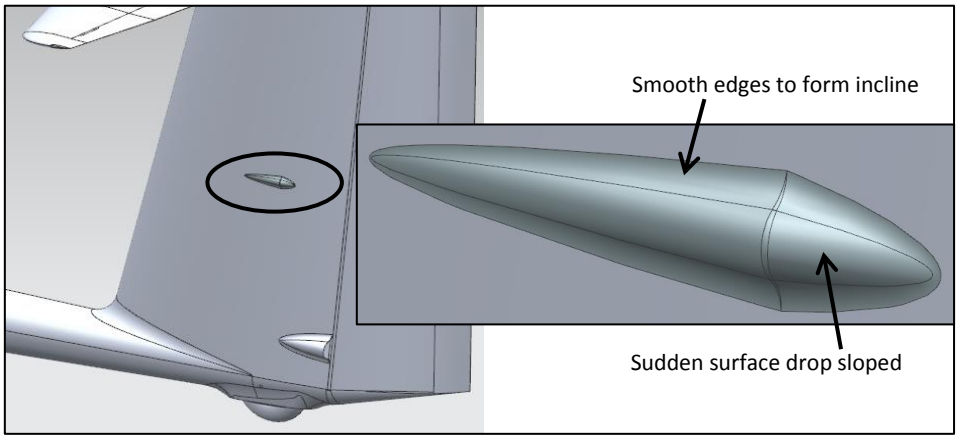

Figure 8-9: **Mild fin protrusion CAD model**

The slope allows the velocity vortex to reduce as the air flows along the probe after passing the edge of the incline without separating from the surface.

8.2.1 Drag analysis

A CFD model was created to analyse the drag along the surface of the probe concept (Figure 8-10). The size of the turbulent wake was greater than the prominent fin protrusion (Figure 8-3), but still significantly smaller than that of the current probe. The average drag force increase on the left surface of the fin was 2 %, which is less than half of that induced by the current probe (Table 8-4).

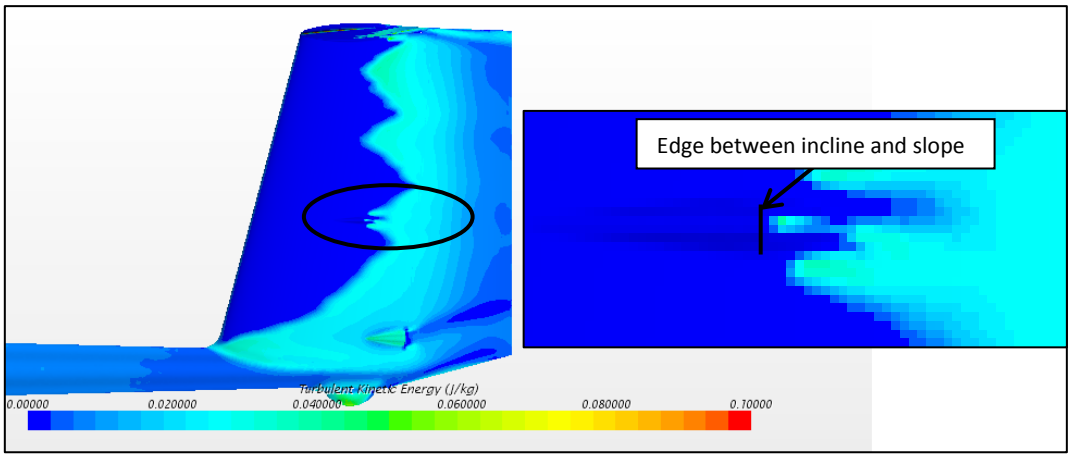

Figure 8-10: **Drag analysis of the mild fin protrusion using CFD**

Table 8-4: Drag calculated using CFD for the mild fin protrusion

CAS	Drag (N)			Difference from ideal JS-1C		Difference from current probe	
km/h	Ideal JS-1C	Current probe	Concept design 2	N	%	N	%
95	4.42	4.65	4.50	0.08	1.9	-0.14	-3.1
118	6.62	6.97	6.77	0.15	2.2	-0.20	-2.8
156	11.23	11.81	11.48	0.26	2.3	-0.33	-2.8
175	14.36	15.04	14.64	0.28	2.0	-0.41	-2.7
204	19.84	20.76	20.15	0.31	1.6	-0.60	-2.9

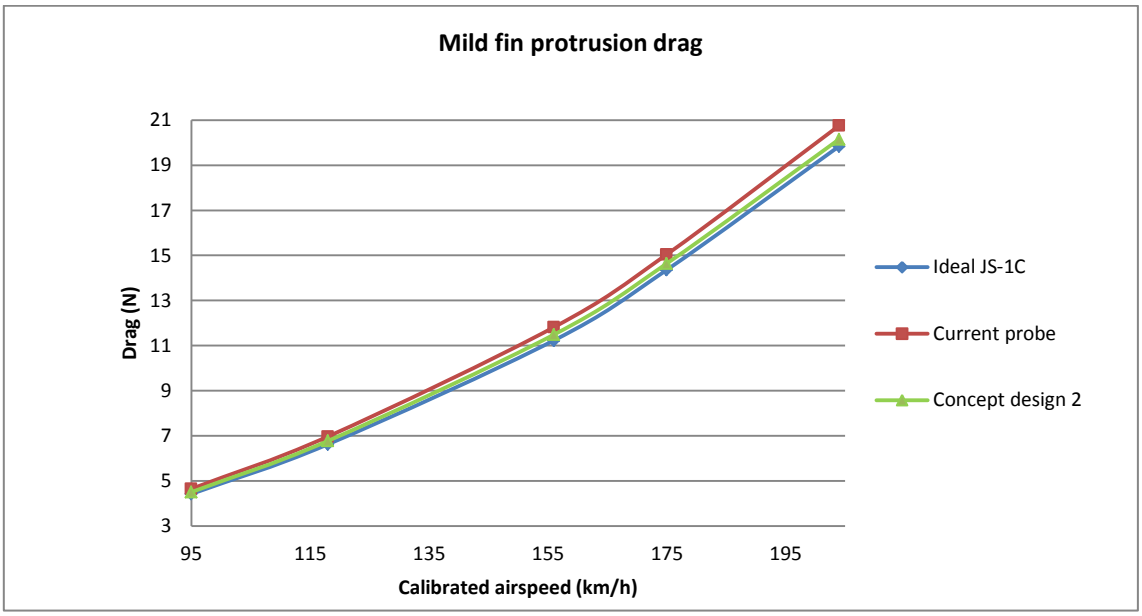

Figure 8-11: Drag calculated using CFD for the mild fin protrusion

The reduction of the velocity vortex caused a small reduction in the drag compared to the prominent fin protrusion (Figure 8-11).

8.2.2 Compensation characteristics analysis

A plane was created through the cross-section of the design to determine the area of lowest pressure where the probe opening was positioned (Figure 8-12).

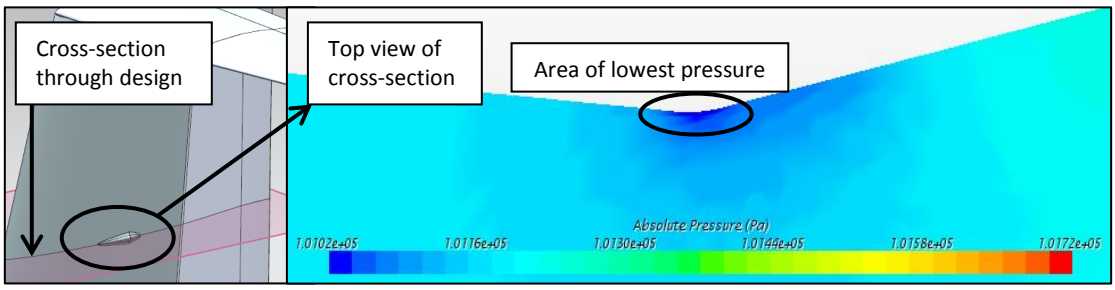

Figure 8-12: Absolute pressure scalar plane created through the cross-section of the mild fin protrusion

The following data was calculated using CFD for straight and level flight (Table 8-5):

Table 8-5: **Pressure drop calculated for straight and level flight using CFD for the mild fin protrusion**

Theoretical model			Current probe		Concept design 2	
CAS	Pressure drop	Cp	Pressure drop	Cp	Pressure drop	Cp
km/h	Pa	-	Pa	-	Pa	-
95	-446	-1.00	-334	-0.75	367	-0.82
118	-679	-1.00	-526	-0.78	581	-0.86
156	-1189	-1.00	-1020	-0.86	1047	-0.88
175	-1505	-1.00	-1311	-0.87	1335	-0.89
204	-2037	-1.00	-1834	-0.90	1851	-0.91

The average pressure coefficient calculated was within the boundary between the theoretical model and current probe. The CFD model for straight and level flight was modified to simulate pitch and sideslip manoeuvres of 10° (Table 8-6).

Table 8-6: **Pressure drop calculated during pitch and sideslip manoeuvres using CFD for the mild fin protrusion**

CAS	Straight and level	Pitch 10° down		Pitch 10° up		Sideslip 10°	
km/h	Pressure drop (Pa)	Pressure drop (Pa)	Difference (%)	Pressure drop (Pa)	Difference (%)	Pressure drop (Pa)	Difference (%)
95	-367	-368	0.5	-325	-11.3	-323	-11.9
118	-581	-580	-0.2	-512	-11.9	-512	-11.9
156	-1047	-1036	-1.1	-918	-12.4	-915	-12.6
175	-1335	-1315	-1.5	-1163	-12.9	-1160	-13.1
204	-1851	-1802	-2.6	-1596	-13.8	-1596	-13.8

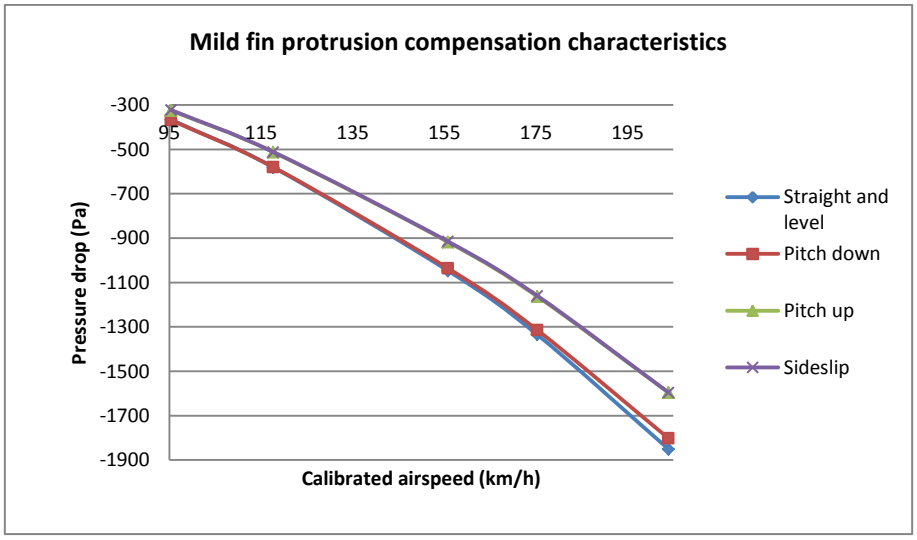

Figure 8-13: **Compensation characteristics calculated using CFD for the mild fin protrusion**

The average pressure drop change during pitch improved greatly compared to the prominent fin protrusion, where the climb calculated was 12 % and the dive 1 % (Figure 8-13). The change in sideslip was slightly better than the current probe with 13 %.

8.2.3 Discussion

The velocity vortex of the prominent fin probe was significantly reduced (Figure 8-14). The slope allowed the air to flow along the probe with minimum separation from the surface. The reduction of the vortex also improved the compensation characteristics of the design and reduced the drag the probe induced on the surface of the fin.

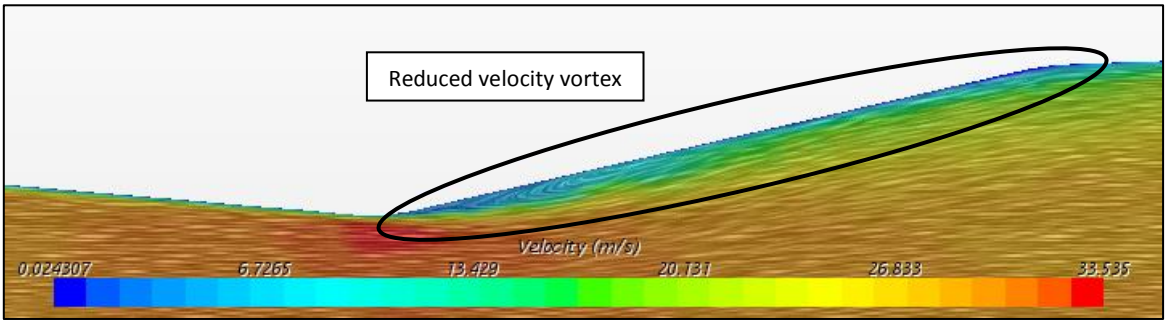

Figure 8-14: Velocity vector plane created through the cross-section of the mild fin protrusion

8.3 Discussion

The implementation of a total energy probe on the skin of the sailplane to promote drag reduction could benefit the JS-1C. Further research and design refinement is required to ensure that the mild fin protrusion concept measured a uniform average pressure drop change during pitch manoeuvres.

8.4 Conclusion

Total energy probe concepts were designed for the sides of the vertical tail fin to move the premature boundary layer transition caused by the probe closer to the trailing edge of the fin to reduce the parasitic drag.

The mild fin protrusion concept could benefit the drag performance of the JS-1C if finer design changes are implemented to ensure uniform average pressure drop changes during pitch manoeuvres, along with the slight improvement during sideslip.

The concept experiment (RFC document) described in paragraph 2.6 was recreated to determine whether simply moving the total energy probe to the horizontal tail plane would sufficiently reduce the drag induced without reducing the compensation capabilities of the probe.

CHAPTER 9: RELOCATION OF THE TOTAL ENERGY PROBE TO THE HORIZONTAL TAIL PLANE

The concept experiment described in paragraph 2.6, where the probe was installed on the tip of the horizontal tail plane, was recreated in CFD. The concept aimed to reduce the drag induced by the total energy probe by simply moving it to a different location, while retaining the same compensation characteristics of the current probe.

A drag analysis was conducted on the concept experiment to determine if the drag could be significantly decreased when simply moving the probe.

9.1 Drag analysis

The concept experiment was recreated and compared to the baseline in paragraph 7.3 using CFD (Figure 9-1). The tip, which was originally subjected to laminar flow, now experienced turbulent flow. The size of the turbulent wake was significantly less than that of the current probe position (Figure 7-5).

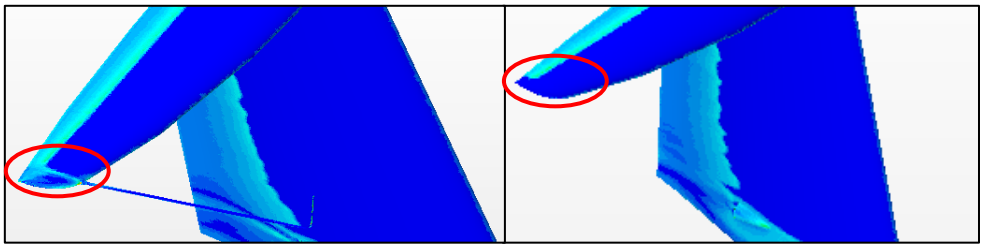

Figure 9-1: **External airflow of the horizontal tail plane tip probe (left) compared to the baseline (right)**

Table 9-1: **Drag calculated using CFD for the tail plane tip probe**

CAS	Drag (N)			Difference from ideal JS-1C		Difference from current probe	
km/h	Ideal JS-1C	Current probe	Tail plane tip probe	N	%	N	%
95	4.42	4.65	4.77	0.35	8.0	0.12	2.7
118	6.62	6.97	7.16	0.53	8.1	0.19	2.7
156	11.23	11.81	12.18	0.95	8.5	0.36	3.1
175	14.36	15.04	15.40	1.04	7.3	0.36	2.4
204	19.84	20.76	21.32	1.48	7.5	0.57	2.7

An average drag force increase of 7.8 % was calculated, which is 1.5 times more than the current probe in paragraph 7.4 of 5 % (Table 9-1 and Figure 9-2). The surface area downwind of the total energy probe, when positioned on the tip of the tail plane, is much less than that of the current probe position and should, therefore, induce less drag.

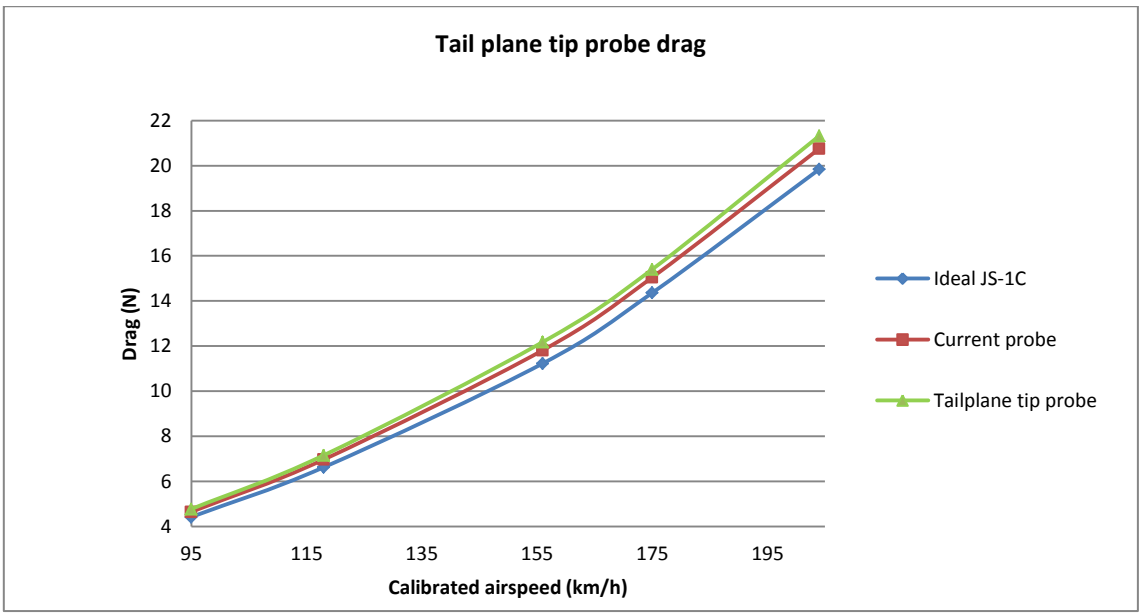

Figure 9-2: Drag calculated using CFD for the tail plane tip probe

An analysis was conducted on the surface of the tail plane to determine the cause of the drag increase.

9.2 Horizontal tail plane surface analysis

A velocity vector and turbulent airflow analysis was conducted on the tail plane using CFD to try and identify the cause of the drag increase when moving the probe to the tip of the tail plane.

9.2.1 Velocity vector analysis

Cross-section planes were created on the tail plane of the concept experiment and baseline to study the effect of the probe on the airflow over the surfaces of the tail plane (Figure 9-3).

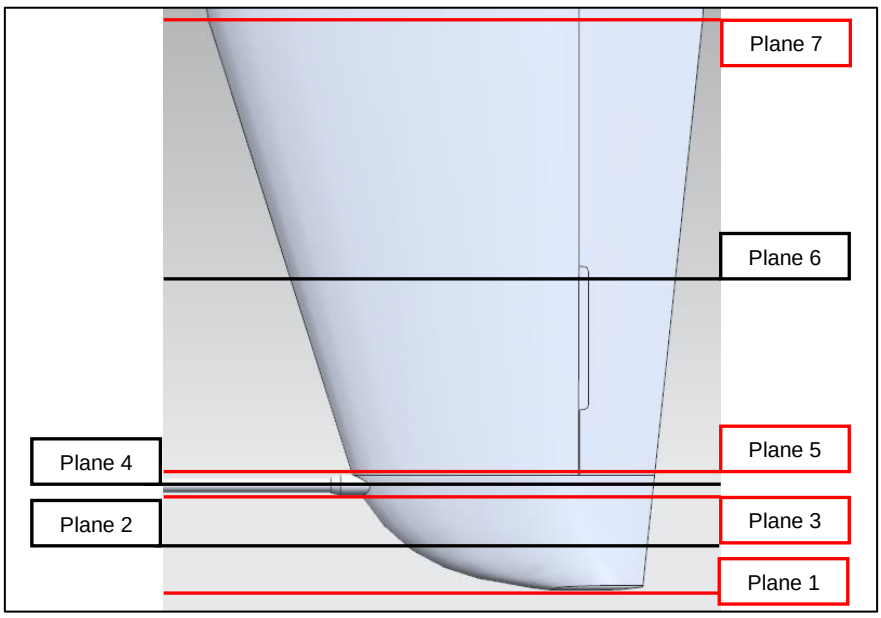

Figure 9-3: Cross-section planes created through the tail plane of the concept experiment CFD

There is a slight increase in the velocity over the bottom surface of the tail plane near the leading edge at the section plane (plane 7) positioned at around a quarter length of the left side of the tail plane (Figure 9-4). The velocity in the same area experiences a slight decrease when moving towards the tip of the tail plane (plane 6) (Figure 9-5) and a reduction in velocity over the top and bottom surfaces is clearly visible at the root side of the probe (plane 5) (Figure 9-6).

The velocity of the airflow over the top and bottom surfaces is nearly the same at the centre of the probe (plane 4) (Figure 9-7) and the airflow on the tip side of the probe (plane 3) is nearly the same as that observed at the root side of the probe (plane 5) (Figure 9-8).

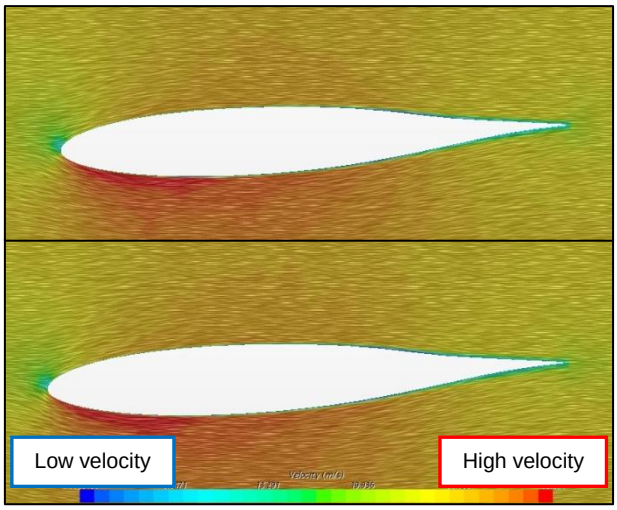

Figure 9-4: **Velocity vector plane 7 created through the tail plane of the baseline (top) and concept experiment (bottom) CFD**

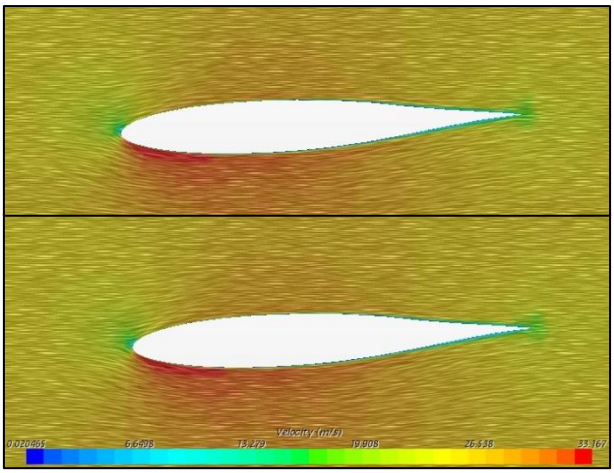

Figure 9-5: **Velocity vector plane 6 created through the tail plane of the baseline (top) and concept experiment (bottom) CFD**

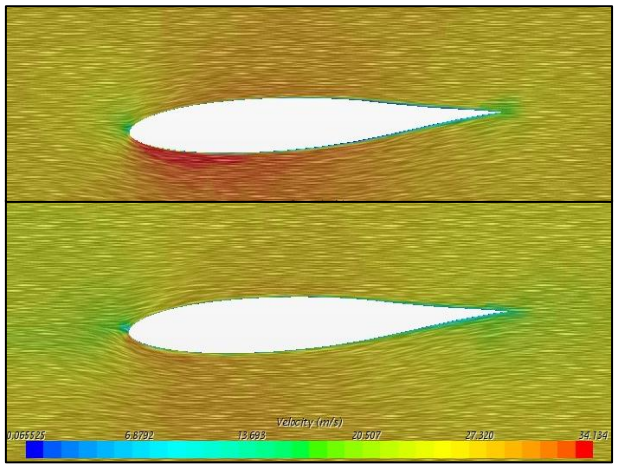

Figure 9-6: **Velocity vector plane 5 created through the tail plane of the baseline (top) and concept experiment (bottom) CFD**

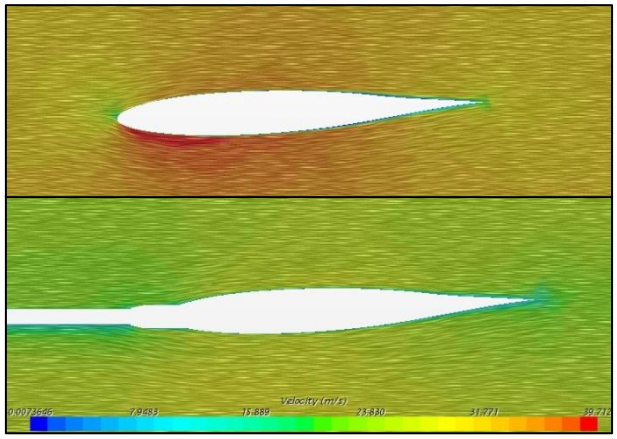

Figure 9-7: **Velocity vector plane 4 created through the tail plane of the baseline (top) and concept experiment (bottom) CFD**

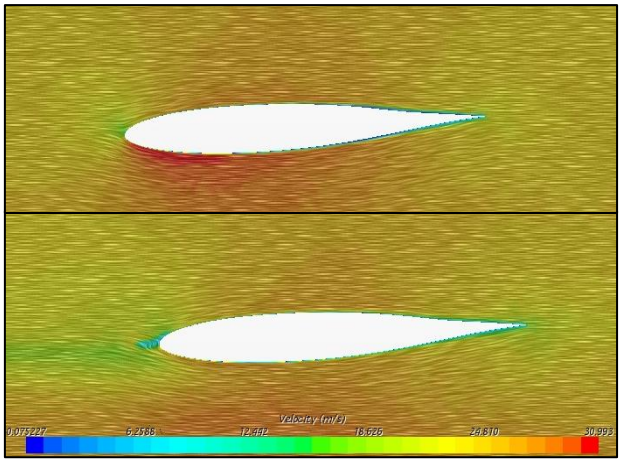

Figure 9-8: **Velocity vector plane 3 created through the tail plane of the baseline (top) and concept experiment (bottom) CFD**

The velocity increases over the bottom surface near the leading edge halfway between the probe and the tip of the tail plane (plane 2) (Figure 9-9) and a slightly more turbulent wake occurs, which is difficult to observe, at the tip of the tail plane (plane 1) (Figure 9-10).

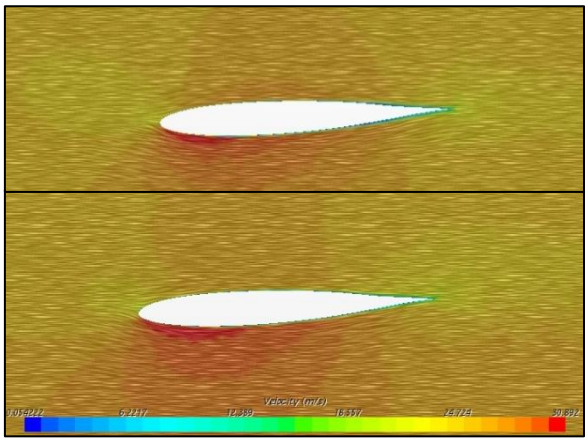

Figure 9-9: **Velocity vector plane 2 created through the tail plane of the baseline (top) and concept experiment (bottom) CFD**

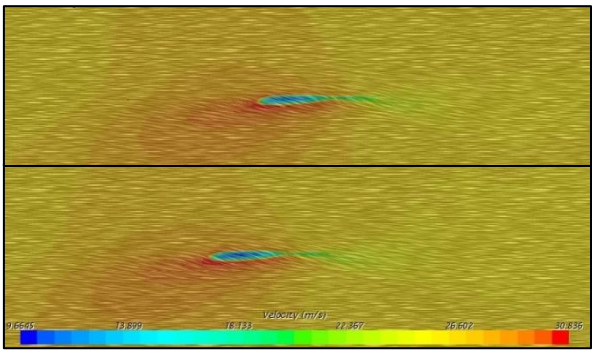

Figure 9-10: **Velocity vector plane 1 created through the tail plane of the baseline (top) and concept experiment (bottom) CFD**

The velocity vectors normal to the surfaces of the tail plane were analysed to observe minor changes to the airflow more easily. Small changes occur close to the root of the tail plane (Figure 9-11), with significant changes visible at the centre of the probe, as expected (Figure 9-12). The turbulent wake at the trailing edge of the tail plane is slightly more erratic due to the presence of the probe (Figure 9-13).

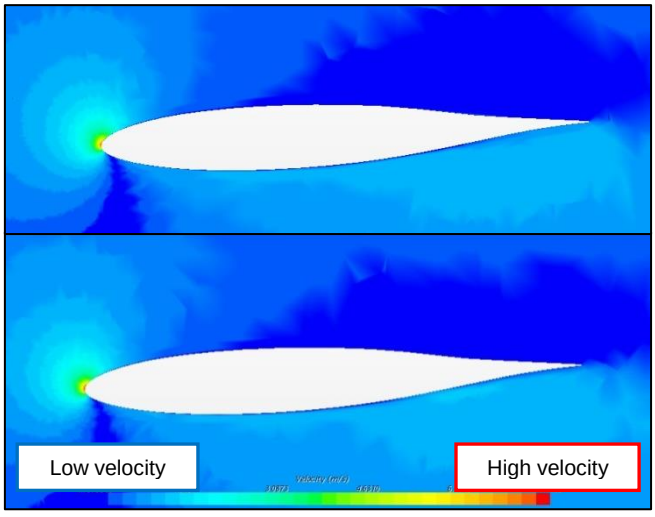

Figure 9-11: **Normal velocity vector plane 7 created through the tail plane of the baseline (top) and concept experiment (bottom) CFD**

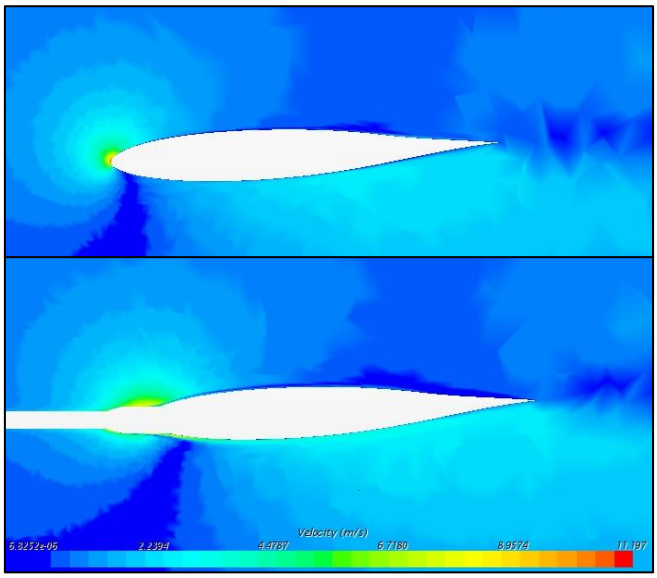

Figure 9-12: **Normal velocity vector plane 4 created through the tail plane of the baseline (top) and concept experiment (bottom) CFD**

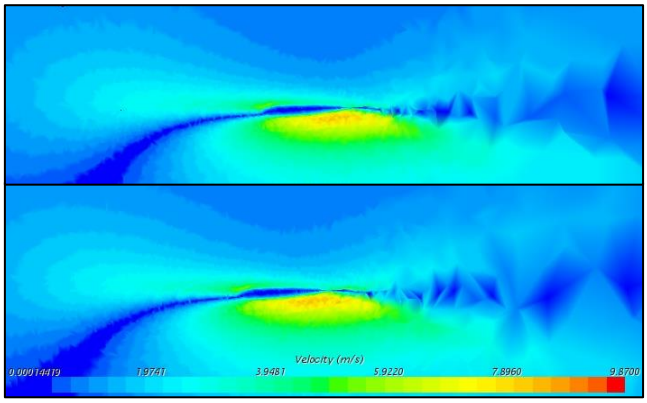

Figure 9-13: **Normal velocity vector plane 1 created through the tail plane of the baseline (top) and concept experiment (bottom) CFD**

The velocity vector analysis did not reveal any significant changes, except at the probe location, in the airflow that could explain the drag increase calculated in paragraph 9.1.

A turbulent airflow analysis was conducted to analyse the surfaces of the tail plane in greater detail.

9.2.2 Turbulent airflow analysis

Cross-section planes were added to the existing planes in paragraph 9.2.1 to observe whether the probe could influence the airflow of the tail plane closer to the root and in greater detail (Figure 9-14).

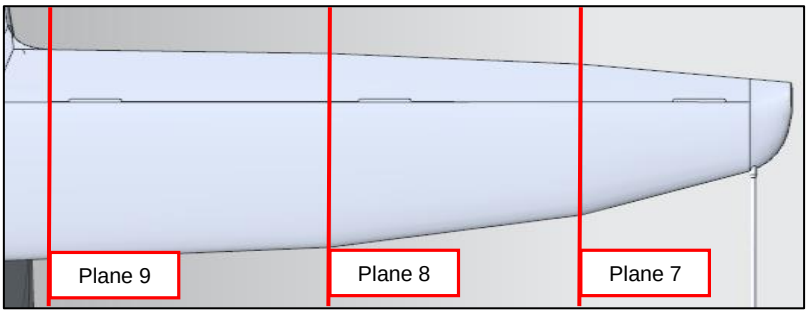

Figure 9-14: **Additional cross-section planes created through the tail plane of the concept experiment CFD**

There are no significant changes observed at the root of the left side of the tail plane (Figure 9-15). The effect of the probe becomes more evident in the turbulent wake that forms at the trailing edge of the tail plane when moving closer to the tip (Figure 9-16 and Figure 9-17).

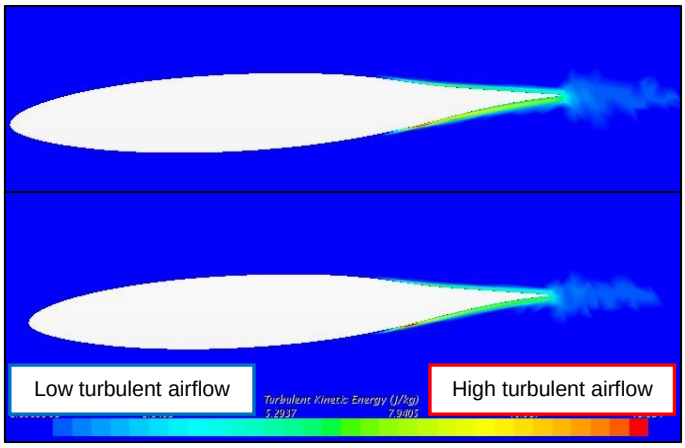

Figure 9-15: **Turbulent kinetic energy scalar plane 9 created through the tail plane of the baseline (top) and concept experiment (bottom) CFD**

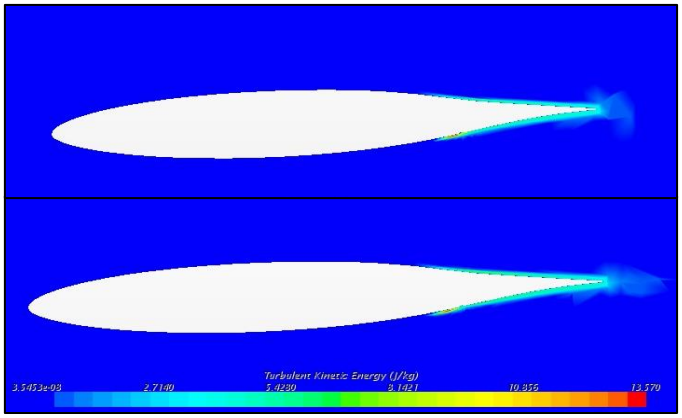

Figure 9-16: **Turbulent kinetic energy scalar plane 8 created through the tail plane of the baseline (top) and concept experiment (bottom) CFD**

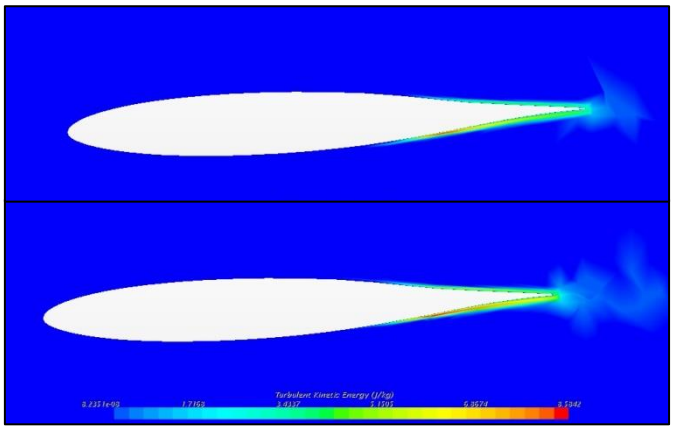

Figure 9-17: **Turbulent kinetic energy scalar plane 7 created through the tail plane of the baseline (top) and concept experiment (bottom) CFD**

The probe causes significant turbulent airflow over the surfaces of the tail plane at the centre of the probe (Figure 9-18), as well as significant turbulence at the tip of the tail plane (Figure 9-19).

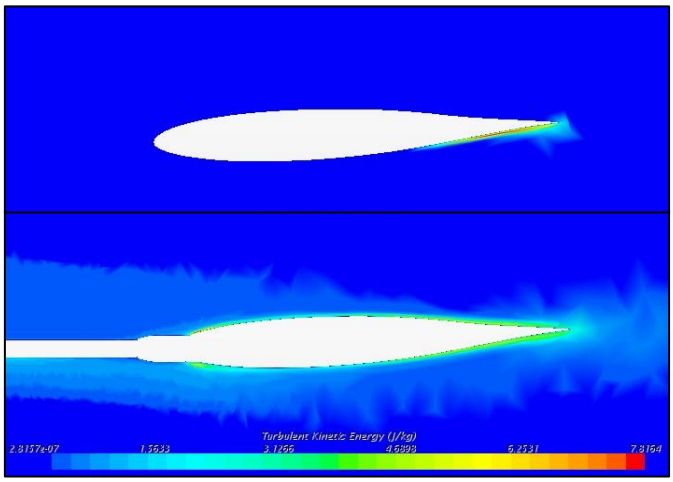

Figure 9-18: **Turbulent kinetic energy scalar plane 4 created through the tail plane of the baseline (top) and concept experiment (bottom) CFD**

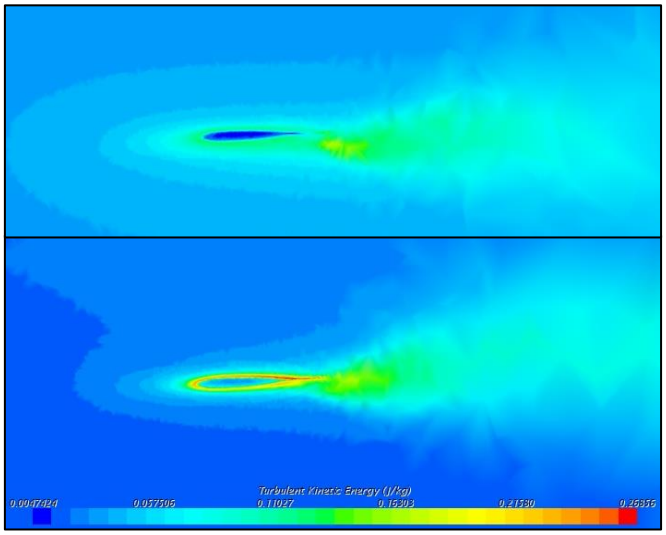

Figure 9-19: **Turbulent kinetic energy scalar plane 1 created through the tail plane of the baseline (top) and concept experiment (bottom) CFD**

It is evident that the probe positioned on the tip of the tail plane causes small changes to the airflow over nearly half of the tail plane and significant changes at the tip and probe location.

9.2.3 Discussion

There were no significant changes observed, except at the centre of the probe position and tip, which could cause the drag to increase significantly. However, the effect of the probe position stretches to nearly half of the tail plane. These minor changes over a large area, along with the significant changes at the tip and probe location, could cause the drag increase calculated in paragraph 9.1 which is greater than that of the current total energy probe.

9.3 Compensation characteristics

The relocation of the current probe to the horizontal tail plane should not influence the compensation characteristics thereof, as long as the probe is installed with the same angles as that of the current probe with respect to the longitudinal, latitudinal and vertical axis of the fuselage. Based on the data collected for the total energy probe relocated to the tail plane, concept designs were created by modifying and redesigning the probe for the tail plane tip (continued from the concept designs described in paragraph 8.1 and 8.2).

9.4 Concept design 3 – Tail plane tip extension

The aim of the concept design is to reduce the influence of the probe over the surfaces of the tail plane by reducing the surface area of the probe itself and positioning it closer to the tip.

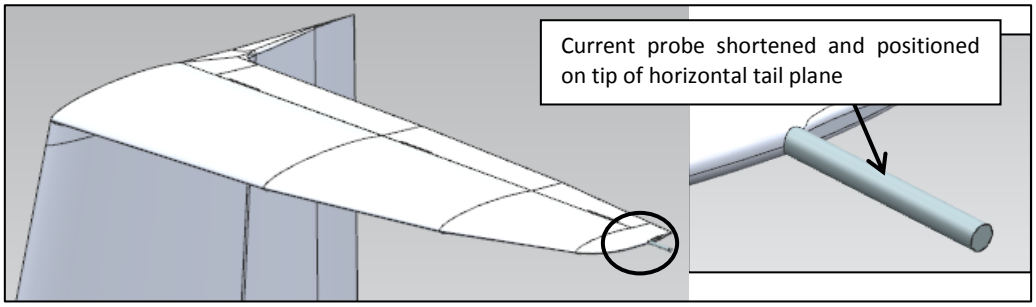

Figure 9-20: Tail plane tip extension CAD model

The design of the current probe was used to extend the probe opening away from the tail plane surfaces to lessen the effect of the pressure difference, where the length was shortened to reduce the surface area and reduce the forces exerted thereon by the air (Figure 9-20).

9.4.1 Drag analysis

A CFD model was created to analyse the drag along the surface of the probe concept. The design created virtually no turbulent wake (Figure 9-21).

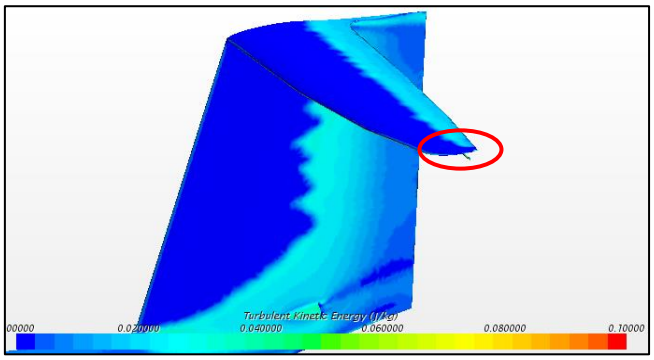

Figure 9-21: **Drag analysis of the tail plane tip extension using CFD**

Table 9-2: **Drag calculated using CFD for the tail plane tip extension**

CAS	Drag (N)			Difference from ideal JS-1C		Difference from current probe	
km/h	Ideal JS-1C	Current probe	Concept design 3	N	%	N	%
95	4.42	4.65	4.62	0.20	4.6	-0.03	-0.6
118	6.62	6.97	6.90	0.27	4.1	-0.07	-1.0
156	11.23	11.81	11.77	0.54	4.8	-0.05	-0.4
175	14.36	15.04	14.94	0.58	4.0	-0.11	-0.7
204	19.84	20.76	20.75	0.91	4.6	0.00	0.0

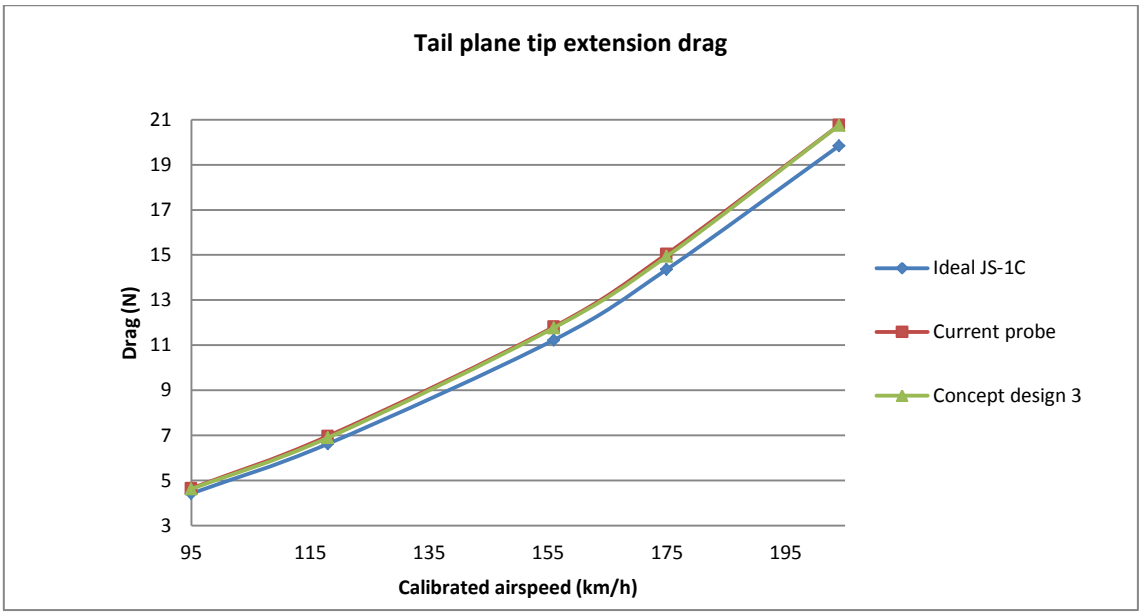

Figure 9-22: **Drag calculated using CFD for the tail plane tip extension**

The average drag force increase was 4.4 % on the left side of the tail plane, which is slightly less than that induced by the current probe (Table 9-2 and Figure 9-22).

9.4.2 Compensation characteristics analysis

A plane was created through the cross-section of the design to determine the area of lowest pressure where the probe opening was positioned (Figure 9-23).

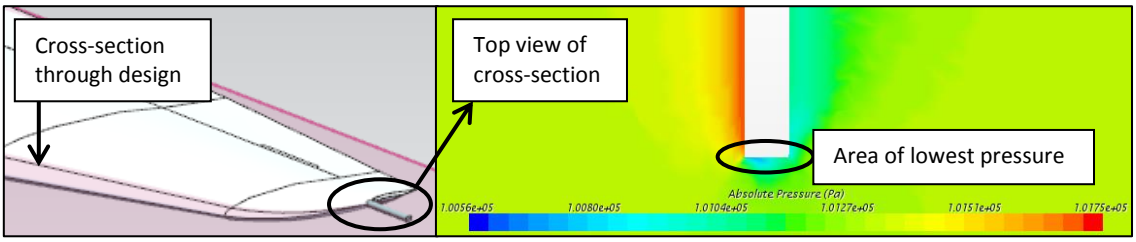

Figure 9-23: **Absolute pressure scalar plane created through the cross-section of the tail plane tip extension**

The following data was calculated using CFD for straight and level flight (Table 9-3):

Table 9-3: **Pressure drop calculated for straight and level flight using CFD for the tail plane tip extension**

Theoretical model			Current probe		Concept design 3	
CAS	Pressure drop	Cp	Pressure drop	Cp	Pressure drop	Cp
km/h	Pa	-	Pa	-	Pa	-
95	-446	-1.00	-334	-0.75	-436	-0.98
118	-679	-1.00	-526	-0.78	-674	-0.99
156	-1189	-1.00	-1020	-0.86	-1169	-0.98
175	-1505	-1.00	-1311	-0.87	-1467	-0.97
204	-2037	-1.00	-1834	-0.90	-1982	-0.97

The average pressure coefficient calculated was within the boundary between the theoretical model and current probe. The CFD model for straight and level flight was modified to simulate pitch and sideslip manoeuvres of 10° (Table 9-4).

Table 9-4: **Pressure drop calculated during pitch and sideslip manoeuvres using CFD for the tail plane tip extension**

CAS	Straight and level	Pitch 10° down		Pitch 10° up		Sideslip 10°	
km/h	Pressure drop (Pa)	Pressure drop (Pa)	Difference (%)	Pressure drop (Pa)	Difference (%)	Pressure drop (Pa)	Difference (%)
95	-436	-471	8.1	-453	4.1	-381	-12.5
118	-674	-719	6.6	-700	3.8	-586	-13.0
156	-1169	-1249	6.8	-1221	4.4	-1022	-12.5
175	-1467	-1600	9.0	-1523	3.8	-1291	-12.0
204	-1982	-2159	9.0	-2044	3.2	-1743	-12.0

The design is slightly more sensitive to changes in pitch than the current probe, where the average pressure drop change calculated for the climb was 4 % and the dive 8 % (Figure 9-24). The change in sideslip was slightly better with 12 % than that of the current probe.

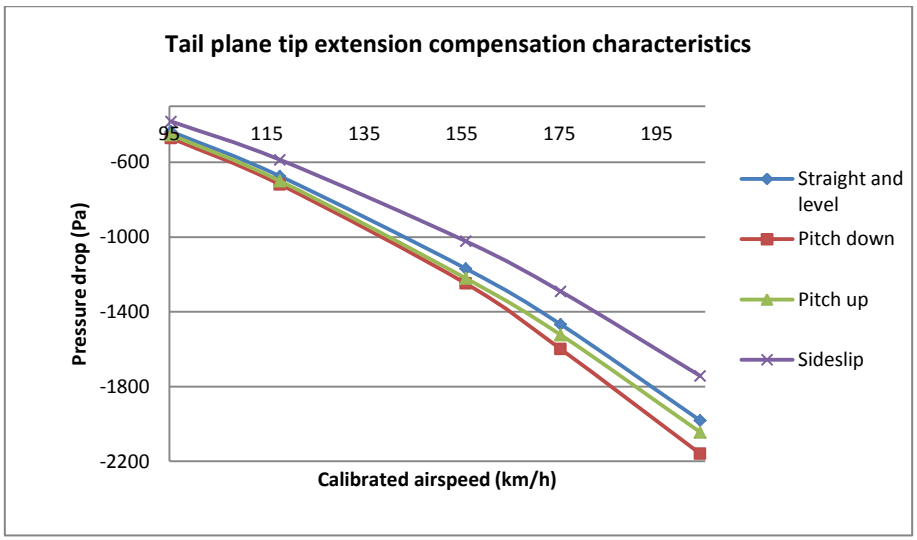

Figure 9-24: Compensation characteristics calculated using CFD for the tail plane tip extension

9.4.3 Discussion

The concept design induced slightly less drag and nearly recreated the same compensation characteristics as that of the current probe.

9.5 Concept design 4 – Tail plane tip bulge

The aim of the design is to further reduce the drag of the tail plane tip extension concept by redesigning the surface of the horizontal tail plane tip into a probe. The pressure difference between the top and bottom surfaces of the tail plane (paragraph 2.1.4) causes a probe designed close to the skin, such as those described in paragraph 2.4.4, to become significantly sensitive to changes in pitch. The tip was modified to create a base symmetric to the airflow for pitch insensitivity (Figure 9-26).

The base provides separation from the rest of the tail plane surfaces to prevent the unsymmetrical pressure distribution from affecting the probe measurements (Figure 9-25).

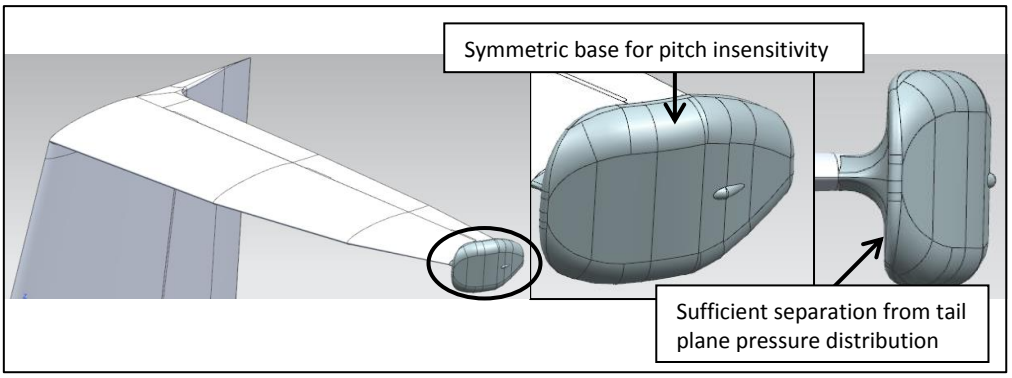

Figure 9-25: Tail plane tip bulge CAD model

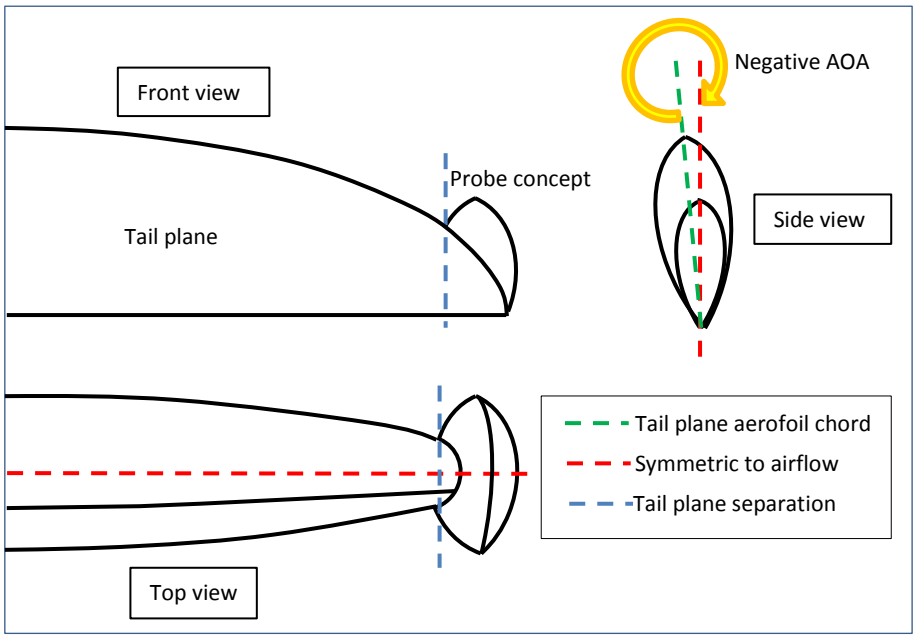

Figure 9-26: **Tail plane tip bulge principle**

9.5.1 Drag analysis

A CFD model was created to analyse the drag along the surface of the probe concept. The design created a large turbulent wake with a severe drag increase at the inner edges of the base (Figure 9-27).

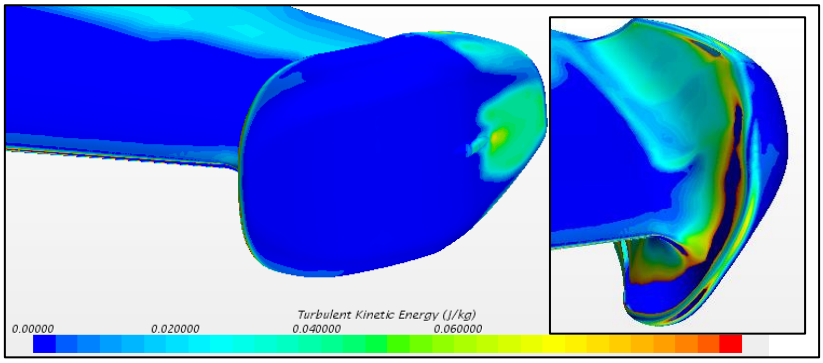

Figure 9-27: **Drag analysis of the tail plane tip bulge using CFD**

Table 9-5: **Drag calculated using CFD for the tail plane tip bulge**

CAS	Drag (N)			Difference from ideal JS-1C		Difference from current probe	
km/h	Ideal JS-1C	Current probe	Concept design 4	N	%	N	%
95	4.42	4.65	5.57	1.16	26.2	0.93	20.0
118	6.62	6.97	8.35	1.73	26.1	1.38	19.8
156	11.23	11.81	14.06	2.83	25.2	2.25	19.0
175	14.36	15.04	17.79	3.43	23.9	2.74	18.2
204	19.84	20.76	24.26	4.42	22.3	3.50	16.9

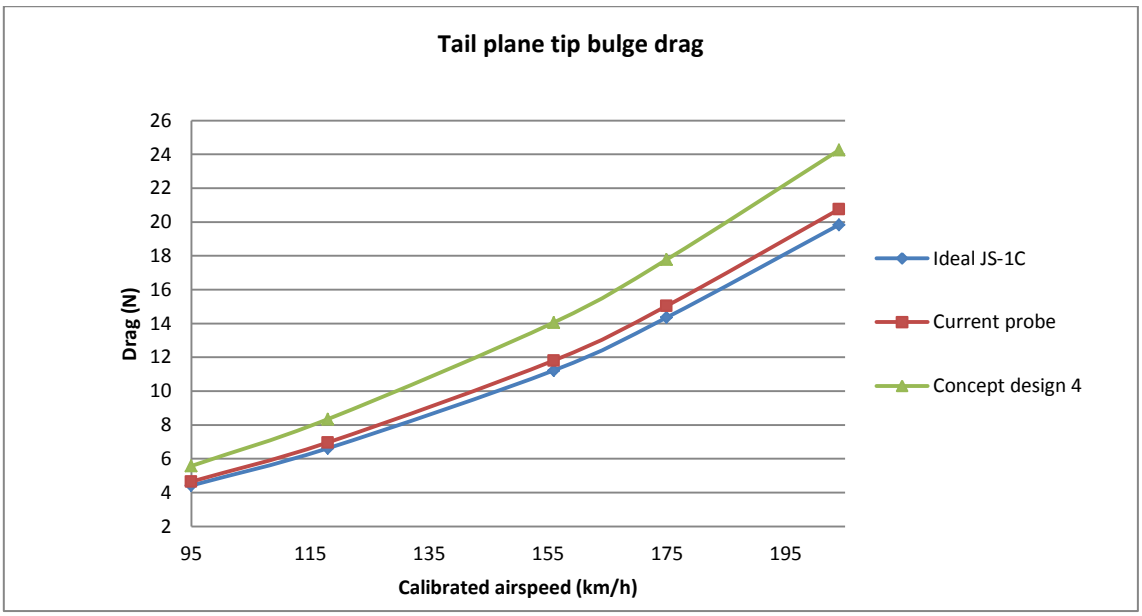

Figure 9-28: **Drag calculated using CFD for the tail plane tip bulge**

The average drag force increase was 25 % on the left side of the tail plane, which is five times that induced by the current probe (Table 9-5 and Figure 9-28).

9.5.2 Compensation characteristics analysis

A plane was created through the cross-section of the design to determine the area of lowest pressure where the probe opening was positioned (Figure 9-29).

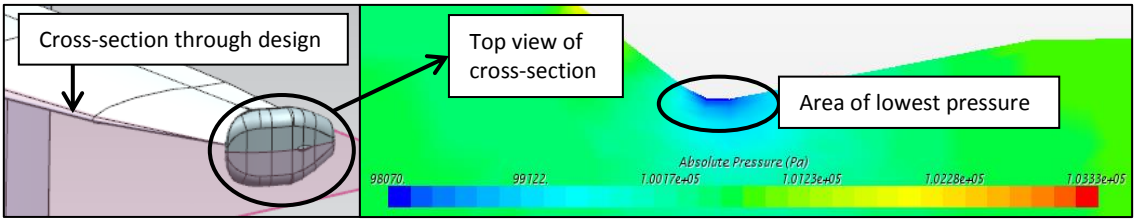

Figure 9-29: **Absolute pressure scalar plane created through the cross-section of the tail plane tip bulge**

The following data was calculated using CFD for straight and level flight (Table 9-6):

Table 9-6: **Pressure drop calculated for straight and level flight using CFD for the tail plane tip bulge**

Theoretical model			Current probe		Concept design 4	
CAS	Pressure drop	Cp	Pressure drop	Cp	Pressure drop	Cp
km/h	Pa	-	Pa	-	Pa	-
95	-446	-1.00	-334	-0.75	-406	-0.91
118	-679	-1.00	-526	-0.78	-633	-0.93
156	-1189	-1.00	-1020	-0.86	-1120	-0.94
175	-1505	-1.00	-1311	-0.87	-1417	-0.94
204	-2037	-1.00	-1834	-0.90	-1946	-0.96

The average pressure coefficient calculated was within the boundary between the theoretical model and current probe. The CFD model for straight and level flight was modified to simulate pitch and sideslip manoeuvres of 10° (Table 9-7).

Table 9-7: Pressure drop calculated during pitch and sideslip manoeuvres using CFD for the tail plane tip bulge

CAS	Straight and level	Pitch 10° down		Pitch 10° up		Sideslip 10°	
km/h	Pressure drop (Pa)	Pressure drop (Pa)	Difference (%)	Pressure drop (Pa)	Difference (%)	Pressure drop (Pa)	Difference (%)
95	-406	-499	22.9	-394	-3.0	-337	-16.9
118	-633	-777	22.8	-617	-2.4	-527	-16.8
156	-1120	-1377	22.9	-1099	-1.9	-933	-16.7
175	-1417	-1734	22.4	-1375	-3.0	-1182	-16.6
204	-1946	-2374	22.0	-1891	-2.9	-1615	-17.0

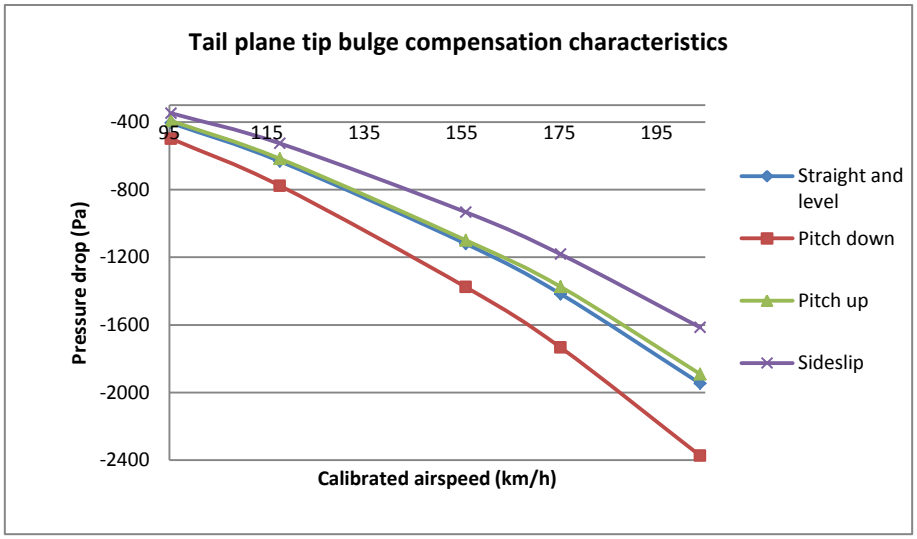

Figure 9-30: Compensation characteristics calculated using CFD for the tail plane tip bulge

The design has nearly the same compensation characteristics as the current probe during a climb with an average pressure drop change calculated as 3 %, but is much more sensitive during a dive with 23 % (Figure 9-30). The change in sideslip was slightly worse than the current probe with 16 %.

9.5.3 Discussion

A large base is required to reduce the sensitivity of the probe to pitch manoeuvres due to the pressure distribution on the surfaces of the tail plane. However, the larger the base becomes to reduce manoeuvre sensitivity the more drag the design induces. The attempts made to keep the design symmetric to the airflow did not promote uniform sensitivity during pitch manoeuvres.

9.6 Discussion

The relocation of the current probe caused a significant decrease in the size of the turbulent wake when compared to the current probe position. However, the turbulent wake is not a representation of the drag force; the size of the turbulent wake is smaller than that of the current probe, but the drag force is greater.

The probe causes a significant drag increase on the tip of the tail plane and, combined with the minor influence the probe has over a large surface area of the tail plane, caused an undesired drag increase greater than that of the current probe. The influence of the probe on the surfaces of the tail plane was restricted when positioned even closer to the tip and the probe length shortened.

A probe designed as part of the tail plane skin is much more complex, where the unequal pressure distribution between the top and bottom surface causes large pressure drop changes during different manoeuvres. Significant design changes would have to be made to the tail plane to create a stable base for the probe instead of creating a large separate base that induces more drag than the current probe.

9.7 Conclusion

The total energy probe was moved to the tip of the horizontal tail plane, where concept designs were also applied to reduce the unexpected high drag experienced.

The total energy probe moved to the tip of the horizontal tail plane did not significantly reduce the drag compared to that of the current probe location. However, the relocation and modification of the probe for the very tip of the tail plane (paragraph 9.4) as a minor extension from the tip surface could prove significant for its simplicity. Though the drag was not significantly reduced as in the mild fin protrusion concept in paragraph 8.2, the drag was still 12 % less than that induced by the current total energy probe.

The current total energy probe was relocated to the nose of the sailplane on the fuselage to determine whether moving the probe to a surface mostly subjected to laminar flow would cause a significant drag increase.

CHAPTER 10: RELOCATION OF THE TOTAL ENERGY PROBE TO THE FUSELAGE

The current total energy probe was relocated to the nose of the fuselage. The aim was to determine whether moving the probe to a surface mostly subjected to laminar flow would cause a significant drag increase.

10.1 Drag analysis

The current probe was relocated to the nose of the fuselage (Figure 10-1) and the drag thereof compared to a baseline created for the fuselage section of the sailplane (Figure 10-2).

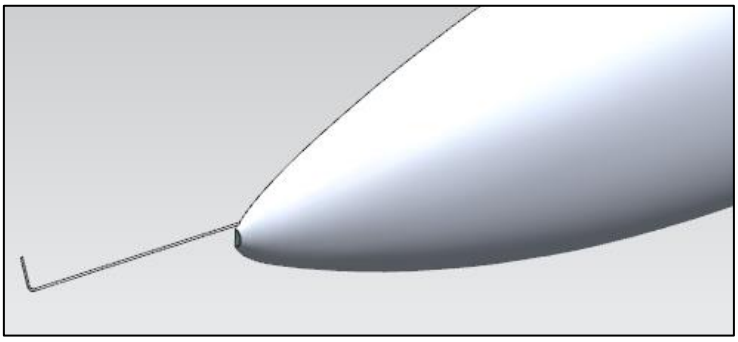

Figure 10-1: **Fuselage nose probe**

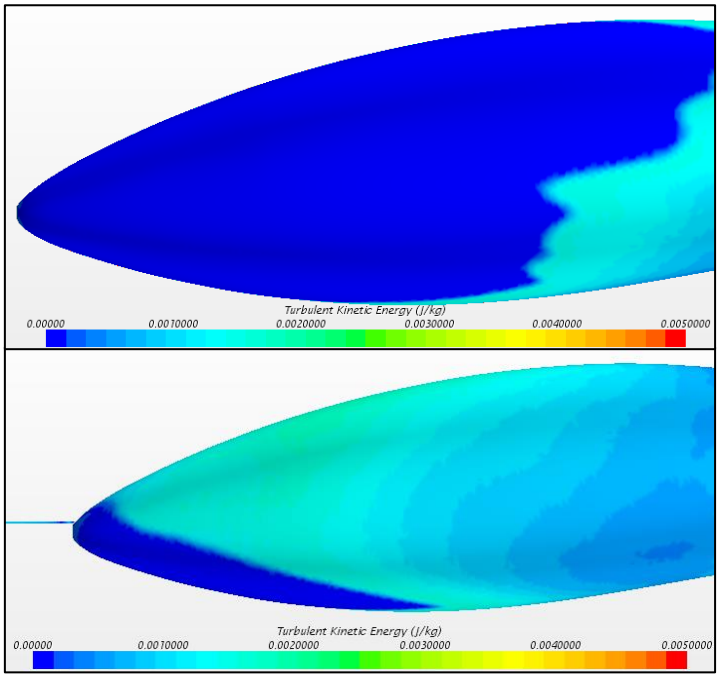

Figure 10-2: **External airflow of the fuselage nose probe (bottom) compared to the fuselage baseline (top)**

The probe created a turbulent wake over nearly the entire fuselage section. Due to the mostly laminar boundary layer present over the fuselage, the total energy probe caused the layer to prematurely transition to turbulent.

Table 10-1: Drag calculated using CFD for the fuselage nose probe

CAS	Drag (N)		Difference from ideal JS-1C	
km/h	Ideal JS-1C	Fuselage nose probe	N	%
95	19.13	22.36	3.23	16.9
118	31.77	35.07	3.29	10.4
156	55.47	62.01	6.55	11.8
175	74.93	78.40	3.47	4.6
204	102.66	107.22	4.56	4.4

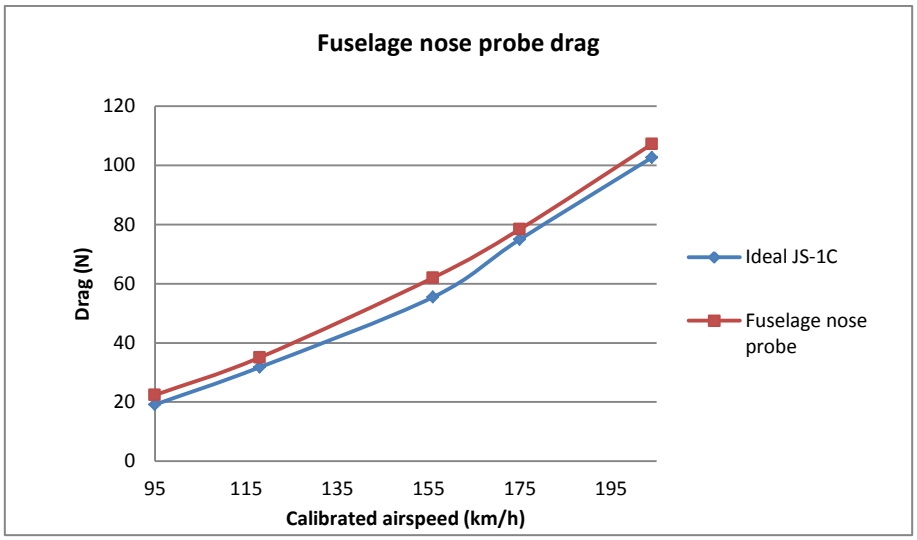

Figure 10-3: Drag calculated using CFD for the fuselage nose probe

An average drag force increase of 9.6 % was calculated on the left surface of the fuselage section, which is nearly twice that induced by the current probe (Table 10-1 and Figure 10-3).

10.2 Compensation characteristics

The relocation of the current probe to the nose of the fuselage should not influence the compensation characteristics thereof, as with the tail plane tip probe in paragraph 9.3. Based on the data collected for the total energy probe relocated to the nose of the fuselage, concept designs were created by modifying the fuselage nose probe and redesigning the probe for the fuselage skin (continued from the concept designs described in paragraph 9.4 and 9.5).

10.3 Concept design 5 – Fuselage nose extension

The aim of the design is to redesign the fuselage nose probe to determine whether the drag in paragraph 10.1 could be reduced (Figure 10-4).

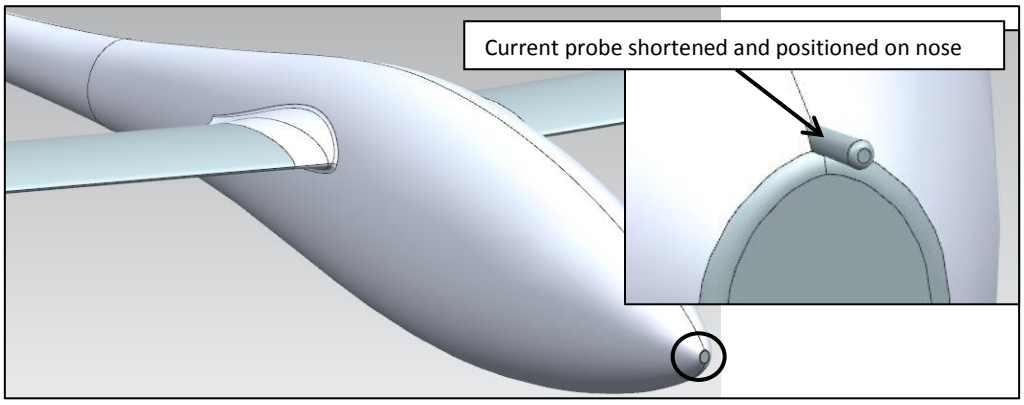

Figure 10-4: **Fuselage nose extension CAD model**

The current probe length was shortened to prevent damage to the probe during an aero tow (paragraph 2.6).

10.3.1 Drag analysis

The baseline for the fuselage section created in paragraph 10.1 was compared to the concept design (Figure 10-5). The turbulent wake of the concept design was nearly the same as the fuselage section baseline and the average drag force increase on the left surface of the fuselage was 37 % (Table 10-2).

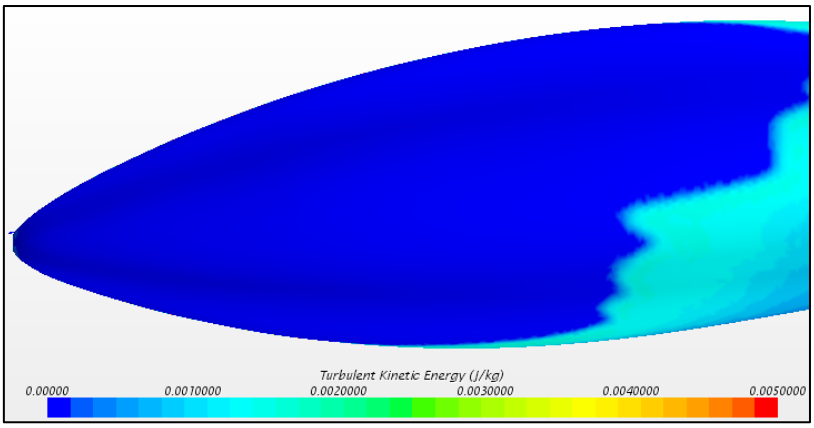

Figure 10-5: **Drag analysis of the fuselage nose extension using CFD**

Table 10-2: **Drag calculated using CFD for the fuselage nose extension**

CAS	Drag (N)		Difference from ideal JS-1C	
km/h	Ideal JS-1C	Concept design 5	N	%
95	19.13	23.47	4.33	22.7
118	31.77	38.83	7.05	22.2
156	55.47	80.25	24.78	44.7
175	74.93	108.64	33.70	45.0
204	102.66	151.96	49.30	48.0

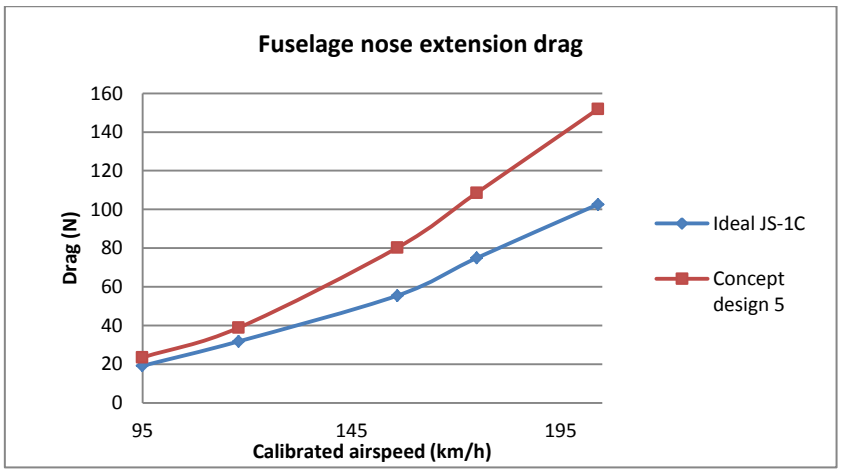

Figure 10-6: **Drag calculated using CFD for the fuselage nose extension**

This is a significant increase compared to merely moving the current probe in paragraph 10.1 (Figure 10-6).

10.3.2 Compensation characteristics analysis

A plane was created through the cross-section of the design to show the area where the probe opening was positioned (Figure 10-7). Since the probe opening is not positioned to create a vacuum or negative pressure, the opening was positioned in an area of high pressure with equal magnitude.

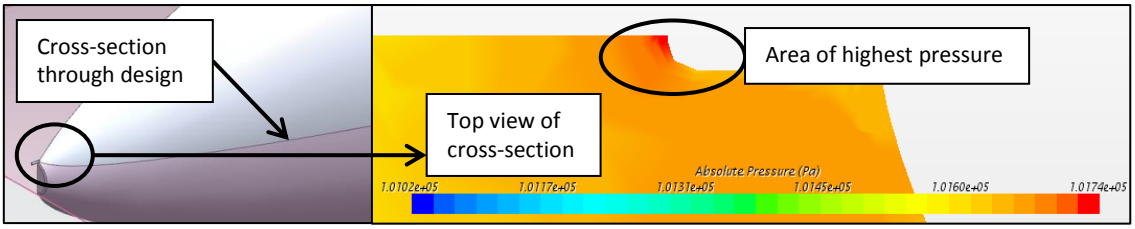

Figure 10-7: **Absolute pressure scalar plane created through the cross-section of the fuselage nose extension**

The following data was calculated using CFD for straight and level flight (Table 10-3):

Table 10-3: **Pressure drop calculated for straight and level flight using CFD for the fuselage nose extension**

Theoretical model			Current probe		Concept design 5	
CAS	Pressure drop	Cp	Pressure drop	Cp	Pressure drop	Cp
km/h	Pa	-	Pa	-	Pa	-
95	-446	-1.00	-334	-0.75	433	0.97
118	-679	-1.00	-526	-0.78	669	0.99
156	-1189	-1.00	-1020	-0.86	1169	0.98
175	-1505	-1.00	-1311	-0.87	1471	0.98
204	-2037	-1.00	-1834	-0.90	2001	0.98

The average pressure coefficient calculated was within the boundary between the theoretical model and current probe of 1.00 and 0.83 respectively for a positive pressure of equal magnitude. The CFD model for straight and level flight was modified to simulate pitch and sideslip manoeuvres of 10° (Table 10-4).

Table 10-4: Pressure drop calculated during pitch and sideslip manoeuvres using CFD for the fuselage nose extension

CAS	Straight and level	Pitch 10° down		Pitch 10° up		Sideslip 10°	
km/h	Pressure drop (Pa)	Pressure drop (Pa)	Difference (%)	Pressure drop (Pa)	Difference (%)	Pressure drop (Pa)	Difference (%)
95	433	437	1.0	358	-17.3	396	-8.5
118	669	675	0.9	552	-17.4	612	-8.5
156	1169	1180	0.9	965	-17.5	1070	-8.5
175	1471	1486	1.0	1215	-17.4	1347	-8.5
204	2001	2018	0.9	1649	-17.6	1829	-8.6

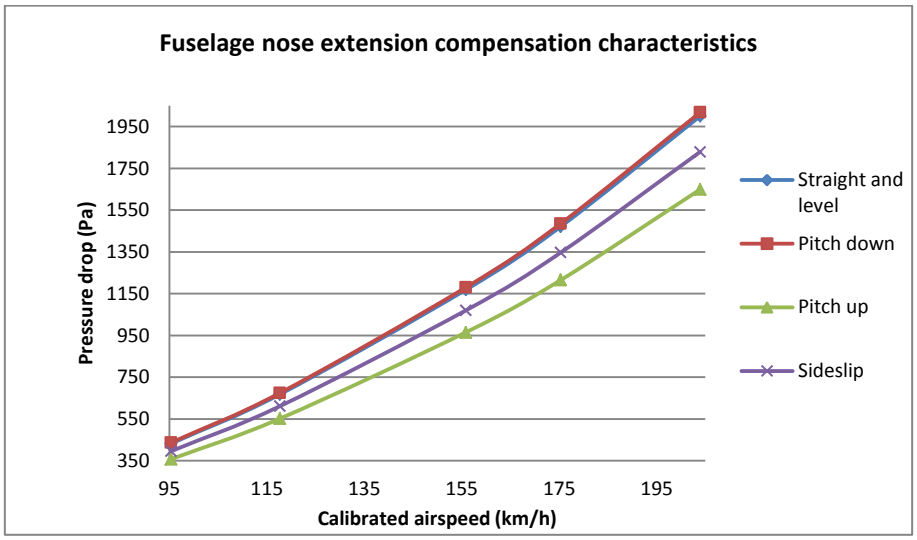

Figure 10-8: Pressure drop calculated during pitch and sideslip manoeuvres using CFD for the fuselage nose extension

The average pressure drop change is almost the same as the mild fin protrusion concept, where the climb is slightly worse with 17 % and the sideslip improved greatly with 8 % (Figure 10-8).

10.3.3 Discussion

The design caused a significant drag increase on the fuselage surface compared to merely moving the current total energy probe. There is a slight velocity increase in the airflow over the bottom surface of the fuselage with differences in the airflow observed where the probe is positioned (Figure 10-9). Cross-section planes were created on the fuselage baseline and concept design to study the effect of the probe on the airflow over the surfaces of the fuselage (Figure 10-10).

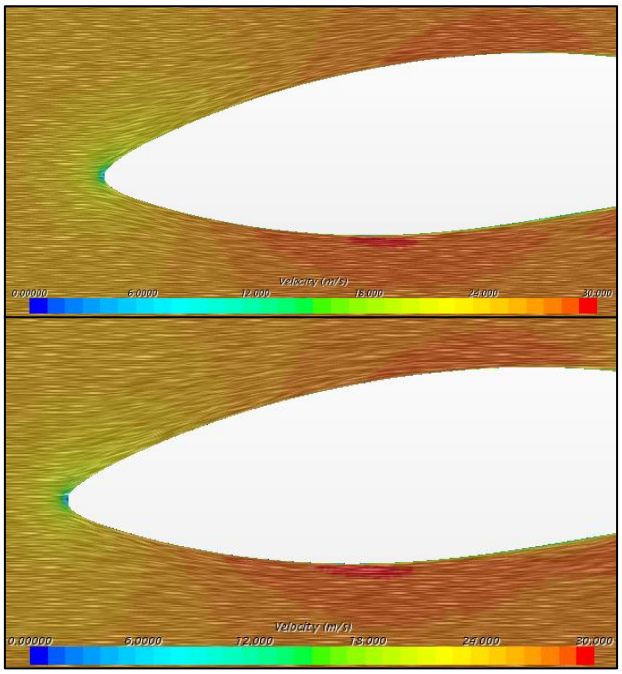

Figure 10-9: **Velocity vector plane created through the fuselage baseline (top) and fuselage nose extension (bottom) CFD**

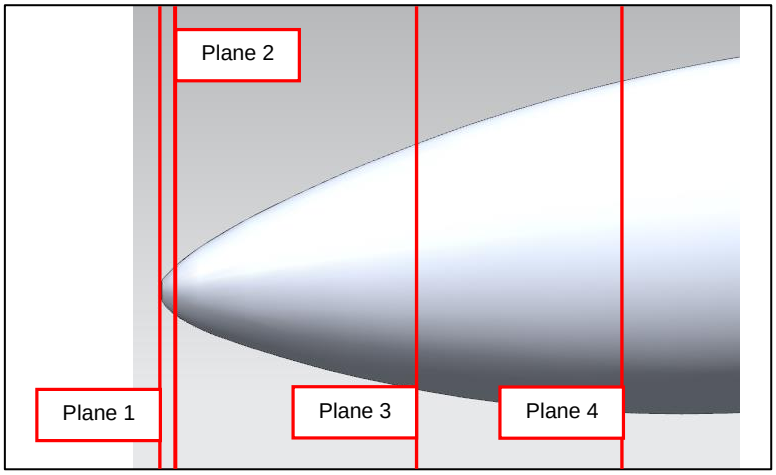

Figure 10-10: **Cross-section planes created through the CFD of the fuselage nose extension**

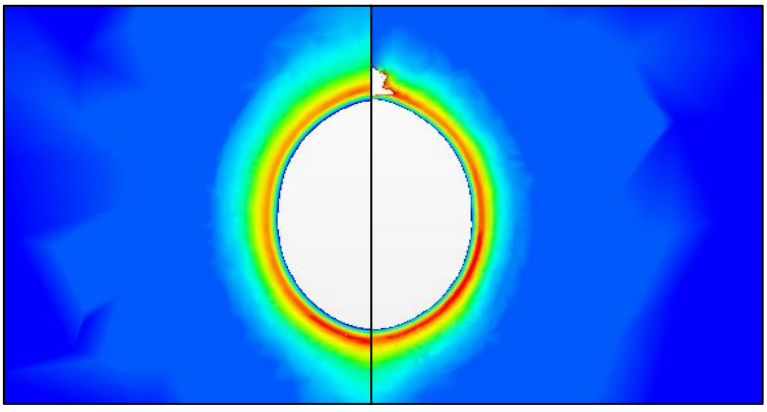

Figure 10-11: **Turbulent kinetic energy scalar plane 1 created through the fuselage baseline (left) and fuselage nose extension (right) CFD**

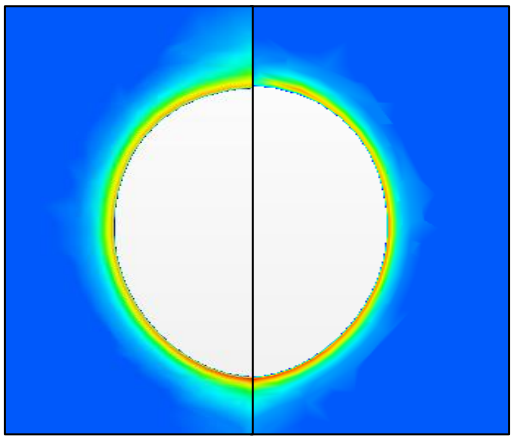

Figure 10-12: **Turbulent kinetic energy scalar plane 2 created through the fuselage baseline (left) and fuselage nose extension (right) CFD**

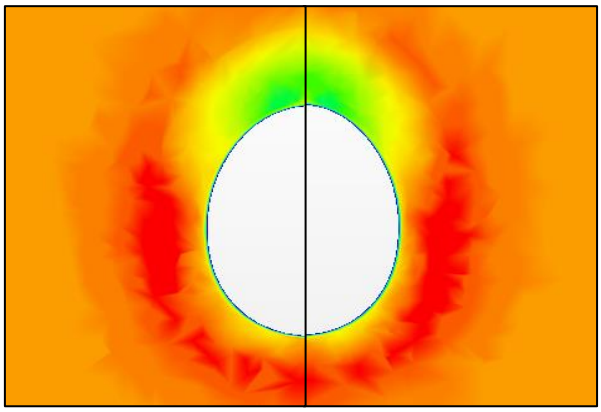

Figure 10-13: **Turbulent kinetic energy scalar plane 3 created through the fuselage baseline (left) and fuselage nose extension (right) CFD**

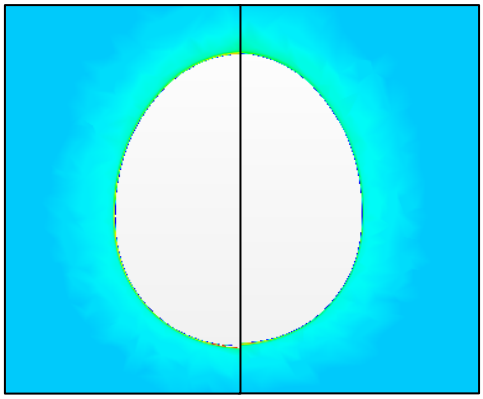

Figure 10-14: **Turbulent kinetic energy scalar plane 4 created through the fuselage baseline (left) and fuselage nose extension (right) CFD**

As with the tail plane tip probe in paragraph 9.2, the combination of small changes over a large surface area with the significant changes at the probe position causes the drag to increase significantly (Figure 10-11 to Figure 10-14).

10.4 Concept design 6 – Fuselage protrusion

The aim of the design is to improve the fuselage nose extension concept by redesigning the probe as a protrusion on the fuselage skin, such as that of Hugh Kendall (Figure 10-15).

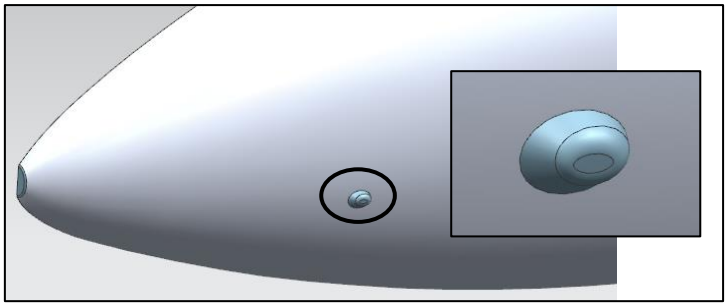

Figure 10-15: **Fuselage protrusion CAD model**

10.4.1 Drag analysis

The baseline created for the fuselage section was compared to the concept design (Figure 10-16) and the average drag force increase on the left surface of the fuselage was calculated as 0.8 % (Table 10-5).

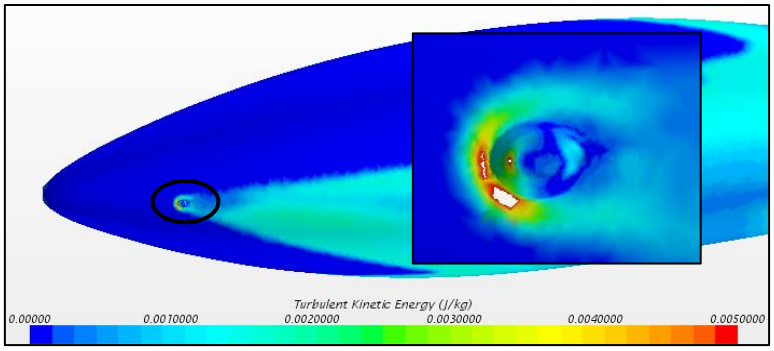

Figure 10-16: **Drag analysis of the fuselage protrusion using CFD**

Table 10-5: **Drag calculated using CFD for the fuselage protrusion**

CAS	Drag (N)		Difference from ideal JS-1C	
km/h	Ideal JS-1C	Concept design 6	N	%
95	19.13	19.39	0.26	1.4
118	31.77	31.79	0.01	0.0
156	55.08	55.47	0.39	0.7
175	74.87	73.93	1.07	1.4
204	102.11	102.66	0.55	0.5

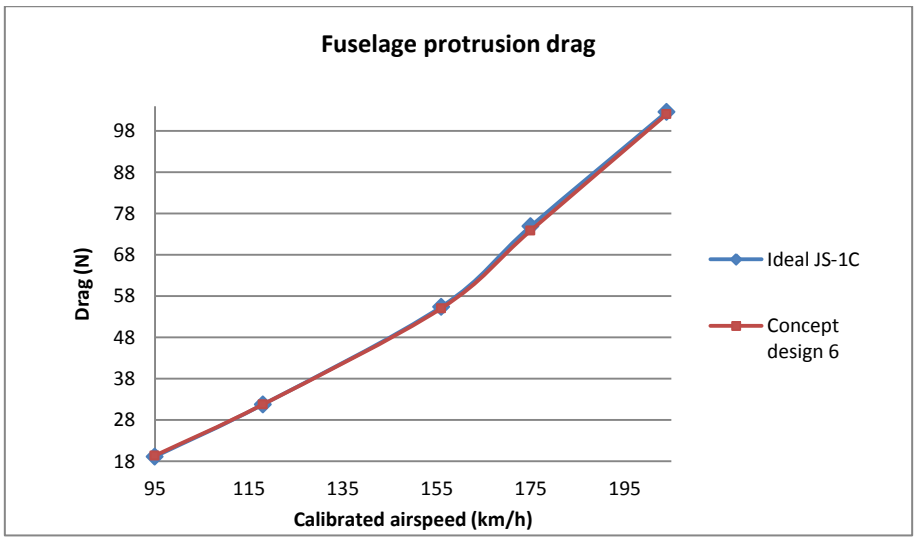

Figure 10-17: **Drag calculated using CFD for the fuselage protrusion**

This is a significant improvement compared to the fuselage nose extension (Figure 10-17).

10.4.2 Compensation characteristics analysis

A plane was created through the cross-section of the design to determine the area of lowest pressure where the probe opening was positioned (Figure 10-18).

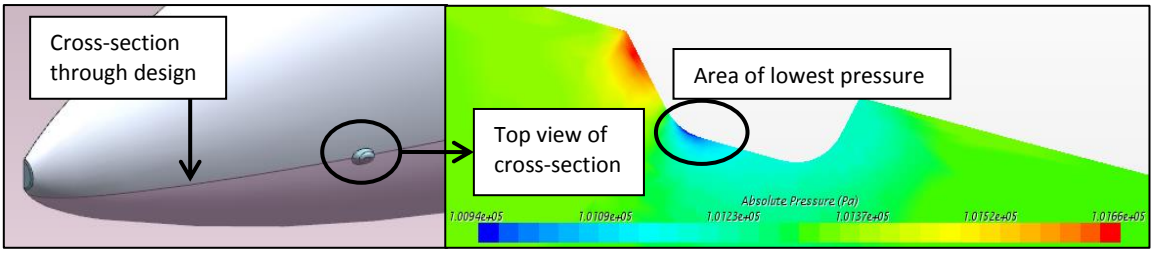

Figure 10-18: **Absolute pressure scalar plane created through the cross-section of the fuselage protrusion**

The following data was calculated using CFD for straight and level flight (Table 10-6):

Table 10-6: **Pressure drop calculated for straight and level flight using CFD for the fuselage protrusion**

Theoretical model			Current probe		Concept design 6	
CAS	Pressure drop	Cp	Pressure drop	Cp	Pressure drop	Cp
km/h	Pa	-	Pa	-	Pa	-
95	-446	-1.00	-334	-0.75	-397	-0.89
118	-679	-1.00	-526	-0.78	-621	-0.92
156	-1189	-1.00	-1020	-0.86	-1105	-0.93
175	-1505	-1.00	-1311	-0.87	-1397	-0.93
204	-2037	-1.00	-1834	-0.90	-1915	-0.94

The average pressure coefficient calculated was within the boundary between the theoretical model and current probe. The CFD model for straight and level flight was modified to simulate pitch and sideslip manoeuvres of 10° (Table 10-7).

Table 10-7: Pressure drop calculated during pitch and sideslip manoeuvres using CFD for the fuselage protrusion

CAS	Straight and level	Pitch 10° down		Pitch 10° up		Sideslip 10°	
km/h	Pressure drop (Pa)	Pressure drop (Pa)	Difference (%)	Pressure drop (Pa)	Difference (%)	Pressure drop (Pa)	Difference (%)
95	-397	-514	29.6	-410	3.5	-383	-3.3
118	-621	-803	29.2	-644	3.6	-601	-3.3
156	-1105	-1430	29.4	-1143	3.4	-1041	-5.9
175	-1397	-1813	29.8	-1448	3.6	-1318	-5.7
204	-1915	-2488	30.0	-1984	3.6	-1796	-6.2

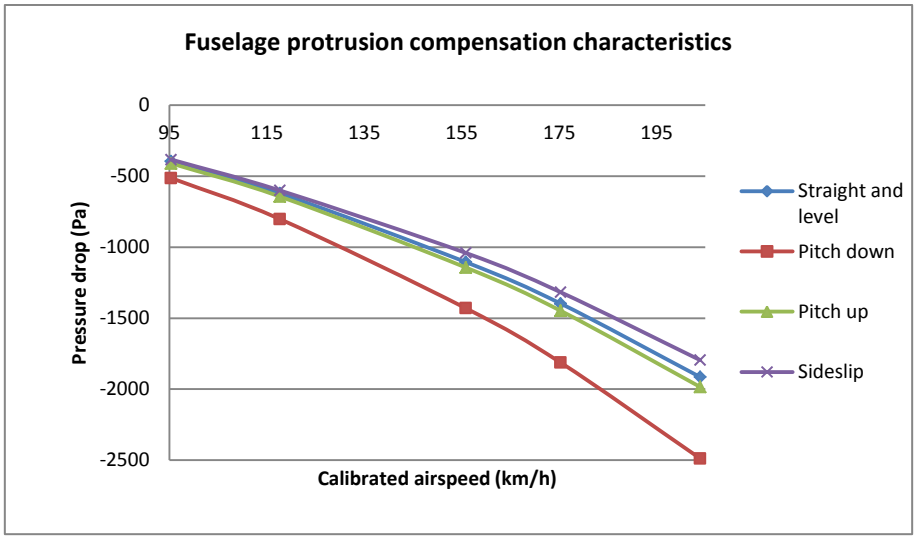

Figure 10-19: Pressure drop calculated during pitch and sideslip manoeuvres using CFD for the fuselage protrusion

The average pressure drop change during a dive was significantly worse than the fuselage nose extension with 30 %, but better during climb and sideslip with 4 % and 5 % respectively (Figure 10-19).

10.4.3 Discussion

The design requires further improvement to reduce its significant sensitivity during dive manoeuvres and ensure uniform average pressure drop changes during pitch manoeuvres.

10.5 Discussion

The relocation of the current probe to the nose of the fuselage induced nearly twice the drag of that induced by the current total energy probe, but reducing the length thereof (fuselage nose

extension) caused a further significant drag increase. The small changes in the airflow over a large area, along with the significant changes at the probe location, caused the drag to increase as with the tail plane tip probe in paragraph 9.2.3. The design of total energy probe protrusions on the sides of the fuselage skin is beneficial to drag reduction, but the elliptic shape of the fuselage makes it difficult to achieve uniform average pressure drop changes during pitch manoeuvres.

10.6 Conclusion

The total energy probe was moved to the nose of the fuselage and concept designs were applied to reduce the significant drag increase.

The fuselage protrusion concept requires further design refinement to improve climb and sideslip manoeuvre insensitivity to benefit from the low drag induced. The design could greatly benefit the JS-1C, as demonstrated by the total energy blister design by Hugh Kendall (paragraph 2.4.4).

The other external sensors that can be installed onto the JS-1C were evaluated, including the possibility of replacing all external sensors with a single probe.

CHAPTER 11: EXTERNAL SENSORS

The JS-1C sailplane has two external sensors, namely the total energy probe and the pitot-static probe. There is also an optional sensor called a multi probe that replaces both probes and measures total, static and dynamic pressure.

11.1 Pitot-static probe

A sailplane requires a pitot-static probe to operate the airspeed indicator and altimeter of the sailplane during flight, which are compulsory instruments. The pitot-static probe of the JS-1C is also positioned on the vertical tail fin in the same area as the current total energy probe. The installation of the pitot-static and total energy probes separately (Figure 11-1) causes an estimated average drag increase of 5.3 % on the left surface of the fin (Figure 11-2).

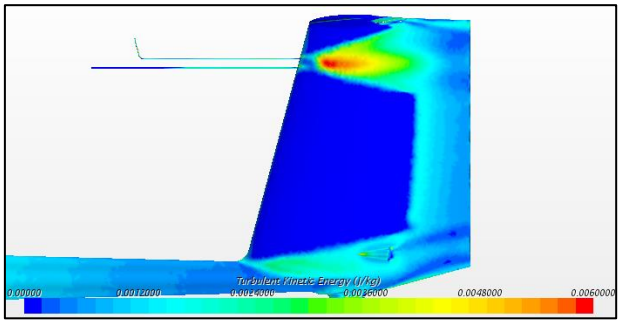

Figure 11-1: **Drag analysis of the pitot-static and total energy probes at the current probe position**

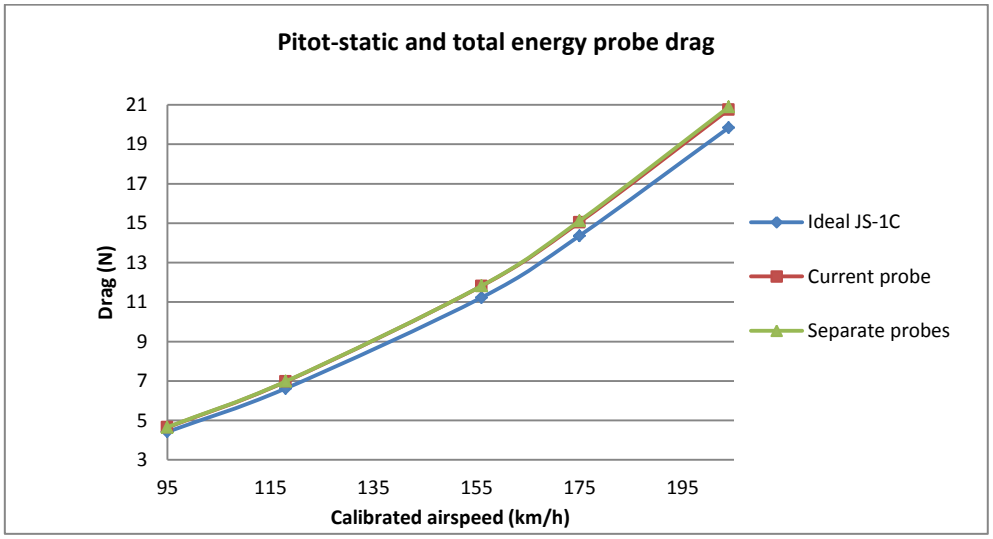

Figure 11-2: **Drag calculated using CFD for the pitot-static and total energy probes at the current probe position**

The pitot-static probe positioned alone at the current total energy probe position (Figure 11-3) would cause an estimated average drag increase of 1.3 % on the left surface of the fin (Figure 11-4).

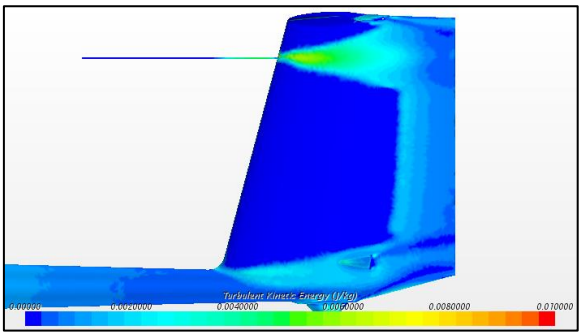

Figure 11-3: **Drag analysis of the pitot-static probe at the current total energy probe position**

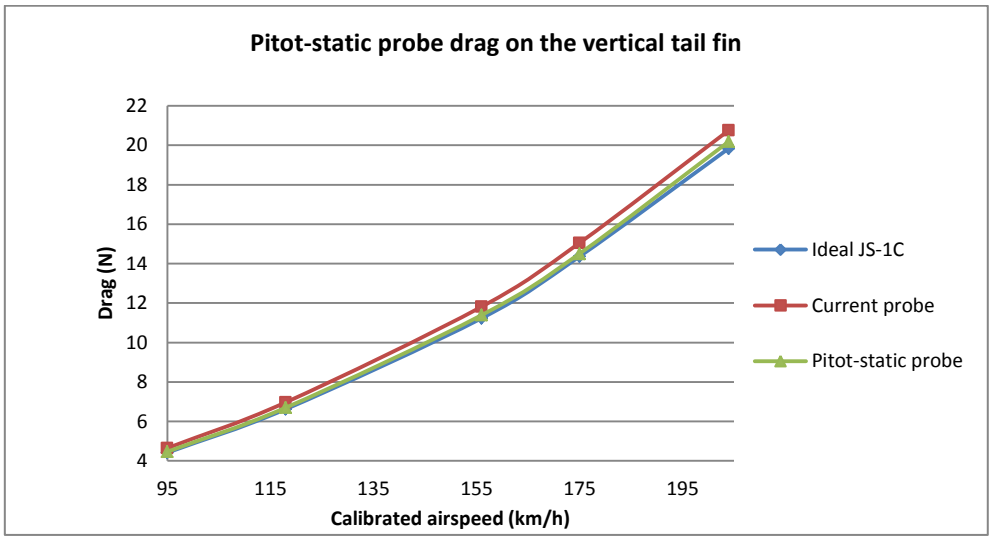

Figure 11-4: **Drag calculated using CFD for the pitot-static probe at the current total energy probe position**

The pitot-static probe positioned on the left tip of the horizontal tail plane (Figure 11-5) would cause an estimated average drag increase of only 0.5 % (Figure 11-6).

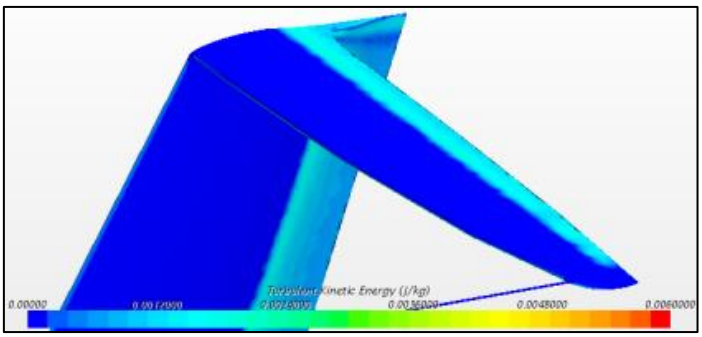

Figure 11-5: **Drag analysis of the pitot-static probe at the horizontal tail plane tip**

The pitot-static probe itself induces significantly less drag than the current total energy probe.

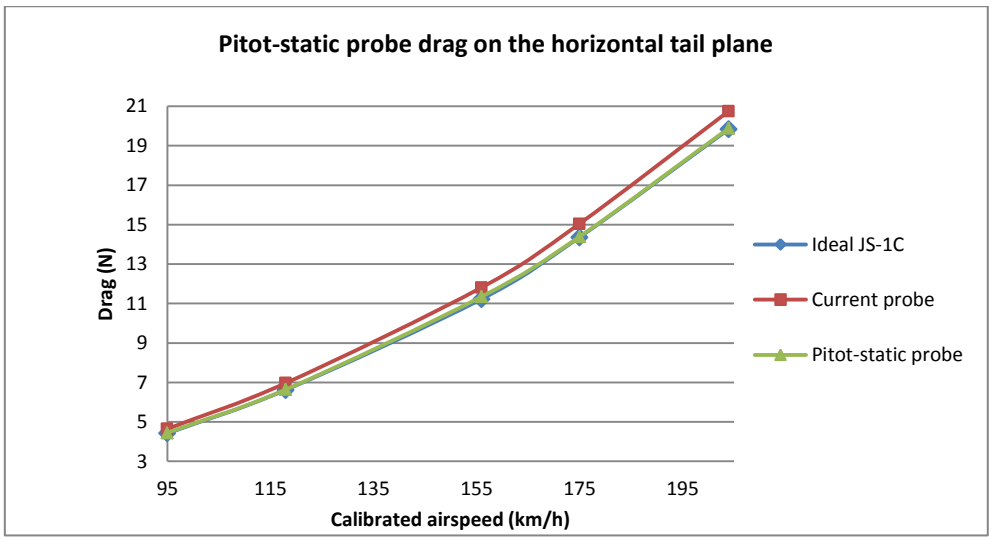

Figure 11-6: Drag calculated using CFD for the pitot-static probe at the horizontal tail plane tip

A drag analysis was conducted on the multi probe to determine whether a single probe would induce less drag than installing both probes separately.

11.2 Multi probe

Clients can choose whether to install the total energy and pitot-static probes separately or to replace both probes with a single multi probe (Figure 11-7).

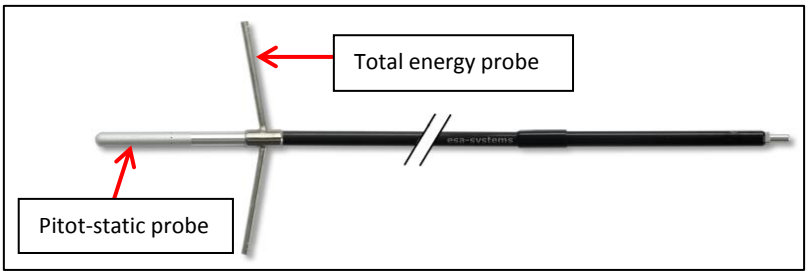

Figure 11-7: Type DN/3-fach/UN multi probe (esa systems, 2016)

A multi probe installed at the current total energy probe position (Figure 11-8) would cause an estimated average drag increase of 7.3 % on the left surface of the fin (Figure 11-9).

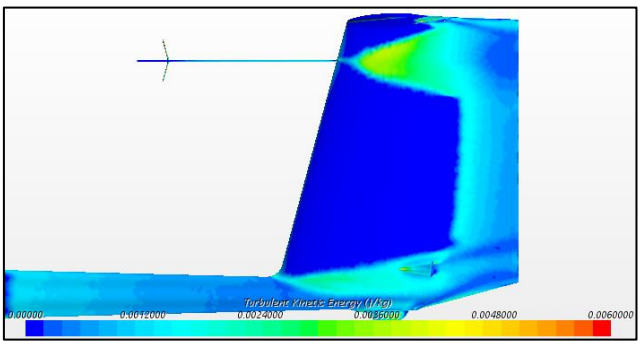

Figure 11-8: Drag analysis of the multi probe at the current total energy probe position

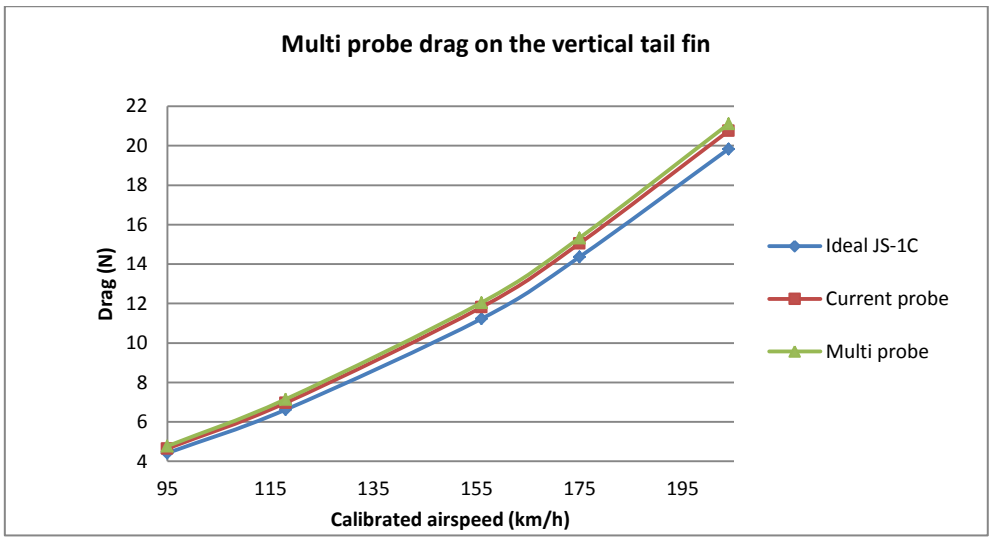

Figure 11-9: **Drag calculated using CFD for the multi probe at the current total energy probe position**

A multi probe installed on the left tip of the horizontal tail plane (Figure 11-10) would cause an estimated average drag increase of 10.1 % (Figure 11-11).

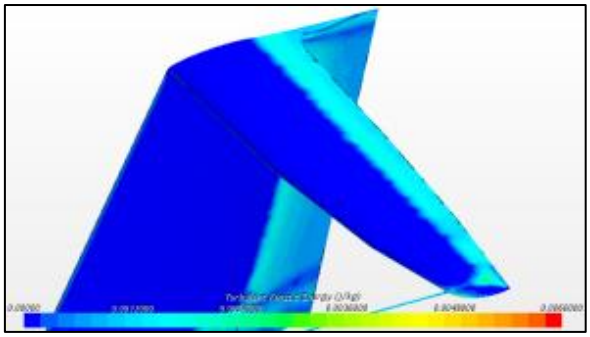

Figure 11-10: **Drag analysis of the multi probe at the horizontal tail plane tip**

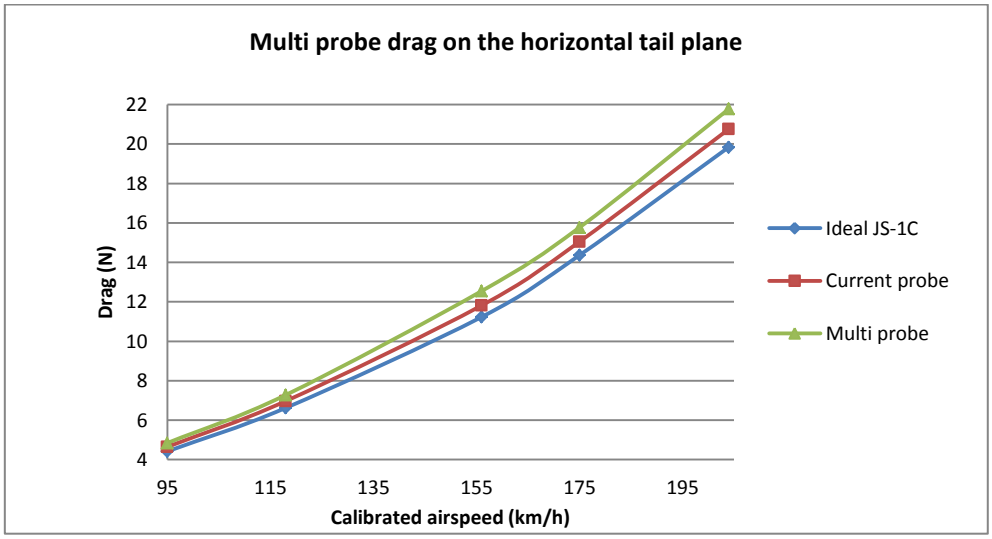

Figure 11-11: **Drag calculated using CFD for the multi probe at the horizontal tail plane tip**

The multi probe induced more drag than the current total energy probe.

11.3 Discussion

The multi probe, though more convenient than two separate probes, induced more drag than the current total energy probe (Table 11-1).

Table 11-1: Estimated total drag of different probe placement combinations

Total drag increase on the JS-1C tail section (%)								
Probe	Placement	Configuration	CAS					Average
			95 km/h	118 km/h	156 km/h	175 km/h	204 km/h	
None	-	-	0.0	0.0	0.0	0.0	0.0	**0.0**
Total energy probe	Fin	Up	10.4	10.4	10.4	9.6	9.2	**10.0**
		Down	10.8	10.3	12.1	10.9	9.3	**10.7**
	Fin shift	Up	9.7	9.7	11.7	10.0	8.8	**10.0**
		Down	10.8	10.8	11.8	11.2	9.9	**10.9**
	Tail plane centre	Up	6.3	5.9	7.7	4.3	9.4	**6.7**
		Down	6.8	7.9	9.0	9.9	9.9	**8.7**
	Tail plane tip	Up	8.0	8.1	8.5	7.3	7.5	**7.8**
		Down	5.8	5.4	7.1	6.1	6.2	**6.1**
Multi probe	Fin	Vertical	15.9	16.0	14.6	13.5	12.8	**14.6**
		Horizontal	15.3	15.3	16.7	13.3	14.0	**14.9**
	Fin shift	Vertical	14.2	14.8	16.9	13.8	13.5	**14.6**
		Horizontal	13.5	13.5	15.7	15.0	13.3	**14.2**
	Tail plane centre	Vertical	11.8	12.0	13.3	11.7	13.8	**12.5**
		Horizontal	11.0	11.8	13.6	15.6	15.1	**13.4**
	Tail plane tip	Vertical	9.6	9.9	11.7	9.8	9.7	**10.1**
		Horizontal	10.5	10.4	11.9	10.9	10.2	**10.8**
Pitot-static probe	Fin	-	2.2	2.3	2.9	2.0	3.5	**2.6**
	Fin shift	-	2.6	1.8	3.6	1.2	4.3	**2.7**
	Tail plane centre	-	1.2	1.4	1.8	1.4	2.5	**1.7**
	Tail plane tip	-	0.7	0.3	1.1	0.2	0.2	**0.5**

Placement:	Fin	Current position on fin leading edge
	Fin shift	Position on fin leading edge halfway between current position and tail plane centre
	Tail plane centre	Centre of tail plane where tail plane and fin leading edges intersect
	Tail plane tip	Left or right tip of tail plane
Configuration:	Up	Extension of probe directed upwards
	Down	Extension of probe directed downwards
	Vertical	Probe extensions are vertically aligned
	Horizontal	Probe extensions are horizontally aligned

The pitot-static probe itself induced so little drag that priority was given to selecting the most optimum total energy probe design or position to promote drag reduction.

11.4 Conclusion

The external sensors that can be installed on the JS-1C, besides the total energy probe, were evaluated and the possibility of replacing all external sensors with a single probe was discussed.

The multi probe alone induced more drag than installing the pitot-static probe and total energy probe separately. The installation of the probes separately induces significantly less drag than the current probe when each is installed at their most optimum position on the sailplane.

The manufacturability of the total energy probe configurations and designs was discussed according to the complexity thereof and the labour required.

CHAPTER 12: MANUFACTURABILITY

The manufacturability and incorporation of the total energy probe design into the manufacturing of the JS-1C sailplane is important, as the capabilities of the probes rely heavily on their orientation to the surfaces of the part to which they were designed for and applied to (for example paragraph 9.3 and 10.2).

If the probe design that induces the least drag requires significant changes to existing tooling that could damage the tools and diminish part surfaces, than it would be better to consider the second best design that requires less significant changes with fewer risks. The manufacturability of the total energy probe designs was divided into three categories, namely a mould modification, mould insert and a separate part (Table 12-1).

Table 12-1: Concept designs categorised according to manufacturability

	Manufacturability		
Probe configuration	Mould modification	Mould insert	Separate part
Tail plane tip probe	X		
Fuselage nose probe	X		
Prominent fin protrusion		X	X
Mild fin protrusion		X	X
Tail plane tip extension	X		
Tail plane tip bulge		X	X
Fuselage nose extension	X		
Fuselage protrusion		X	X

The labour required and risks regarding each manufacturing method were discussed.

12.1 Mould modification

A mould modification requires a slight change made to the mould where the total energy probe design is applied to (Figure 12-1). The area on the mould where the total energy probe adapter is positioned, which will hold the total energy probe in place during flight, is carefully removed and the affected surfaces of the mould refinished (Figure 12-2).

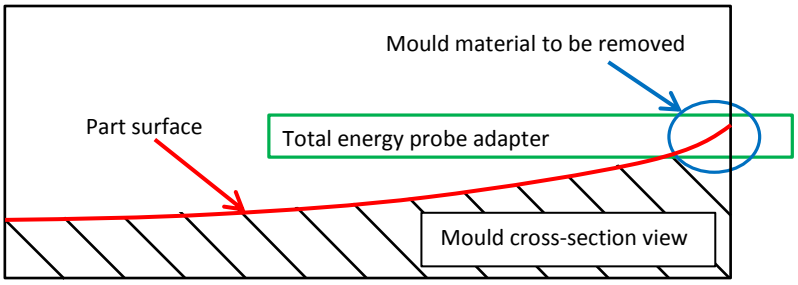

Figure 12-1: Small area on the mould removed to make space for the placement of the total energy probe adapter during part manufacturing

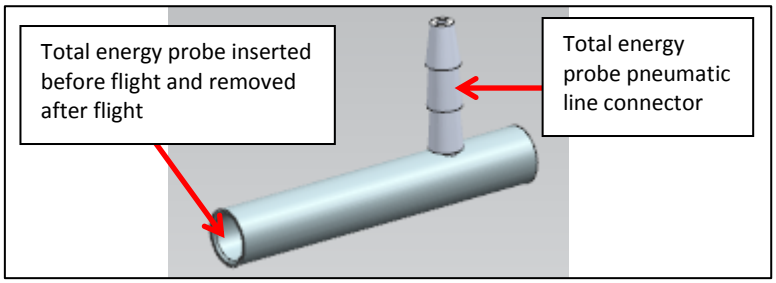

Figure 12-2: **Total energy probe adapter to be permanently bonded into the sailplane**

Tooling is then designed to hold the total energy probe adapter in place during the skin building process of the part. The risks regarding this manufacturing method is minimal if great care is taken when removing the mould surface area, where little mould surface refinishing or repair is required.

12.2 Mould insert

A mould insert requires a significant change to the surfaces of the mould of the part where the total energy probe design is applied to (Figure 12-3). These significant changes include (1) cutting away the surface of the mould where the probe is positioned, (2) manufacturing a total energy probe mould insert to replace the removed surface area, (3) manufacturing tooling to ensure the mould insert is bonded correctly to the rest of the mould and (4) refinishing or repair of the mould surface to ensure an acceptable out-of-mould surface finish. Modifications made to the surfaces of a mould reduce its part output or manufacturing life with the risk of producing parts with a poor surface quality that require additional time and resources to correct.

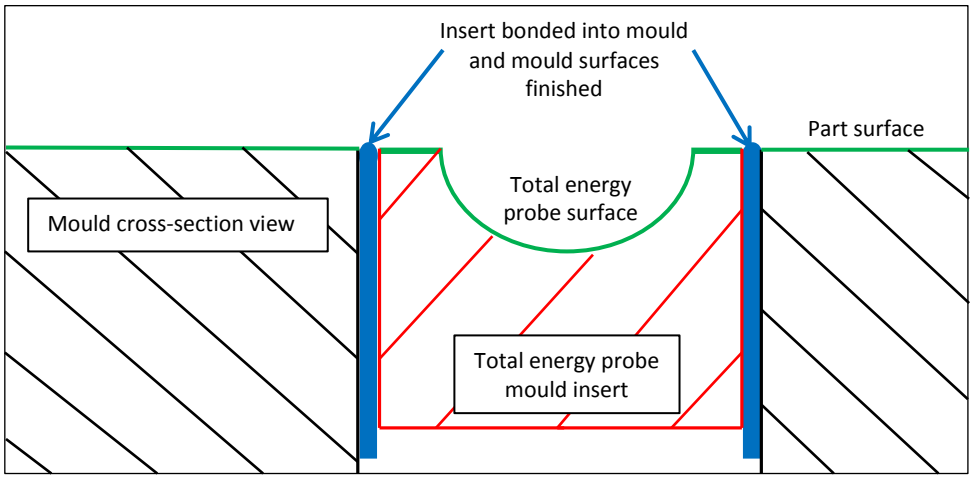

Figure 12-3: **Area where the total energy probe is positioned is removed from the mould and the total energy probe mould insert is bonded to the mould**

12.3 Separate part

The total energy probe designs can be manufactured as separate parts and assembled onto the sailplane during the final manufacturing or assembly phase (Figure 12-4). The risks of post

assembling the probe include (1) finishing the bonding surfaces between the part and skin to create a single, uniform surface without using significant time and resources and (2) ensuring the probe is installed according to the surface of the part in terms of direction (the part is bonded at the correct angles to the skin if it is not symmetric or has a non-uniform shape) and depth (the thickness of the bond between the part and skin does not change the design of the part).

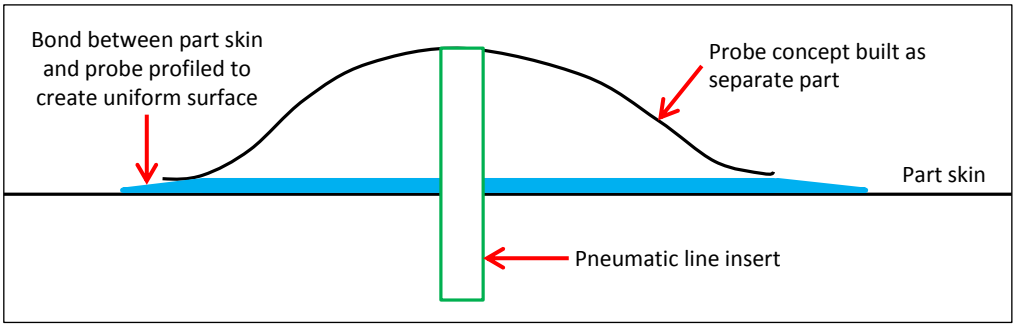

Figure 12-4: Total energy probe design built and bonded as a separate part

12.4 Conclusion

Different methods were discussed to incorporate the total energy probe into the production of sailplanes where tooling already exists or is still in the design phase.

The use of a mould modification would be the least invasive and most accurate manufacturing method to incorporate on sailplanes where moulds have already been built. Sailplanes that are still in the design phase would benefit the most, as the total energy probe design can be incorporated into the mould design and building process without having to make modifications after the moulds have been manufactured.

The total energy probe configurations and designs described in paragraph 8, 9, 10 and 11 were compared and discussed in terms of their overall performance, as well as the most optimum probe combination and placement to promote drag reduction.

CHAPTER 13: DISCUSSION

The drag and compensation characteristics of the designs described in paragraph 8, 9 and 10, as well as the drag characteristics of the additional external sensors in paragraph 11, were compared and discussed. The data of the prominent fin protrusion was excluded from comparison, as the mild fin protrusion serves as the improved design thereof. The tail plane tip bulge and fuselage nose extension were also excluded due to the significant drag increase the designs caused and their similarity in compensation performance to the mild fin protrusion.

13.1 Pressure drop comparison

All the designs measured a pressure coefficient within the set boundary between the theoretical model and current probe during straight and level flight (Figure 13-1).

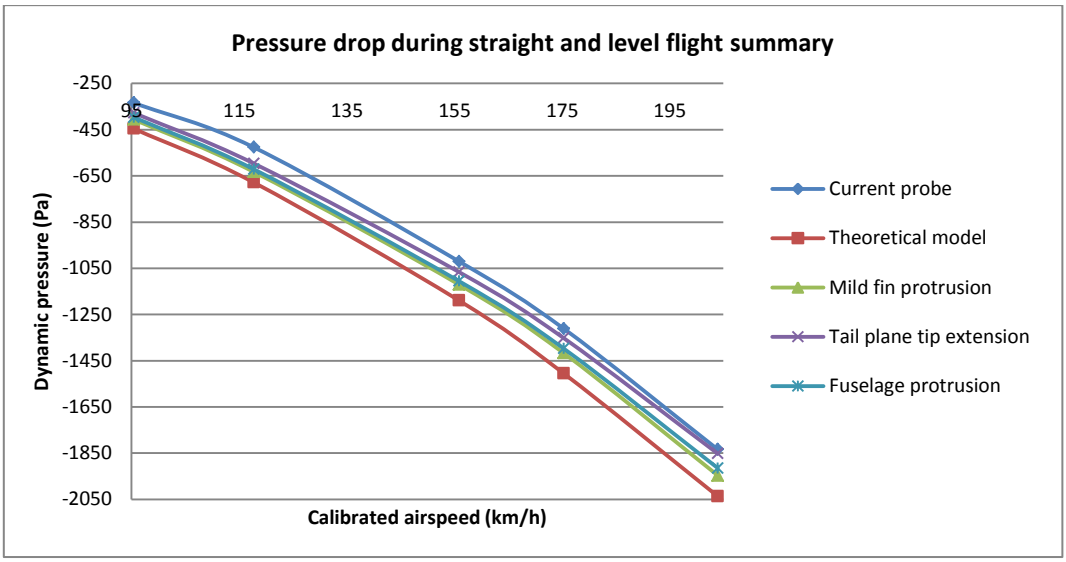

Figure 13-1: Pressure drop comparison during straight and level flight

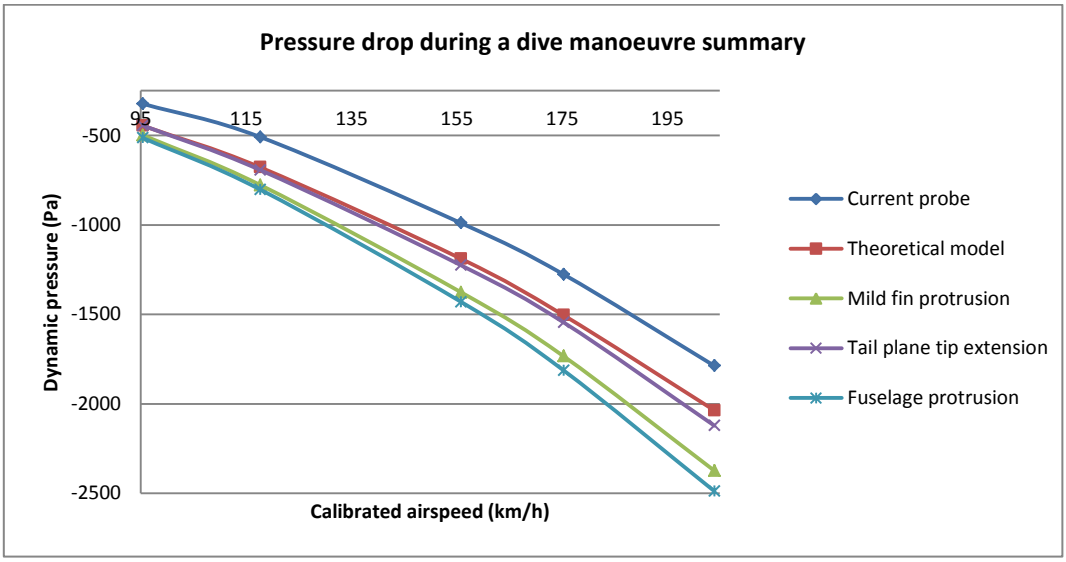

Figure 13-2: Pressure drop comparison during a dive manoeuvre

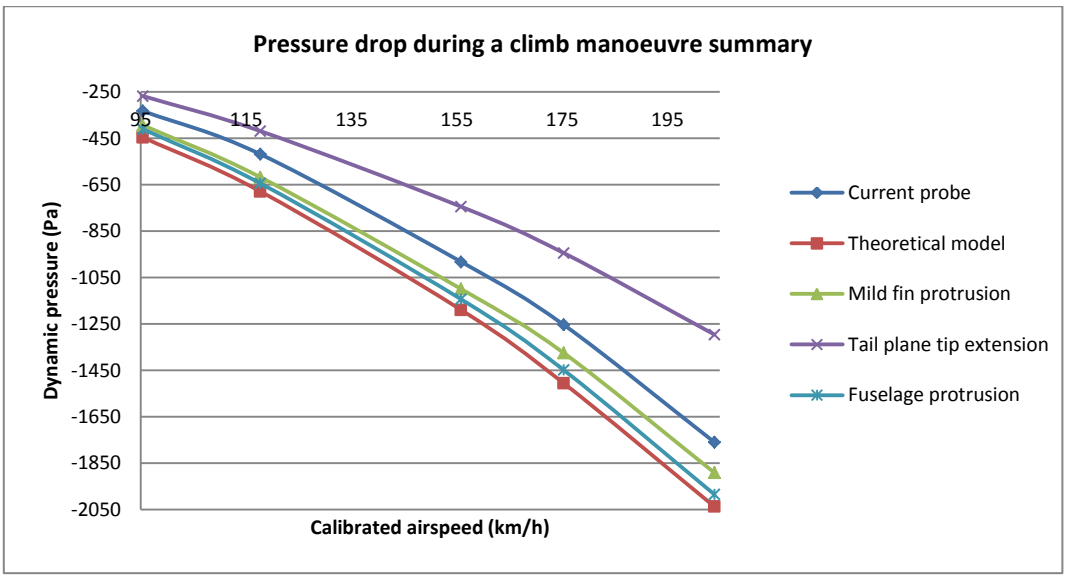

Figure 13-3: Pressure drop comparison during a climb manoeuvre

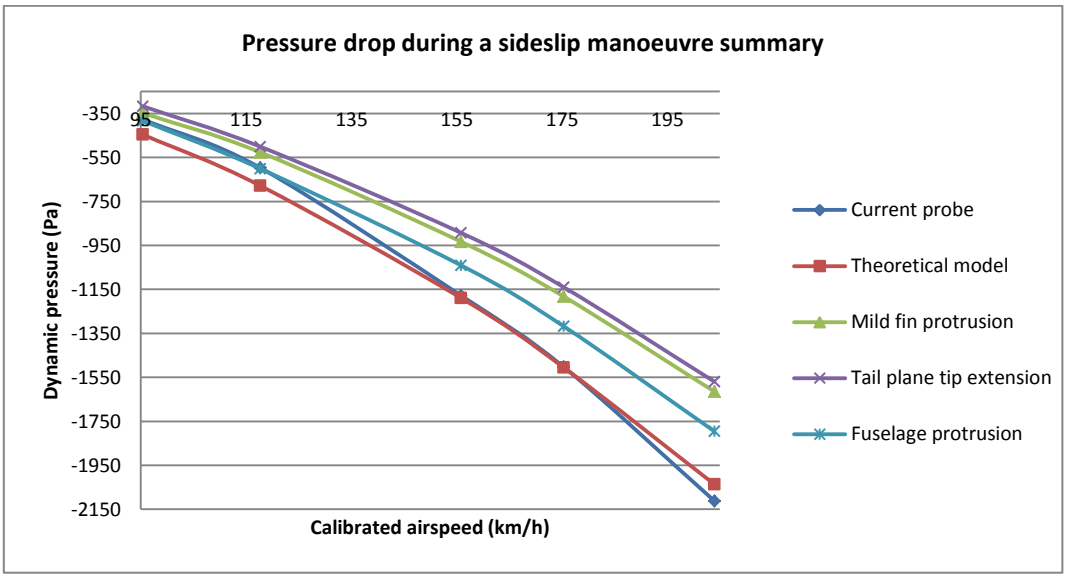

Figure 13-4: Pressure drop comparison during a sideslip manoeuvre

The tail plane tip extension was the least sensitive to dive manoeuvres and the fuselage protrusion the most sensitive (Figure 13-2).

The fuselage protrusion was the least sensitive to climb and sideslip manoeuvres and the tail plane tip extension the most sensitive (Figure 13-3 and Figure 13-4).

The significant sensitivity of the fuselage protrusion to dive manoeuvres would require fine design changes to promote pitch manoeuvre insensitivity and uniform average pressure drop changes. The sensitivity of the mild fin protrusion to pitch manoeuvres is not as drastic as the fuselage protrusion and should require minor design changes to correct.

13.2 Drag comparison

The total drag induced by the different total energy probe designs on the surfaces of the JS-1C was calculated (Table 13-1). The fuselage nose probe induced the most average total drag with 19 % and the fuselage protrusion the least with 1.6 % on the surfaces of the JS-1C (Figure 13-5). The minor drag increase of the fuselage protrusion over the large surface area of the fuselage could be a significant improvement to the drag performance of the JS-1C if successfully implemented.

Table 13-1: Total drag calculated for the total energy probe designs

	Average drag increase (%)		
Probe configuration	Left surface	Right surface	Total drag
Current probe	5.0	5.0	**10.0**
Tail plane tip probe	7.8	0.0	**7.8**
Fuselage nose probe	9.6	9.6	**19.2**
Mild fin protrusion	2.0	2.0	**4.0**
Tail plane tip extension	4.4	4.4	**8.8**
Fuselage protrusion	0.8	0.8	**1.6**

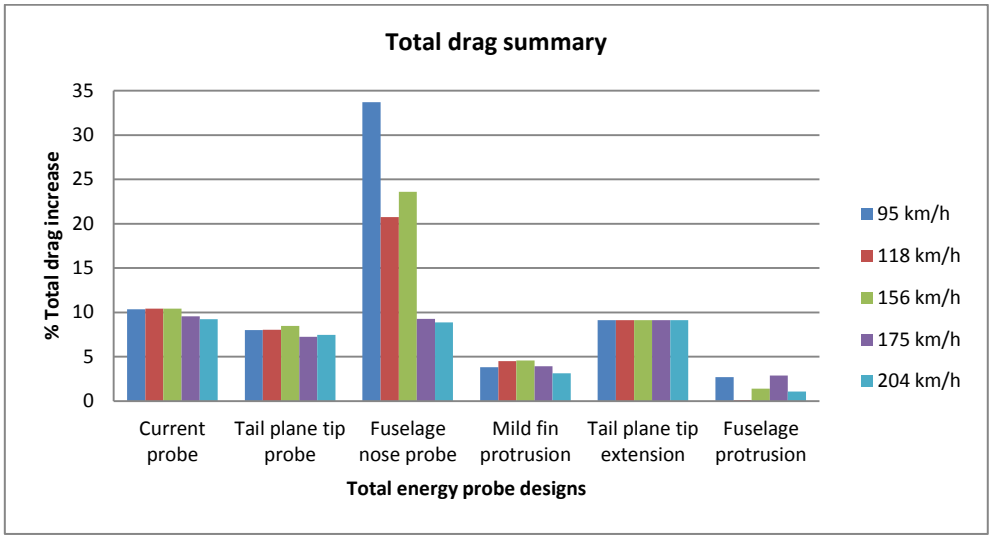

Figure 13-5: Total drag comparison of the total energy probe designs

The probe placement table created in paragraph 11.3 (Table 11-1) was compared to the concept design drag data to determine the most optimum probe combination and placement to promote drag reduction. The most optimum probe placement combination would be to install the pitot-static probe on the horizontal tail plane tip and the fuselage protrusion concept design. This would induce an estimated average total drag increase of 2.1 %, which is almost 80 % less than that induced by the current total energy probe. The use of the fuselage protrusion, however, would rather benefit sailplanes in the design phase, where the probe is designed into the tooling and avoids the risks of modifying moulds already built (paragraph 12.2).

Another possible probe combination considers the popularity of electric variometers. The installation of two pitot-static probes on each tip of the tail plane would include the benefits of improved compensation during pitch manoeuvres (paragraph 5.3) and should improve the sideslip capabilities thereof (paragraph 5.4) by measuring an average pressure during manoeuvres. This would induce an estimated average total drag increase of 1 %, which is 90 % less drag than that of the current total energy probe. This configuration is also the least invasive method to incorporate the installation of the probes into the manufacturing of the sailplane, with minimum mould surface modifications required, more accurate probe installation and less surface finish processes after manufacturing (paragraph 12.1).

Based on (1) the drag and pressure drop comparison of the different total energy probe designs, (2) the manufacturing of the probe designs and (3) the probes that need to be installed on the JS-1C, a conclusion to the dissertation was reached.

CHAPTER 14: CONCLUSION

The surface of the JS-1C vertical tail fin was analysed to determine the effect of the total energy probe on the boundary layer of the tail fin. The possibility of reducing the drag induced by the current probe without reducing the compensation capabilities thereof was identified.

Different concepts were applied to different parts of the JS-1C to determine the optimum placement and design of the total energy probe to promote drag reduction. A design applied to the sides of the fuselage skin as protrusions, such as that of Hugh Kendall, induced nearly 84 % less drag than the current total energy probe. The design required further changes to ensure uniform pressure drop changes and reduced sensitivity during pitch manoeuvres, while maintaining its reduced sensitivity to sideslip, due to the elliptic shape of the fuselage.

The JS-1C requires the additional installation of a pitot-static probe to drive critical instrumentation during flight. The combination of the pitot-static probe positioned on the tip of the horizontal tail plane and the total energy protrusions on the fuselage would induce nearly 80 % less drag than that induced by the current total energy probe. However, modifications made to mould surfaces to incorporate the total energy probe design into the production process would reduce tool life and risk diminishing an acceptable out-of-mould surface finish.

The increasing popularity of electric variometers provides another probe combination. The installation of two pitot-static probes on each tip of the tail plane would induce 90 % less drag than that of the current total energy probe, where improved compensation during pitch manoeuvres is maintained and the sideslip capabilities thereof could be improved by measuring an average pressure. This configuration is also the least invasive method to accurately incorporate the probes into the building process of the sailplane.

The following conclusions were reached:

1. The installation of pitot-static probes on each tip of the horizontal tail plane would induce the least drag.
2. The pitot-static probe provides the best compensation during pitch manoeuvres and the installation of probes on each tip should improve the sideslip capabilities thereof.
3. The installation of pitot-static probe adapters into the tail plane is the least invasive method to accurately incorporate the probes into the manufacturing of the sailplane without having to make significant changes to existing tooling that would reduce tool life and risk diminishing an out-of-mould surface finish.

Recommendations were made based on the conclusions reached.

CHAPTER 15: RECOMMENDATION

The following recommendations are based on the conclusions made in paragraph 14:

1. Sailplanes used for recreational purposes, which do not have flight computers installed that can emulate electric variometers, could benefit from the fuselage skin protrusion concept design.
2. The design of the horizontal tail plane should be reviewed to determine whether it would be possible to redesign the surfaces thereof to incorporate a total energy probe as part of the skin, without the difference in pressure distribution affecting the sensitivity of the probe during pitch and sideslip manoeuvres.

BIBLIOGRAPHY

Althaus, D. 1971. New nozzle for total energy compensation. *Sailplane & Gliding*, 21(6):453-454.

Anderson, J.D. 1991. Fundamentals of aerodynamics. 2nd ed. Maryland: McGraw-Hill.

Aucamp, N. 2014. Manufacturing an internal airflow system for the JS-1 and JS-2 third scale models. Potchefstroom: NWU. (Report - BEng).

Brandes, T. 1975. Braunschweig tube. *Soaring magazine*, 39(1):37-38.

Brözel, R. 2002. Total energy compensation in practice, edited by T. Knauff & D. Nadler. Bayreuth: ILEC GmbH.

Dawydoff, A. 1943. Total energy variometer. *Soaring magazine*, 7(1-2):7,12.

Edi, P., Yusoff, N. & Yazid, A.A. 2008. Airfoil design for flying wing UAV (Unmanned aerial vehicle). (*In* Martin, O., *ed*. Recent advances in applied and theoretical mechanics: Proceedings of the 4th WSEAS international conference on applied and theoretical mechanics. Cairo: WSEAS Press. p. 106-111).

esa systems. 2016. Multi probe DN/3-fach/UN. https://www.esa-systems.com/en/products/details/multisonde-dn3-fachun/ Date of access: 24 June 2016.

FAA (Federal Aviation Administration). 2013. Glider flying handbook. Oklahoma City: U.S. Department of Transportation.

Gordon, R.J. 2006. Optimal dynamic soaring for full size sailplanes. Ohio: Air force institute of technology. (Thesis - MSc).

Hendrix, J. 2012. Deturbulator project. http://www.deturbulator.org/Progress-OilFlows.asp Date of access: 20 July 2016.

Johnson, R.H. 1998. Development of a total energy system for the PW-5 sailplane. *Soaring magazine*, April:16-19.

JS (Jonker Sailplanes). 2014. RFC.JS-1086. Potchefstroom: JS. (Request for change internal company document).

Kantrowitz, A. 1940. Letter to the editor. *Aeronautical Sciences*, 7(12):523.

Kendall, H. 1952. Total energy variometer. *Gliding magazine*, 3(1):29-31.

LXNAV. 2016a. LX 9000. http://lxnav.com/products/lx9000.html Date of access: 7 March 2017.

LXNAV. 2016b. S100. http://lxnav.com/products/lxnav-varios/s100.html Date of access: 7 March 2017.

McCormick, B.W. 1979. Aerodynamics, aeronautics and flight mechanics. Pennsylvania: John Wiley & Sons.

Ngo, C.C. & Gramoll, K. 2016. eCourses. http://www.ecourses.ou.edu/cgi-bin/ebook.cgi?topic=fl&chap_sec=07.4&page=theory Date of access: 12 June 2015.

Nicks, O.W. 1976. Simple total energy sensor. Hampton: Langley Research Center.

Ostroff, A.J., Hueschen, R.M., Hellbaum, R.F. & Creedon, J.F. 1981. Flight evaluation of a simple total energy-rate system with potential wind-shear application. Hampton: Langley Research Center.

Reid, M. 2009a. Soaring café. http://soaringcafe.com/2009/11/total-energy-compensation-explained-part-i/ Date of access: 19 March 2015.

Reid, M. 2009b. Soaring café. http://soaringcafe.com/2009/11/total-energy-compensation-explained-part-ii/ Date of access: 19 March 2015.

Sebald, L. 1981. Soar Idaho. http://www.soaridaho.com/Schreder/Construction/T_E_PROBE_ANTENNA.html Date of access: 27 May 2015.

Van der Walt, F.M. 2015. Aerodynamic improvement of the total energy probe used on sailplanes. Potchefstroom: NWU. (Report - BEng).

Wills, P. 1952. 1952 World championships. *Gliding magazine*, 3(3):102-106.